Graduate Theses and Dissertations   Graduate School

1-1-2015

Large-eddy Simulation of the Inner Continental Shelf Under the Combined Effects of Surface Temperature Fluxes, Tidal Currents and Langmuir Circulation

Rachel Walker

University of South Florida, rachelwalker@mail.usf.edu

Follow this and additional works at: http://scholarcommons.usf.edu/etd

Part of the Civil and Environmental Engineering Commons

www.manaraa.com

Large-eddy Simulation of the Inner Continental Shelf Under the Combined Effects of Surface

Temperature Fluxes, Tidal Currents and Langmuir Circulation

by

Rachel Walker

Major Professor: Andrés E. Tejada-Martínez, Ph.D.
Daniel C. Simkins, Jr., Ph.D.
Muhammad M. Rahman, Ph.D.
Mark Luther, Ph.D.
Boris Galperin, Ph.D.

Date of Approval:
April 7, 2015

Keywords: Numerical simulation, ocean modeling, LES, vertical mixing, surface cooling

Dedication

This work is dedicated to my parents, who have been an endless source of inspiration and motivation throughout not only the PhD program, but my whole life. The continued support of my grandfather, Bert, and the patience and encouragement of Justin Howard and my closest friends have also been invaluable, and this would not have been possible without them.

Acknowledgments

I would like to express my sincere gratitude to Dr. Andrés Tejada-Martínez for his help and support throughout the Ph.D. program. The insightful perspectives and constructive feedback he has provided over the last four years have made the research process both productive and enjoyable. I am also genuinely grateful to my committee members Dr. Daniel C. Simkins, Jr., Prof. Muhammad M. Rahman, Dr. Boris Galperin and Dr. Mark Luther for their time and effort, and for the valuable classes they have provided across several disciplines. Additional thanks to my committee chairperson, Prof. Aydin K. Sunol for his time.

Other members of the Environmental Computational Fluid Dynamics group, past and present, have always provided guidance and encouragement. Special thanks go to Dr. Cigdem Akan, Dr. Roozbeh Golshan and Dr. Nityanand Sinha for both their teachings and their kindness, as well as Dr. Jie Zhang and Amine Hafsi.

Without funding from both the National Science Foundation and the University of South Florida in the form of fellowships, assistantships and a highly enjoyable position working in the Writing Studio, this work would not have been possible.

Table of Contents

List of Tables

List of Figures

v

vi

vii

ix

Abstract

In a shallow shelf region, turbulent motion can have a major effect on coastal processes including ecosystem functioning, surface gas exchange and sediment resuspension. Many factors contribute to such turbulence; wind and wave forcing, buoyancy induced by surface heat fluxes and tidal forcing all play a key role in generating vertical mixing in this shallow region. Alongside these independent sources of turbulence, combinations thereof can lead to full-depth turbulent structures acting secondary to the mean flow and leading to enhanced vertical mixing throughout the entire water column.

Field and laboratory experiments can often prove to be costly and time consuming, and reproducing or maintaining the complex flow dynamics of real world ocean flows is a constant challenge to these methods of research. As such, those interested in developing realistic and useful models of the marine environment to further understand its behavior often rely on 3-dimensional mathematical modeling and simulation. In this dissertation, simulations will be presented of turbulent flow and associated vertical mixing in a domain representative of the shallow coastal ocean, sufficiently far off shore that the land-ocean boundary does not significantly affect the flow behavior. This will be done using a large-eddy simulation (LES) method; solving the governing Navier-Stokes equations over a finite grid designed to capture the large, energy containing turbulent scales, and modeling the smaller, sub-grid scales.

The simulations to be presented feature combinations of coastal forcing mechanisms which are either presently unexplored or the analysis of which has been hindered by the complexity of field

measurements and the challenge of isolating independent causes of turbulent motion. This will include surface heat fluxes, tidal forcing and Langmuir (or wave) forcing, acting both in isolation and in conjunction with each other, in order to bridge existing gaps in knowledge and provide a more complete understanding of the generation of full-depth turbulent structures in this shallow coastal water column.

Chapter 1:

Introduction

1.1 The Coastal Ocean

The coastal ocean accounts for approximately seven percent of the global ocean and is defined as the region in which the seabed is at a sufficiently shallow depth to affect physical, biological and chemical processes. This is typically less than 200 m in depth and extending as far as 80 km from the shore, and includes continental shelf regions such as the Gulf of Mexico. A more detailed description of this coastal zone can be found in [35]. For our purposes, the main focus will be on the inner continental shelf region of depth up to around 50 m.

Turbulent motion, defined as that which features chaotic property changes including rapid variation of velocity in space and time, is a critical feature of most environmental flows. Such motion is characterized by eddies or small packets of fluid particles demonstrating coherent patterns of velocity and vorticity, the interaction of which can lead to substantial levels of mixing. In a shallow coastal ocean region, various environmental phenomena can lead to the initiation of turbulent mixing on a variety of scales. These include winds which lead to shear stresses, waves and surface overturning, tidal forces and currents, and surface heat fluxes which induce buoyant motion. There also exist turbulence inhibitors, such as a stabilizing surface heat flux or a density stratified region known as a pycnocline. See Figure 1.1 for factors contributing to a turbulent near-surface ocean

1
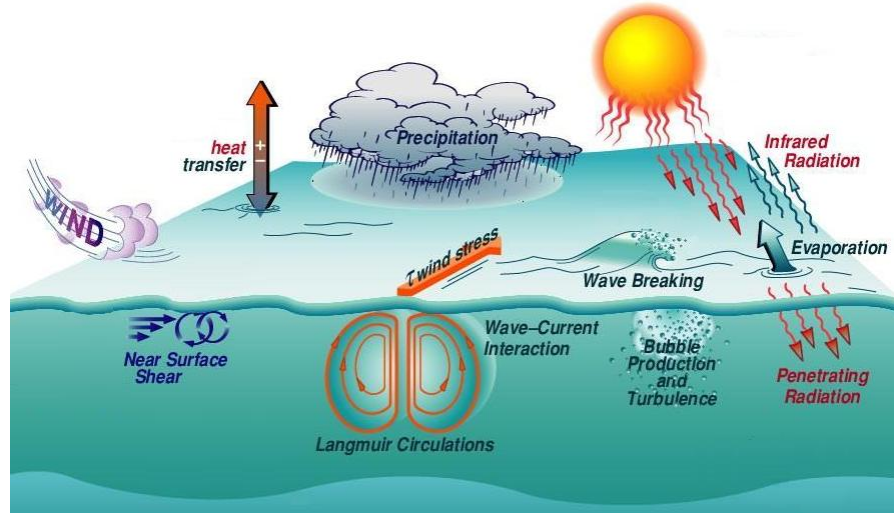
Figure 1.1: Causes of turbulence in the upper ocean mixed layer. Source: [37]. ©Woods Hole Oceanographic Institution. Reprinted with permission [see Appendix D].

system. A further summary of turbulent ocean processes from a marine ecologist perspective can be found in [25].

Typically, a shallow ocean comprises of a series of distinct regions layered in the vertical direction, which are formed by the influence of the various kinds of turbulence outlined above. At the surface is found the upper ocean mixed layer (UOML), the region depicted in Figure 1.1, which lies directly below the air-water interface and is mixed by surface processes such as wind shear and wave forcing whose significance decays with depth. The UOML extends either to the sea bed if the ocean is sufficiently shallow (a fully mixed water column) or to the pycnocline region which features a stable density gradient strong enough to overcome this mixing. In the lower half of the water column exists a tidally driven bottom boundary layer, again mixed, and the height of which is partially determined by the ocean floor roughness. The thickness of these respective layers is highly variable according to environmental factors such as wind strength, wave height and intensity of stratification, but typically they can reach up to tens of metres in the shallow shelf region. For our purposes we focus primarily on the case in which the region is sufficiently shallow that

2

turbulent mixing homogenizes the whole water column, although stabilizing, turbulence inhibiting heat fluxes and stratified temperature profiles will also be addressed.

Alongside the independent sources of turbulence mentioned above, combinations thereof can lead to full-depth turbulent structures which can cause mixing of flow properties throughout the entire water column. Such turbulent motion is able to take the form of cellular structures, rotating around a horizontal axis often approximately aligned with the wind or tide, and spanning the full depth of the water column. When this is the case, these cells have the capacity to affect flow properties from the surface down to the sea floor. The development and sustainability of these large-scale turbulent structures induced by combinations of forcing mechanisms will be the focus of the present work.

In a greatly simplified model problem without the complexities of the natural ocean environment, for example in a channel flow driven by a pressure gradient or a constant surface stress, full-depth turbulent structures can also be observed acting as a secondary motion to the mean flow and persisting in space and time. To put into perspective the typical scale and characteristics of one such form of turbulent motion in a simplified model problem, we may consider the case of a Couette flow: a flow driven by the shear stress generated by two infinite parallel plates moving in opposite directions. In the computational simulations of Lee and Kim (1991) of such a problem, time- and space-persistent structures in the form of large, rotating roll cells oriented down-stream and secondary to the mean flow have been observed (see Figure 1.2) [13] . These structures were found to fill the entire channel and contribute as much as 30% to the total turbulent kinetic energy.

3
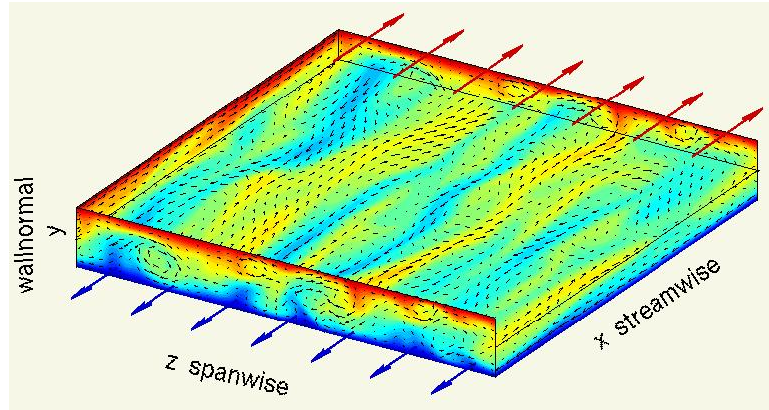
Figure 1.2: An instant in the evolution of plane Couette flow in a rectangular domain. Large arrows indicate direction of motion of respective planes, velocity vectors depict full-depth cellular structures. Adapted from [40]. ©J. F. Gibson. Reprinted with permission [see Appendix D].

Following this computation of streamwise elongated roll cells in [13], Papavassiliou and Hanratty (1997) [21] also found in their computational simulations of a similar flow that the streamwise-aligned, elongated cell structures are persistent enough in space and time to be deemed secondary structures to the mean flow [21]. Note that although the spanwise and wall normal velocities of the secondary flow are small compared to the mean streamwise flow velocity, they contribute to the mixing and transport due to the fact they persist in space and time. These structures can be visualized on horizontal planes of the flow by a strongly streaky structure in the streamwise velocity fluctuation; the shaded regions in Figure 1.3 represent two positive uninterrupted streamwise velocity streaks at mid-depth in the domain, extending from one end of the channel to the other in the Couette flow computation of [21].

Despite this being a simplistic problem with a basic flow definition, the key characteristics of the roll cells observed, notably their persistence in space and time and their secondary motion to the mean flow, provide the foundation for our definition of full-depth turbulent structures to be applied to our more complex environmental flows. Structures of this kind in a coastal ocean envi-

4
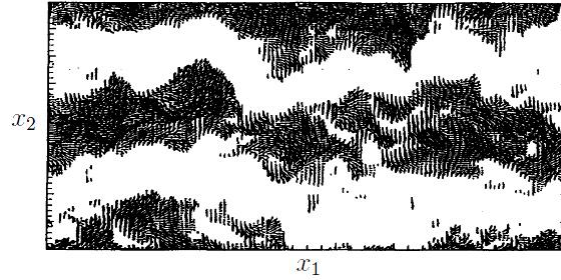
Figure 1.3: Positive streamwise velocity fluctuations on a horizontal plane in DNS of Couette flow. x_1 represents the streamwise direction, x_2 the cross-stream. Shown are uninterrupted streaks elongated in the streamwise direction. Shaded regions represent positive velocity fluctuations, blank regions represent negative velocity fluctuations. Adapted from [21]. ©Elsevier. Reprinted with permission [see Appendix D].

ronment can lead to significant levels of vertical mixing; the many reasons a detailed understanding of vertical mixing mechanisms is necessary will be discussed in the next section. Following this, an outline of some of the forcing mechanisms known to lead to large-scale turbulence in a coastal ocean or more general channel flow environment will be presented, alongside a summary of relevant developments in their study. This will be followed by identification of the key gaps in existing knowledge or understanding relating to this turbulent motion in a coastal environment.

1.1.1 Motivation

An improved understanding of the mixing induced by environmental forcing mechanisms may be relevant to several external interest groups, ranging from marine biologists to coastal ecologists to environmental policy makers. Several potential applications of greater understanding of turbulent motion and vertical mixing in coastal flows is provided below.

The effect of strong vertical mixing on near-shore ecosystems is too significant to be disregarded, affecting temperature, salinity, nutrient concentration, sediment resuspension, light and ultimately species-specific growth and predator-prey relationships. Petrovskii and Malchow (2004)

5

[23] state that "even small changes in the environmental conditions may lead to a significant change in the ecosystem functioning, particularly, to dramatic changes in species abundance". For example, many types of plankton reside in the nutrient and sunlight-rich upper (or shallow) ocean and act as a permanent food source for marine species higher up the food chain, ultimately including the human population. Plankton communities are, by definition, unable to swim against a current, and as such they typically move with the bulk flow, driven by tides or currents. Peters and Marrase (2000) [22] state that "large-scale turbulence can affect a range of biological processes ... bringing nutrient-rich water into contact with plankton cells ... and transporting plankton and detritus away from their sites of growth or production". As such, turbulence-induced vertical mixing may cause the redistribution of plankton 'plumes', potentially inhibiting their intake of nutrients or limiting their interaction with predators and having a significant impact throughout the food chain.

Phytoplankton communities are also a vital element of the carbon cycle. By transforming carbon from the ocean floor into carbon dioxide which can then be transferred into the atmosphere, these microscopic aquatic plants ultimately supply a substantial proportion of the oxygen consumed by living beings. This photosynthetic procedure can only occur at the surface of the ocean. It has been found that the strength of turbulent upwelling regions in ocean flows can contribute to the provision of nutrients to these surface-dwellers. According to oceanographers at the National Oceanic and Atmospheric Administration, a significant 75 percent decrease in phytoplankton has been seen to correspond to just a 5 degree temperature increase caused by winds too weak to cause the turbulent redistribution of cool waters from the ocean floor [36].

Alongside the influence on marine animal and plant life, full-depth turbulent structures can also influence other environmental processes such as the transfer of momentum from wind and surface waves to the water column, and the transfer of gases between ocean and atmosphere which

6

ultimately affects the chemical composition of both respective parts. Surface gas exchange models are often based on the wind speed, as an increased wind speed causes increased wave motion which in turn can lead to the production of surface bubbles which facilitate the transfer of gases in both directions. However, only accounting for wind in these models does not acknowledge the surface turbulence coming from other mechanisms such as those to be addressed in the current work. Further understanding of turbulence in particular near the ocean surface can potentially aid these models for gas exchange and allow further development of studies of the transfer across the air-sea interface of carbon dioxide and other gases which influence climate change including global warming and radiation. Further detail on the impact of full-depth turbulent structures on surface gas exchange can be found in [1] and [2].

Turbulent ocean characteristics are found in many advanced models of climate change used for research and development. The National Center for Atmospheric Research has developed "one of the worlds most sophisticated models" of the global climate (see Figure 1.4). Surface winds, vertical mixing, ocean currents, temperature and salinity and air-sea exchanges all feature prominently and all require accurate resolution or parameterization. In these models turbulent vertical mixing is parameterized via eddy viscosity and eddy diffusivity models. Thus improved understanding of how vertical mixing turbulent processes behave under various forcing mechanisms is highly valuable.

"The need for improved understanding of the coastal ocean is urgent, since this ocean region has special importance to society. For example, humans need to make wise use of coastal ocean fishery and petroleum resources, while coping with the hazards the ocean can pose to the 50 percent of the U.S. population that lives near the coast. Humans must understand the coastal ocean to

7

minimize adverse impacts due to coastal engineering projects, changes in freshwater drainage, pollution, and introduction of exotic species." [38]
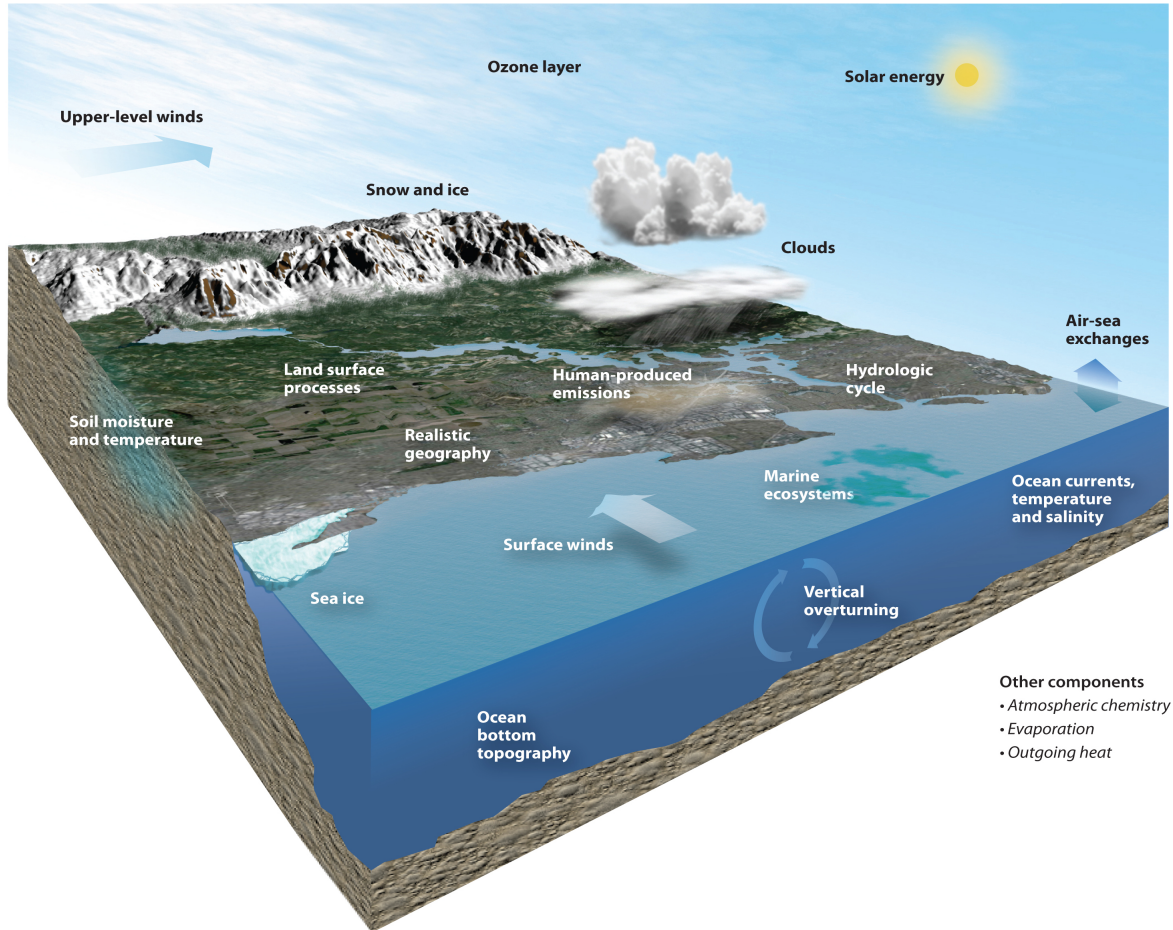
Figure 1.4: Components of the Community Earth System Model for climate systems. NCAR 2004 [42]. Reprinted for educational purposes with permission [see Appendix D].

A further potential use of advanced understanding of shallow ocean turbulent motion is in the study of contaminant dispersion models, brought under intense scrutiny in the years since the Deepwater Horizon oil spill of 2010. Upper ocean mixing processes can have a significant impact on such dispersion, and should be accurately accounted for in contaminant spill models. According to a 2005 National Research Council report titled "Oil Dispersant: Efficacy and Effects" [43],

improved representations of natural mixing processes would aid decision makers in understanding the behaviour of dispersants under varying wind and wave forcing conditions.

As can be seen, the findings of research into the behavior of turbulent coastal processes have applications across many disciplines, which suggests the importance of developing a complete and comprehensive understanding of ocean behavior under varying environmental conditions. By collecting continuous, real-time data on time-varying flow properties such as pressure, velocity and temperature in shallow ocean regions, persistent flow patterns and behaviours can be identified and analyzed. Such field measurements can be acquired from research vessels, buoys and on-shore coastal monitoring systems using a variety of techniques and equipment. This includes acoustic doppler velocimetry which serves to measure the components of flow velocity at regular, high frequency time increments or profilers moored to the seabed which can vary in depth and measure temperature components, along with many other constantly advancing oceanographic technologies.

In-situ measurements are crucial for the continuing improvement of our understanding of the ocean, yet such field measurements can prove to be costly and time consuming, as well as not typically being generalizable to many locations. Results from field experiments also often include a great deal of information which extends beyond the scope of the empirical study and as such does not get sufficiently analyzed. Moreover, there are typically many environmental turbulence-generating mechanisms at play at any one time in the real-world scenario; isolating individual contributing factors to turbulent processes can be virtually impossible. Laboratory experiments are an option, but these also face the difficulties of reproducing the many complex flow properties which occur in real world ocean flows.

9

Given the above, those interested in developing realistic and useful models of the marine environment to further understand its behavior often rely on 3-dimensional mathematical modelling and simulation to complement existing observations from the field. Computational simulations of various kinds of fluid flows have been conducted for many years to improve understanding of turbulent flow characteristics. The application of numerical modelling to turbulent structures in the coastal ocean is crucial to forming a complete basis of knowledge on their development and sustainability, with a further benefit of being able to isolate individual forcing mechanisms to better understand their effect on turbulent motion, and it is hoped improved understanding will aid a more thorough analysis of both existing and future field data.

In fluid flows, both in the ocean and in simpler model problems, several fundamental mechanisms can lead to full-depth cellular patterns and vertical mixing. These will be summarized in the following sections.

1.1.2 Convective Motion

In flows in which density variations associated with temperature and/or salinity variations are present such as in the ocean, the action of gravity can induce convective motion. For example, considering the case of a regular horizontal channel flow with a negative temperature gradient between the upper and lower walls, thermal instability may initiate turbulent motion in which the cooler, heavier fluid sinks, and the warmer, lighter fluid rises. The release of potential energy associated with this movement can provide kinetic energy to sustain the motion. Whether the destabilizing action of the temperature difference is strong enough to overcome a stable equilibrium depends on the dimensionless Rayleigh number, representing the ratio of the destabilizing effect of the buoyant force to the stabilizing effect of factors which oppose convective motion such as the

10

viscosity and thermal diffusivity. Thermal instability typically occurs when the Rayleigh number exceeds a critical value of around 1700.

Thermal conduction leads the rising warm fluid to cool at the surface and hence begin to sink again, and similarly the sinking cool fluid heats up near the warmer lower surface, allowing the motion to continue in a steady pattern. Horizontal motion at the surface and the bottom maintains continuity. Convection cells can take several forms, for example three-dimensional hexagonal structures, or counter-rotating elongated cells (see Figure 1.5). The self-organizing flow due to a non-uniform temperature distribution in a layer of fluid is typically called Rayleigh-Benard convection.
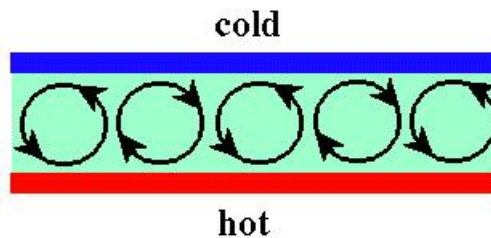
Figure 1.5: Cellular structure of Rayleigh-Benard convection [39]. ©S. Morris. Reprinted with permission [see Appendix D].

In the opposite scenario in which the temperature gradient is positive over the height of a water column, stable density stratification provides resistance to mixing, inhibiting vertical motion and reducing the vertical transfer of momentum. Although the situations described here are again simple model problems, stably stratified and unstably stratified density profiles induced by surface heat fluxes can have significant effects in various environmental phenomena.

Taylor et al. (2005) [29] considered the case of an open channel with stable stratification imposed at the free surface by a constant heating flux. An adiabatic solid lower wall was used and a stably density stratified pycnocline was seen to develop throughout the channel, inhibiting the

11

mixing induced by the turbulence generated by flow interaction with the solid wall at the lower boundary. Similar results have been found with a fixed temperature difference across the channel in which the Dirichlet boundary conditions impose a greater temperature at the surface than the bottom [3].

Many numerical simulations of unstable stratification have also been conducted in recent years. In DNS of a cooling air-water interface, Leighton, Smith and Handler (2003) [14] observed that when the heat flux out of the shear-free upper surface is sufficiently strong, the cool thermal boundary layer becomes unstable and turbulence is initiated by free convection and maintained by buoyant production. The spatial scales of the rising warm plumes and sinking cool plumes were found to be controlled by the heat flux as opposed to being inhibited in size by the computational domain. In 2012, Bammou et al. [4] considered a horizontal channel heated uniformly from below, hence again imposing unstable density stratification. Results showed the development of thermal instabilities in the form of steady, longitudinal convective roll cells.

The atmospheric boundary layer (ABL) is one environmental flow known for convective turbulence. The ABL refers to the lowest part of the atmosphere, the characteristics of which are directly affected by proximity to the Earth's surface. The changing surface temperature of the Earth, notably the heating of the Earth's surface causing upward heat advection, can have the effect of causing an upward heat flux and negative temperature gradient, leading to convective instability. When both convection and wind stress are applied, convective cells reaching up to 1 or 2 km in depth can develop and velocity fluctuation maps show a similar streak structure to that found in our existing examples of Couette flow visible in Figure 1.3. In these convective atmospheric flows "cloud streets" or horizontal helices of air flow, elongated and oriented nearly parallel to the mean

12

ambient flow direction, can form as a product of the horizontal convective rolls, as can be seen in Figure 1.6.
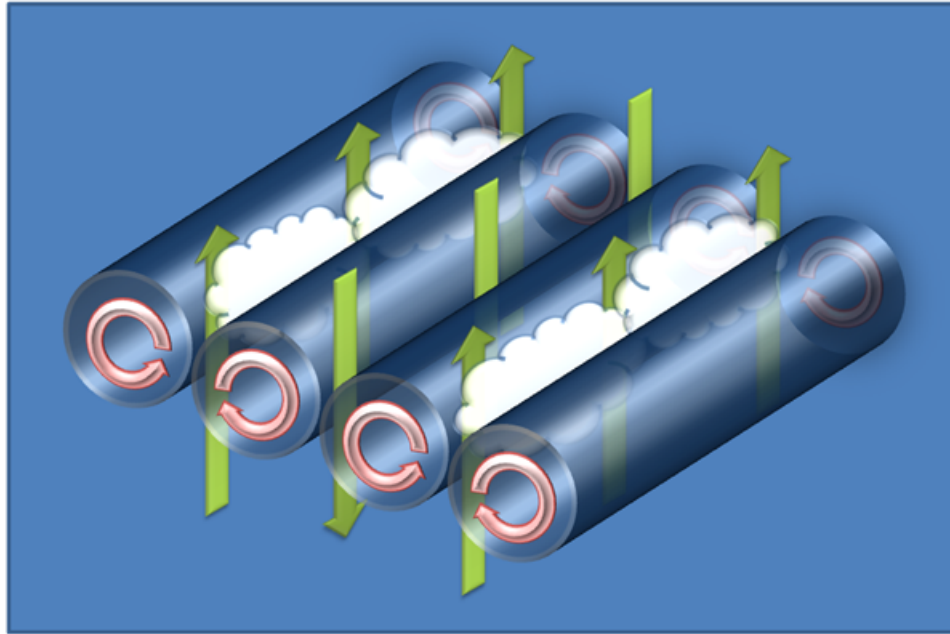
Figure 1.6: Simple schematic of the production of cloud streets by horizontal convective rolls [41]. Released into public domain by author [see Appendix D].

As can be seen, convective instability can lead to the generation of large-scale turbulent structures in both computational and observed environmental flows. Prior to 2014, the LES method featured in the present dissertation (to be discussed in more detail in Chapter 2), when applied to flows representative of a shallow coastal ocean domain, had typically maintained focus on the application of surface heating or the application of bottom and surface Dirichlet boundary conditions such that the temperature difference between the upper and lower boundaries was fixed. The first goal of the present work was to consider a pressure gradient driven channel flow with zero surface shear stress and apply a constant surface heat flux to see the impact of a cooling induced buoyancy on the development of the turbulence. The domain depth was representative of a shallow coastal ocean region, and the constant pressure gradient or body force assumed to represent a tidal force

13

at peak tide; the turbulent motions were considered on a time-scale significantly shorter than that of a full tidal cycle such that this can be assumed to be temporarily constant. The findings of this study were published in [34] and will be summarized in Chapter 5.

1.1.3 Langmuir Circulation

In both the wind and wave driven upper ocean mixed layer (UOML) and a fully mixed shallow water column, previous studies, both field-based and computational, have demonstrated the existence of persistent turbulent cellular structures below the ocean surface. These structures are similar to the Couette flow roll cells described previously in the sense that they are also secondary to the mean flow, cause vertical mixing and redistribution of flow components and can persist in space and time. A phenomenon known as Langmuir forcing, induced by the interaction of the Stokes drift velocity caused by surface gravity waves (in the direction of wave propogation) and vertical vorticity from wind-driven mean currents, has been seen to lead to the development of these cells, which are denoted Langmuir cells or Langmuir circulation (LC). Langmuir cells consist of parallel, counter-rotating vortices which are oriented downwind, and their formation leads to regions of convergence on the water surface which can be seen in the ocean as streaks of debris (for example bubbles or debris) also oriented down-wind and known as windrows (see Figure 1.7). Maximum downwind velocity occurs at these convergence points between cells, and below this surface convergence is a region of downwelling, pulling surface waters down to deeper depths.

14
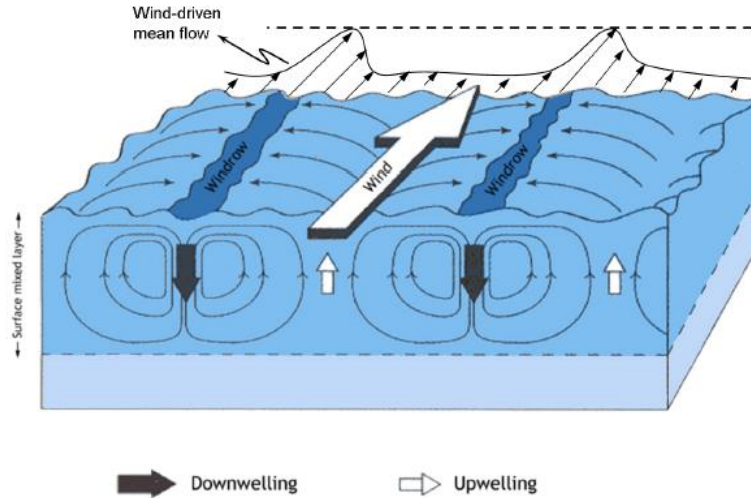
Figure 1.7: Cellular structure of Langmuir circulation (LC). ©The Royal Swedish Academy of Sciences. Reprinted with permission [see Appendix D].

LC often occurs when winds and waves are roughly aligned and wind speeds are greater than 3 m/s. The largest scales of LC can extend from tens of meters to kilometers in the downwind direction and can be separated by distances ranging from meters to as much as a kilometer [33]. For the cells to develop, initially a shear force has to exist on the surface of the ocean caused by wind. In the presence of significant wave forcing, Stokes drift will occur aligned with the wind, and it is known that both the surface wind-driven velocity and the Stokes drift will decrease with increasing depth. This causes greater fluid transport at the surface than lower in the ocean or channel. The layering of the Stokes drift velocity in this manner can cause any vortical motion present at the surface to rotate into the form of vertical cell structures, with their axis of rotation now aligned with the wind direction.

Following Langmuir's initial observation of these upper ocean structures in 1938 [12], the scope of knowledge of this turbulent process has increased significantly. LC has been found during field measurements and has also been modeled computationally through the addition of a Craik-

15

Leibovich (C-L) vortex force, a term in the momentum equations accounting for the generation mechanism of LC by parameterizing the interaction between the shear current and the Stokes drift velocity [5]. Historically, LC has been observed spanning the upper ocean mixed layer in deep water, bounded below by a pycnocline [27]. However, recently LC has also been observed in shallow coastal ocean regions by Gargett et al. (2004) [8], extending from the surface to the bottom of the water column.

The field research outlined in [8] significantly altered our understanding of the key turbulent processes in a shallow coastal region. Detailed acoustic Doppler current profiler (ADCP) measurements identified full-depth Langmuir cells, entraining the whole vertical water column and lasting as long as 18 hours in a coastal shelf region 15 m in depth just off the coast of New Jersey. The coherent full-depth structures were seen to develop episodically, similar in structure to those seen in a basic Couette flow but greater in strength, and were defined as 'Langmuir supercells' due to the fact that the LC extended to the bottom of the water column (unlike the aforementioned LC in the upper-ocean mixed layer which is inhibited below by a pycnocline). More recently, Scully et al. (2014) [26] also observed that wind- and wave-driven circulation and mixing in the estuarine system of Chesapeake Bay is consistent in structure with full-depth Langmuir circulation, and additionally noted that tidal currents, vertical density stratification and surface heat fluxes were all able to modulate the intensity and coherence of the observed circulations.

Motivated by the field observations of [8], three-dimensional simulations of full-depth LC were conducted by Tejada-Martinez and Grosch (2007) [30]. These simulations required use of a 'large-eddy' technique which resolved only the scales of turbulence which contribute significantly to the kinetic energy of the flow, hence reducing computational cost; the various kinds of numerical simulation techniques will be discussed in the next chapter. The cases considered were a wind-driven

16

shear flow without Langmuir circulation, and the same flow with Langmuir circulation under varying wave conditions for comparison to the existing data. In the first case, velocity profiles on vertical planes indicated downstream-oriented roll cells similar in structure to the Couette cells found in [21]. Inclusion of Langmuir forcing (provided through the Craik-Leibovich force described earlier) in this wind-driven flow caused the Couette cells to merge in the cross-stream direction, giving rise to scales consistent with those found in the existing field observations of Langmuir cells by Gargett et al. (2004) [8]. In particular, the magnitude of velocity fluctuations from the LES, when dimensionalized using the wind stress friction velocity during Gargett's observations, were in good agreement with the field measurements. These computational tests were unique as they focused on LC in a shallow water column which is affected by a bottom boundary layer, whereas prior simulations had maintained focus on a surface mixed layer over deep water where the effects of a bottom boundary layer on near-surface processes are not present.

The findings of [8],[30] and [32] indicate that the application of Langmuir forcing is able to cause the development of Langmuir cells strong enough to penetrate to full depth, leading to significant disruption of the log-layer profile in the bottom boundary layer, and causing a significant increase in sediment resuspension. The full-depth vertical mixing corresponding to the presence of these cells has the potential to directly affect biology, sediment transport and gas exchange in shallow oceans, as was discussed previously. As these shallow shelf-based "supercells" are a relatively new contribution to the study of Langmuir turbulence, further clarification of how such structures may behave when acting in conjunction with other turbulence-inducing forcing mechanisms was a secondary aim of the current work.

17

1.1.4 Tidal Currents

In the previous section, both field and computational measurements of LC were addressed. The works of both [8] and [30] focus on a shallow ocean flow experiencing a constant surface wind stress. A similar configuration instead with zero surface shear stress representative of an initially unstratified tidally driven bottom boundary layer approximately 10 m in depth was considered by Li et al. (2004) [15]. A maximum tidal speed of 0.5 m/s was observed, and the tidal force was oscillatory with a dimensional period of 12.5 hours.
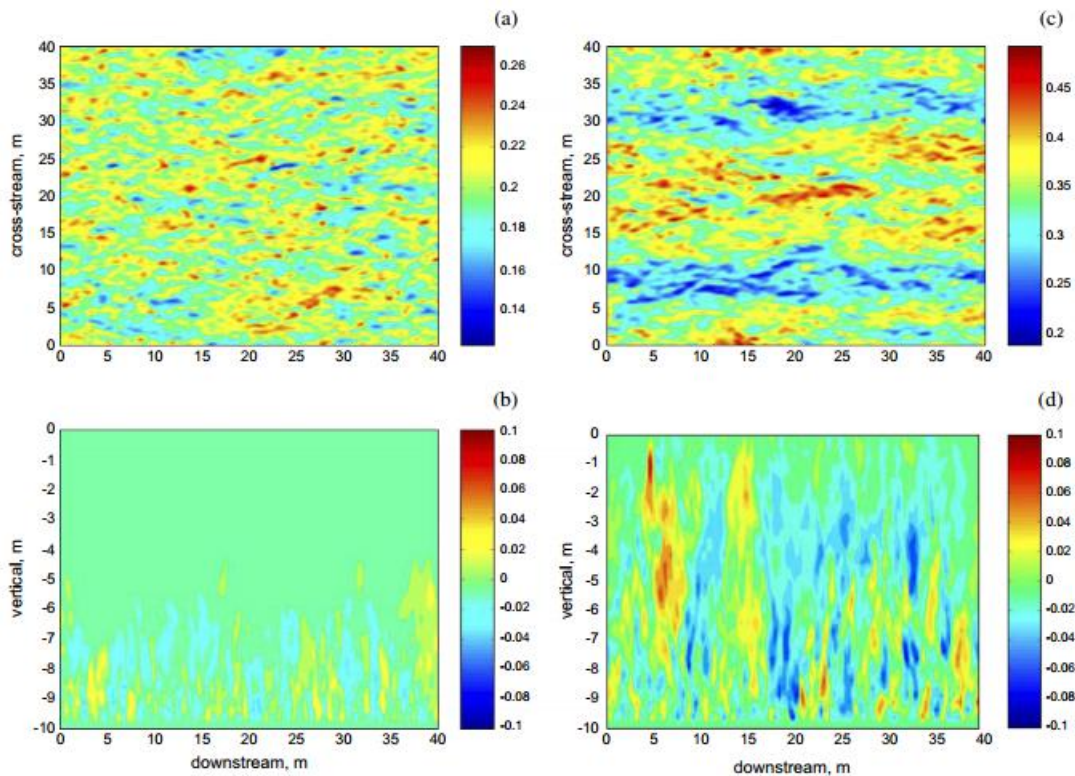
Figure 1.8: Snapshots of 3D turbulence field in a tidal boundary layer. Distributions of along-stream velocity in a horizontal plane at time t=1h (a) and t = peak tide (c), and distributions of vertical velocity in a vertical plane aligned in the downstream direction at time t = 1h (b) and t = peak tide (d). [15]. ©Elsevier. Reprinted with permission [see Appendix D].

In this test, velocity profiles again identified the generation of large turbulent eddies on a vertical plane, increasing in width and height as the flood tide peaked until they filled the full height of

18

the domain. At maximum tidal velocity the mean velocity profiles show near total mixing. The cellular structures were also visualized on horizontal (Figures 1.8a and1.8c) and vertical (Figures 1.8b and1.8d) planes in the flow. At peak tide, the distribution of along-stream velocity in a horizontal plane 2 m above the bottom boundary shows the formation of elongated streak structures, similar to those corresponding to Couette cells. As in the Couette case, these streaks accompany full-depth vertical motion visible on vertical planes in the flow, reaching the upper and bottom surfaces of the flow domain. Note that these full-depth structures are not visible when the along-stream velocity is weak in Figures 1.8a and 1.8b. The colormaps suggest that the turbulent cells grow in horizontal scale during peak and ebb tide and decay as flow decelerates between the two. It was also noted that the turbulence field dissipates if its not sustained by new shear production from the boundary.

These results exhibit the generation of full depth rotating cell structures similar to those found in the wind-driven flow without LC of [30], suggesting that both wind and tidal forcing can generate large scale rotating structures similar to the roll cells of a Couette flow and the surface wave-current induced Langmuir cells. These results lead us to investigate how such tidally-driven motions may interact with other sources of turbulence in a shallow coastal domain such as convection.

1.2 Aims and Objectives

In the previous few sections some of the primary mechanisms capable of generating large turbulent structures in a shallow domain have been briefly outlined. In field observations of both the UOML and shallow coastal shelves however, there may often be more than one mechanism contributing to vertical mixing. It is rare in a natural environment that one forcing mechanism alone will be active at any one time.

19

Some of the studies outlined above have been able to consider the effects of multiple forcing mechanisms acting simultaneously on the flow region, for example in [8], the surface buoyancy flux was observed to be stabilizing in the day (hence undergoing heating), and destabilizing at night (hence undergoing cooling). The surface heat flux varied between approximately -200 and +200 W/m^2. In this instance the observation was that the Langmuir supercells (LSC) were not significantly altered in structure or strength during varying surface heat fluxes. On the other hand, in the observations in Chesapeake Bay of [26], it was found that a destabilizing surface heat flux of 400 W/m^2 is able to augment the intensity and coherence of the observed circulations somewhat.

In 2011, Kukulka et al. [11] investigated the impact of cross-wind tidal forcing on full-depth Langmuir cells in a domain representative of a shallow, fully mixed coastal water column similar to [30]. Here the tidal force was constant, acting in the cross-wind direction, perpendicular to the surface wind stress. The findings of the study indicated that under a cross-wind current representative of the tide, the full depth cells become distorted, less coherent and weaker. The model considered two cases, one with weak wind stress, and one with strong wind stress. Where the wind stress was weaker, the cells were less sustainable under the cross-stream current than in the stronger wind stress case. In [17], Martinat et al. (2011) considered a flow configuration similar to that of [11], featuring a surface wind stress in the downstream direction and again a constant tidal cross-wind pressure gradient. In this case however, when compared to a case with wind stress only (without tidal forcing), very similar results were found, suggesting the breakdown and distortion found in the results of [11] is absent. The reason for this discrepancy in the results of the two tests is ultimately unknown, although in the LES conducted in [11] the wavelength of the surface gravity waves generating LC was less than half that applied in [17], perhaps causing a decrease in strength or stability of the LC.

20

As mentioned, in laboratory experiments and field data collection it proves to be extremely time consuming and expensive to find or reproduce a specific set of variables for a prolonged period of time. Even from these simple examples, it can be seen that the complex nature of natural ocean flows and the wide range of constantly changing variables at play makes it highly challenging to determine which individual mechanisms play a role in generating large-scale turbulence and to identify their respective strengths. The benefit of numerical simulation techniques is the potential to isolate these individual causes of turbulence in order to develop a more comprehensive under-standing of their effects and aid a more thorough analysis of both existing and future field data. The better understanding of the impact of various environmental influences including wind stress, sur-face waves, tidal forcing and heat fluxes on turbulent structures will allow improved understanding of vertical mixing processes in coastal oceans. With this knowledge, improved turbulence parame-terization models may be developed for analysis of the behavior of coastal ecosystems, surface gas exchanges and general ocean circulation models which combine chemical and biological processes for climate change studies.

It is important to reiterate that in ocean flows global currents and other flow phenomena can lead to considerable mixing and redistribution of flow properties on a large scale, but for our purposes we consider only localized mixing processes affecting vertical motion throughout the water column in domains not exceeding tens of meters.

Despite the great contributions made by the studies outlined in this introductory chapter to the field of knowledge on turbulent motion in tidal boundary layers and fully mixed coastal regions, there are numerous further developments still to be made. Several combinations of flow character-istics remain unexplored but may have significant effects on full-depth turbulent structures. Below in Table 1.1 can be seen a summary of the key features of some major studies to assist in high-

lighting where gaps in testing persist. For example, as existing LES studies of fully-mixed shallow domains have primarily maintained focus on surface heating or the case in which a density difference is fixed between the upper and lower surfaces, it remains to be seen in what manner a constant surface cooling flux generates turbulent buoyant motion in a shallow shelf region driven by a tidal force in the absence of wind and wave-forcing. We may also wish to investigate what effect such convection can have on pre-existing Langmuir circulation at particular wind and wave strengths without the influence of other external factors. Furthermore, how do we quantify the effect of a crosswind tide on existing full-depth Langmuir cells in a manner which can resolve the cause of discrepancies in results of earlier studies?

Table 1.1: Pre-tested forcing mechanisms in ocean flows.

Author/Year	Flow	Tidal body force	Wind stress	CL (Langmuir) forcing	Stratification
Tejada-Martinez and Grosch (2007)	Wind and Langmuir-forced	N	Y	Y	N
Li et al. (2004)	Tidally-forced	Streamwise oscillating	N	N	N
Kukulka et al. (2011)	Wind, tidal and Langmuir-forced	Cross-stream constant	Y	Y	N
Martinat et al. (2011)	Wind, tidal and Langmuir-forced	Cross-stream constrant	Y	Y	N
Taylor et al. (2005)	Tidally-forced	Streamwise constant	N	N	Stable – constant surface heat flux
Armenio and Sarkar (2002)	Channel flow between walls	Streamwise constant	N	N	Stable – constant density difference between walls
Skyllingstad et al (1995)	Surface mixed layer over pycnocline	N	Y	Y	Stable and unstable

As can be seen, there are many questions which remain unanswered when considering the impact of wind, wave and tidal forcing characteristics on secondary flow structures. As such, the purpose of the present work is to bridge these gaps in knowledge and further develop our present understanding of the behavior of turbulent structures in the shallow coastal ocean under a variety of forcing mechanisms. A series of simulations will be carried out, each with their own

22

respective set of forcing conditions, to assess the role of each mechanism in generating turbulence both independently and in conjunction with others. Three basic problem definitions to be used in testing can be defined as

a) A simple open channel flow driven by a constant tidal body force and featuring zero surface wind stress - representative of a tidal boundary layer or a shallow coastal domain in the absence of wind.

b) A flow driven by a constant surface wind stress but without tidal or wave forcing.

c) A flow accounting for the action of both surface wind and wave forcing via the use of the Craik-Leibovich (CL) vortex force, representing the mechanism that generates Langmuir circulation.

The results from the application of further environmental forcing mechanisms to these basic problem setups will be divided into the following results chapters:

- Chapter 4: Preliminary tests - Basic problem definitions as outlined above without any additional forcing mechanisms.

- Chapter 5: Simple tidal channel flow and wind-driven flow under the application of a destabilizing surface cooling flux.

- Chapter 6: Wind-driven flow with LC under the application of a destabilizing surface cooling flux.

- Chapter 7: Wind-driven flow with LC under the application of crosswind tidal forcing.

- Chapter 8: Wind-driven flow with LC under the application of a stabilizing surface heat flux.

23

Simulations will be performed of turbulent flow and associated vertical mixing with the above forcing mechanisms in a domain representative of the shallow coastal ocean, approximately 10 to 30 meters in depth and sufficiently far off shore that the land-ocean boundary does not significantly affect the flow behavior. This will be done using a large-eddy simulation (LES) method; solving the governing Navier-Stokes equations over a finite grid designed to capture the large, energy containing turbulent scales, and employing a dynamic Smagorinsky model to account for the smaller, sub-grid scales. Following this, a variety of statistical flow features will be analyzed to allow the clear presentation of evidence of turbulent vertical mixing.

It is hoped that the findings of these tests will allow us to analyze the impact of previously either unconsidered or insufficiently analyzed variable combinations on the large full-depth turbulent structures in shallow coastal shelves. This will bridge gaps in existing research on the behavior of turbulent coastal ocean flows under varying environmental conditions. It is hoped the observations may be relevant to several external interest groups who may require more accurate parameterizations of flow behavior to aid their understanding of pollutant dispersal, sediment suspension or any of the other potential applications of this information.

Chapter 2:

Modelling Turbulence

2.1   Introduction to Turbulence

When describing a flow as turbulent, we refer to a flow which is chaotic and highly irregular. Unlike in a simple laminar flow, particle paths are erratic and feature rapid variation of velocity. Most kinds of fluid flow feature some level of turbulent mixing (and corresponding momentum, heat and mass transfer), with the tendency to become turbulent typically increasing with decreasing viscosity of the fluid in question.

The mixing induced by a turbulent flow can be attributed to the interaction of turbulent 'eddies', defined as regions or pockets of fluid elements undergoing turbulent motion which vary in scale from small enough as to be almost invisible to large enough to entrain a significant portion of the flow. Despite this variation in scale, an eddy by definition is, even at its smallest, macroscopic in size, meaning they are significantly larger than the size of an average molecule in the flow.

Eddies are often associated with rotation (or vorticity), particularly near boundaries, and they can change shape and size as they move with the flow. An energy cascade process occurs whereby the larger eddies break down into smaller eddies, transferring their kinetic energy down the scale spectrum until it can be dissipated by viscosity. For a more complete description of the fundamental features of turbulent fluid flows, the reader is directed to [6].

25

2.2 Numerical Approaches

A fluid system considered in terms of classical mechanics (a scale larger than the molecular level) will be governed by the fundamental Navier-Stokes equations, to be discussed at length in Chapter 3, which describe the motion of fluid substances by a momentum balance in each spatial direction. An approximation to the solution of these equations requires the discretization of the flow domain into a meshed structure, such that the equations can be solved at a set of distinct points.

There are several methodologies, varying in computational cost and accuracy, for solving the governing equations in this manner. As mentioned, turbulent motion is made up of eddies which can vary greatly in size. To determine which method to use for a particular purpose, it is necessary to determine which of these scales we wish to computationally resolve. Consider the characteristic length scale of a large turbulent eddy, L, often dependent on the flow geometry and domain restrictions; for example, in a turbulent channel flow L may be of the order of the depth of the channel. Using this length scale L in our definition of a Reynolds number

$$Re = \frac{UL}{\nu} \tag{2.1}$$

and noting that the number of grid points N required to accurately resolve small scales of turbulence in 3-dimensions is

$$N \approx Re^{9/4} \tag{2.2}$$

26

we can see that, for a typical environmental flow in which the Reynolds number can be on the order of millions, the computational cost will be completely infeasible. For further detail of this calculation of N, the reader is directed to [1].

2.2.1 Direct Numerical Simulation (DNS)

Direct numerical simulation (or DNS) is an approach in which all scales of turbulence from the smallest dissipative scales to the largest eddies on the order of the domain size are fully resolved. In order to achieve this, the mesh used must be dense enough (that is, with small enough distance between meshpoints), and the timestep small enough to capture all the turbulent dynamics in the flow including even the smallest, most rapidly changing eddies. This is a high accuracy approach and does not require any model or parameterization of unresolved scales, however for a high turbulence flow such as that described in the shallow ocean, DNS is computationally prohibitive.

2.2.2 Reynolds Averaged Navier-Stokes Simulation (RANSS)

As an alternative to DNS, it is possible to directly calculate the time average of the solution, while modelling the effect of the turbulence via a turbulent stress or Reynolds stress term in the momentum equations. To do this, time averaging of the Navier-Stokes equations is applied such that all flow properties are separated into a time-averaged, mean component, and their fluctuation component. This technique is known as the Reynolds Averaged Navier-Stokes (RANS) method. In modelling the turbulent fluctuations as opposed to computationally resolving them, some level of accuracy is dependent on the turbulent model used to parameterize the fluctuations. As such, although this technique is computationally more efficient, significant accuracy is lost compared

27

to DNS. Furthermore, this approach only computes for the mean component of the flow whereas DNS captures all of the turbulent scales.

2.2.3 Large Eddy Simulation (LES)

To summarize, the DNS approach is too computationally expensive for our resources, and the RANS approach significantly limits the resolution and consequently the thoroughness of the description of potentially significant flow phenomena.

Large eddy simulation (LES), to be applied in the present study, is a technique used to resolve the larger, more energetic eddies in a turbulent flow and model the average motion of the smaller scales by introducing additional terms to the governing equations. In LES the small scales which are only modeled as opposed to resolved are independent of the flow geometry; they depend only on viscosity and receiving energy from larger scales instead of being affected by boundary conditions and the mean flow. This facilitates the modelling or parameterization of these scales in the sense that a model is universal and thus can be used for any flow condition. The use of LES serves to balance efficiency with accuracy by reducing the computational cost associated with a full resolution of the problem, but still resolving the larger turbulent eddies that contribute most to the turbulent kinetic energy. LES is more practically useful than DNS particularly for complex geometries and highly turbulent flow configurations. Additionally, it can simulate flows at higher Reynolds numbers than those possible with DNS given the cheaper computational costs.

For a more detailed description of each of the above approaches, the reader is directed to [24]. A more thorough discussion of the LES method to be used in the present work will follow in Chapter 3.

Chapter 3:

Computational Methodology

3.1 Governing Equations

The governing continuity, Navier-Stokes and advection-diffusion equations for a Newtonian, incompressible flow are defined as

$$\frac{\partial u_i}{\partial x_i} = 0 \tag{3.1}$$

$$\rho \frac{Du_i}{Dt} = -\frac{\partial p}{\partial x_i} + \nu \frac{\partial^2 u_i}{\partial x_j^2} - \rho g \delta_{i3} \tag{3.2}$$

$$\frac{DT}{Dt} = \kappa \frac{\partial^2 T}{\partial x_j^2} \tag{3.3}$$

where for now these are in dimensional form, temporarily excluding spatial filtering associated with LES. Note that κ is the thermal diffusivity. The density ρ and temperature can be related through an equation of state, as will be detailed further below. Here, the gravity vector (with magnitude g) points in the negative x_3 direction (i.e. vertically downwards). Using a simple

29

decomposition we can define the pressure (p), density (ρ) and temperature (T) according to

$$p = p_0(x_3) + p*$$

$$\rho = \rho_0 + \rho* \tag{3.4}$$

$$T = T_0 + \theta$$

where p_0, ρ_0 and T_0 are reference state static terms and $p*, \rho*$ and θ are (small) anomalies, or variations from this state. These anomalies are the values for which we wish to solve. Note that the Boussinesq approximation may be applied when density variations are sufficiently small (such that $\rho* \ll \rho_0$ and $\theta \ll T_0$). Applying this approximation and the above decomposition, and discarding the terms which are in hydrostatic balance (i.e. $\frac{dp_0}{dx_3} = -\rho_0 g$), leads to a momentum equation of the form

$$\frac{Du_i}{Dt} = -\frac{1}{\rho_0} \frac{\partial p^*}{\partial x_i} + \nu \frac{\partial^2 u_i}{\partial x_j^2} - \rho^* \frac{g}{\rho_0} \delta_{i3} \tag{3.5}$$

and our temperature equation will now be in terms of temperature fluctuation θ,

$$\frac{D\theta}{Dt} = \kappa \frac{\partial^2 \theta}{\partial x_j^2} \tag{3.6}$$

Note that the equation of state between dimensional variables ρ and T is given by

$$\rho = \rho_0(1 - \beta(T - T_0)) \tag{3.7}$$

30

where β is the coefficient of thermal expansion [14]. When written in terms of our decomposed variables defined above, this gives

$$\rho^* = -\rho_0 \beta \theta \tag{3.8}$$

which allows us to write the final term in Eqn. 3.5 in terms of temperature θ such that

$$\frac{Du_i}{Dt} = -\frac{1}{\rho_0}\frac{\partial p^*}{\partial x_i} + \nu\frac{\partial^2 u_i}{\partial x_j^2} + \beta g \theta \delta_{i3} \tag{3.9}$$

Following [3] we can further decompose our temperature θ into two components as follows

$$\theta = \theta_b + \theta_f \tag{3.10}$$

where

$$\theta_b = \langle \theta \rangle_{x_1, x_2} \tag{3.11}$$

which is the bulk temperature: the total temperature variation averaged over the horizontal directions (homogeneous directions) in our flows to be considered in upcoming chapters. Applying this decomposition to the momentum equation and noting the pressure can be redefined as the pressure remaining after removing the component in hydrostatic balance with this new bulk temperature field, we are left with

$$\frac{Du_i}{Dt} = -\frac{1}{\rho_0}\frac{\partial p^*}{\partial x_i} + \nu\frac{\partial^2 u_i}{\partial x_j^2} + \beta g \theta_f \delta_{i3} \tag{3.12}$$

31

We non-dimensionalize the governing equations 3.6 and 3.12 with the water column half-depth δ. u_τ is a friction velocity associated with either an applied wind stress or a bottom wall (bed) friction velocity depending on the flow configuration. The absolute value of the imposed free-surface temperature gradient is defined to be Q/k, the ratio of the surface heat flux to the thermal conductivity. This leads to our new, non-dimensional momentum equations

$$\frac{Du_i}{Dt} = -\frac{\partial p^*}{\partial x_i} + \frac{1}{Re_\tau}\frac{\partial^2 u_i}{\partial x_j^2} + Ra_\tau \theta_f \delta_{i3} \tag{3.13}$$

The third term on the right hand side of the momentum equation is a buoyancy term in which the non-dimensional Rayleigh number Ra_τ represents the strength of surface buoyancy relative to shear. This Rayleigh number and the Reynolds number (representing the ratio of inertial to viscous forces) are defined as

$$\begin{aligned} Re_\tau &= \frac{u_\tau \delta}{\nu} \\ Ra_\tau &= \frac{\beta g \delta^2}{u_\tau^2}\left|\frac{d\theta}{dx_3}\right|_s \end{aligned} \tag{3.14}$$

where again u_τ and δ are the wall friction velocity and half-depth as described above, ν is the kinematic viscosity, g gravity and β the coefficient of thermal expansion. The $\left|\frac{d\theta}{dx_3}\right|_s$ term represents the absolute value of the prescribed vertical temperature gradient at the surface which, as mentioned, we define to be Q/k.

The non-dimensional temperature equation is given by

$$\frac{D\theta}{Dt} = \frac{1}{PrRe_\tau}\frac{\partial^2\theta}{\partial x_j^2} \tag{3.15}$$

32

where the Prandtl number is the ratio of kinematic viscosity to thermal diffusivity κ, and is defined as

$$Pr = \kappa/\nu \tag{3.16}$$

Note that the equations outlined above are in their most basic form; as the dissertation progresses and more complex problems are considered, any additional terms required in the governing equations, and the boundary conditions imposed, will be discussed in their respective sections.

To complete the basic governing equations to be solved in our LES, we must now apply the spatial filtering as mentioned in Chapter 2.

3.2 Spatial Filtering

As mentioned earlier, turbulent flow contains eddies over a wide range of scales. The purpose of the LES is to resolve the larger eddies in the flow and model or parameterize the effect of the smallest ones on these larger ones to improve computational time and efficiency relative to DNS. To do this a low-pass spatial filter can be applied to the Navier-Stokes equations which damps scales smaller than the filter width, resulting in a filtered set of governing equations. Variables can be decomposed into a resolved (filtered) component denoted by an overbar, and a sub-grid scale component, temporarily denoted with superscript SGS for clarity, of smaller size than the low-pass filter width:

$$F = \bar{f} + f^{SGS} \tag{3.17}$$

33

The whole process of LES is based on this concept of 'filtering out' the smaller scales of turbulence, i.e those which have the least energy, and modeling or parameterizing these residual scales by an extra term in the governing equations. This means the computational solver will only be capturing or resolving the larger scales of turbulence with the most energy which require lesser grid resolution than the residual scales thus making the computation cheaper.
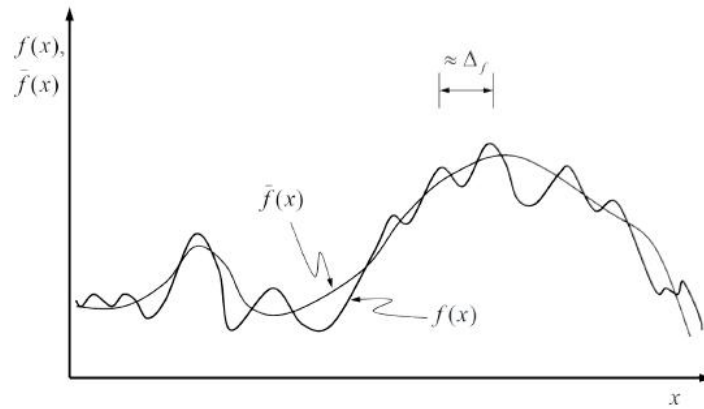
Figure 3.1: Sketch of function $f(x)$ and its filtered component $\bar{f}(x)$ where the filter width is Δ_f. ©A. E. Tejada-Martinez. Reprinted with permission [see Appendix D].

Theoretically a filtered variable can be defined as the integral over the whole spatial domain of the unfiltered variable multiplied by a filter kernel $G(x,y)$:

$$\bar{F}(x,t) = \int_\Omega G(x,y)f(y,t)dy \qquad (3.18)$$

This filtering operation (examples include a basic top hat kernel, or a Gaussian distribution kernel) serves to 'smooth out' the function by dampening the contributions to the variable coming from spatial scales smaller than the filter width.

In 1941, Andrei N. Kolmogorov derived a formula for the energy spectrum of turbulence [10]. This spectrum (see Figure 3.2) provides the distribution of energy among turbulent vortices (or
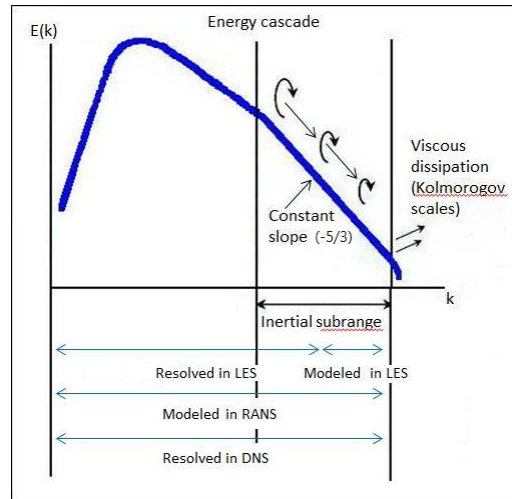
Figure 3.2: Energy spectrum of turbulence.

eddies) by plotting energy E against wavenumber k, where the relationship between wavenumber and wavelength (representing the spatial dimension of the eddy) is given by $k = 2\pi/\lambda$. Eddies which contain the most energy are typically characterized by a low temporal frequency and a large spatial scale; eddies which contain the least energy are typically characterized by a high temporal frequency and a small spatial scale.

This energy spectrum features an "inertial subrange" in which the energy received from the larger scales is in balance with the energy passed down to the smaller scales. Here, there is no external energy being added to these inertial subrange scales, and thus the slope of the energy spectrum in this range remains constant. The aim of LES is to resolve into the inertial subrange. Scales within the inertial subrange are universal, thus a model or parameterization of these scales (required for the LES) should be applicable to any flow configuration.

35

3.3   Sub-Grid Scale Terms

We have established that the application of a spatial filter leads to the Navier-Stokes equations being solved only for the large, energy containing scales. These equations are

$$\frac{\partial \bar{u}_i}{\partial t} + \frac{\partial \bar{u}_i \bar{u}_j}{\partial x_j} = -\frac{\partial \bar{p}}{\partial x_i} + \frac{1}{Re_\tau}\frac{\partial^2 \bar{u}_i}{\partial x_j^2} + \frac{\partial \tau_{ij}^{SGS}}{\partial x_j} + Ra_\tau \theta_f \delta_{i3} \tag{3.19}$$

and

$$\frac{\partial \bar{\theta}}{\partial t} + \frac{\partial \bar{\theta}\bar{u}_j}{\partial x_j} = \frac{1}{Re_\tau Pr}\frac{\partial^2 \bar{\theta}}{\partial x_j^2} + \frac{\partial q_j^{SGS}}{\partial x_j} \tag{3.20}$$

where the overbar denotes a spatially filtered variable.

For our purposes, the domain discretization serves as the filter, since the grid size directly determines the eddy scales that are fully resolved. We are solving the governing equations at discrete points on a pre-defined grid, hence we can define a grid coarseness that captures and resolves turbulent motion only of these defined 'large' scales. Essentially the low energy eddies with scales smaller than filter width Δ (the distance between computational grid points) can be imagined to fall through the gaps in the grid points. Hence, the solution of the governing equations features only spatially filtered variables.

In the above equation, the superscript "SGS" terms represent the contribution of the sub-grid scales. To demonstrate where these additional terms come from, consider that the material derivative on the left hand side of our original Navier-Stokes and temperature advection-diffusion equations (Eqn. 3.12 and Eqn. 3.14, respectively) featured terms of the form

36

$$\frac{\partial(u_i u_j)}{\partial x_j} \tag{3.21}$$

and

$$\frac{\partial(\theta u_j)}{\partial x_j} \tag{3.22}$$

Applying the filter to these terms, we will generate

$$\frac{\partial}{\partial x_j}(\overline{u_i u_j}), \quad \frac{\partial}{\partial x_j}(\overline{\theta u_j}) \tag{3.23}$$

Now, notice the value of these $\overline{u_i u_j}$ and $\overline{\theta u_j}$ terms is unknown as the turbulent residual (sub-grid) scales are not resolved; the unfiltered velocity u_i and temperature θ are not found by the simulation as the code is resolving only the filtered variables. Next, define

$$\overline{u_i u_j} = \overline{u_i u_j} + \bar{u}_i \bar{u}_j - \bar{u}_i \bar{u}_j \tag{3.24}$$

and hence

$$\frac{\partial}{\partial x_j}\overline{u_i u_j} = \frac{\partial}{\partial x_j}(\overline{u_i u_j} + \bar{u}_i \bar{u}_j - \bar{u}_i \bar{u}_j) \tag{3.25}$$

which can then be rearranged to give

$$\frac{\partial}{\partial x_j}(\bar{u}_i \bar{u}_j) + \frac{\partial}{\partial x_j}(\overline{u_i u_j} - \bar{u}_i \bar{u}_j) \tag{3.26}$$

37

Now, this first term remains on the left hand side of the momentum equation, and the second term gives rise to

$$\tau_{ij}^{SGS} = -\overline{u_i u_j} + \bar{u}_i \bar{u}_j \qquad (3.27)$$

hence we have a new term $\frac{\partial \tau_{ij}^{SGS}}{\partial x_j}$ on the right hand side of the momentum equation which features the contribution of the unresolved sub-grid scales on the resolved scales, and hence represents our SGS stress. A similar procedure is used to generate the equivalent sub-grid scale fluxes for the temperature equation:

$$q_j^{SGS} = -\overline{\theta u_j} + \bar{\theta} \bar{u}_j \qquad (3.28)$$

Now we still have a closure problem which arises from not knowing the value of these residual (SGS) stresses and fluxes. This closure problem must be solved by modeling or approximating their contribution to the flow. For the purposes of the present work, the models to be considered will be the widely used dynamic Smagorinsky model, and an adaptation of this, a dynamic mixed model, both of which are described further in Appendix C.

3.4 Spatial and Temporal Discretization

Based on the previous sections the complete and final non-dimensional governing Navier-Stokes equations for momentum and temperature advection-diffusion in our incompressible flow are now, respectively,

$$\frac{\partial \bar{u}_i}{\partial x_i} = 0 \qquad (3.29)$$

38

$$\frac{\partial \bar{u}_i}{\partial t} + \frac{\partial \bar{u}_i \bar{u}_j}{\partial x_j} = -\frac{\partial \bar{p}}{\partial x_i} + \frac{1}{Re_\tau}\frac{\partial^2 \bar{u}_i}{\partial x_j^2} + \frac{\partial \tau_{ij}^{SGS}}{\partial x_j} + Ra_\tau \theta_f \delta_{i3} \tag{3.30}$$

$$\frac{\partial \bar{\theta}}{\partial t} + \frac{\partial \bar{\theta} \bar{u}_j}{\partial x_j} = \frac{1}{Re_\tau Pr}\frac{\partial^2 \bar{\theta}}{\partial x_j^2} + \frac{\partial q_j^{SGS}}{\partial x_j} \tag{3.31}$$

An overbar denotes that the spatial filter has been applied in order to perform LES. $\bar{p}$ and $\bar{u}_i$ are the dimensionless filtered pressure and velocity and τ_{ij}^{SGS} and q_j^{SGS} are the subgrid-scale terms.

The governing equations are solved using the second-order time accurate semi-implicit fractional step method described in [30]. This involves solving a form of the momentum equations to get an approximation to the velocity, then solving a form of Poisson equation to give the pressure as well as a correction to the velocity field to enforce continuity. For the spatial discretization, the horizontal derivatives (x_1, x_2) are treated spectrally with Fast Fourier transforms and restricted to periodic boundaries. The vertical derivatives on the other hand make use of high order compact finite differences.

In the following chapters, additions to the governing equations to incorporate tidal body forces, wind and wave forcing and to impose statistical steadiness of the turbulence resolved will be described in detail as they arise in the respective problems.

Chapter 4:

Results: Preliminary Tests

In the sections that follow, each individual test will be outlined in terms of its particular forcing conditions, contributing terms to the governing equations, flow domain and a thorough statistical analysis of the resulting flow properties by means of a variety of post-processing and visualization techniques.

Initially the basic problem characteristics that apply to all the simulations in the present work, such as the fundamental domain and constant boundary conditions, will be introduced. Following this, the three basic problems described earlier (in section 1.2), driven by a) a constant tidal pressure gradient ("PG-driven"), b) a constant surface wind stress ("Wind-driven"), and c) a constant wind stress and wave (Langmuir) forcing, will be introduced. In the latter problem, Langmuir forcing which generates LC is represented by the Craik-Leibovich (C-L) vortex force resulting from wave-current interaction. The key features of a fully developed flow with each of these respective mechanisms acting in isolation before application of the combinations of characteristics of interest to the present work will be briefly summarized in this chapter, to aid the clear understanding of the remaining results. A more detailed analysis of their properties will follow in Chapters 5-8.

Chapters 5 and 6 will discuss in detail the findings of the application of surface cooling to each of the three fundamental flows. Chapters 7 and 8 will focus on the flow featuring both wind and wave forcing and hence characterized by Langmuir circulation: effects of crosswind tidal

forces and the application of a surface heating flux on LC will be considered in these two chapters respectively.

4.1 Domain

In most flows, the computational domain is of dimensions $4\pi\delta$ x $(8/3)\pi\delta$ x 2δ in the x_1 (downstream), x_2 (cross stream) and x_3 (vertical) directions respectively, where recall δ is the water column half-depth. In dimensional terms this corresponds to approximately 10 m in depth, 60 m in downstream length and 40 m in cross-stream width. Periodicity is assumed in both the latter two directions (x_1 and x_2), representing a flow sufficiently far off-shore as to not be affected by lateral boundaries. The bottom wall in all flows is no-slip and adiabatic, and zero normal flow is imposed at the surface. The flow domain will be shown for each test and set of forcing conditions in their respective sections.

Simulations are typically performed on a computational domain discretized with 32 uniformly spaced points in x_1, 64 uniformly spaced points in x_2 and 97 stretched points in x_3. Based on the grid-size sufficiency assessments of Tejada-Martinez and Grosch (2007) [30], it was found that this grid size is sufficiently fine that continued decreasing of the grid cell size will not lead to significant differences in full-depth turbulence structure. Furthermore, this resolution is able to capture the largest scales within the inertial subrange. One method for assessing the accuracy of our solution approximation on this grid is to consider Reynolds-averaged balance equations for the momentum and temperature; the sum of computed terms of these balances can be compared to theoretical values to demonstrate the level of agreement. Details of these balances can be found in Appendix B.

41

Our simulations resolve molecular sublayers and corresponding large velocity and temperature gradients respectively at the bottom and surface boundaries. As such, we cluster the computational grid points in these regions, hence making the grid 'stretched' or finer. Using a mapping hyperbolic function we can stretch our grid in these regions in the vertical direction only and symmetrically about the mid-depth of the water column; further detail of this function is provided in Appendix A.

4.2 PG-Driven

Initially we can consider a simple flow domain with the no-slip, adiabatic bottom wall as mentioned above, a surface with zero shear stress and no-penetration ($\bar{u}_3 = 0$), and driven by a pressure gradient representative of a tidal boundary layer similar to that in the work of Li et al [15] but over a short time period in which tidal forcing is roughly constant. Hence, the flow is driven by a constant, uniform pressure gradient aligned with the x_1-axis. This flow and computational domain are sketched in Figure 4.1.
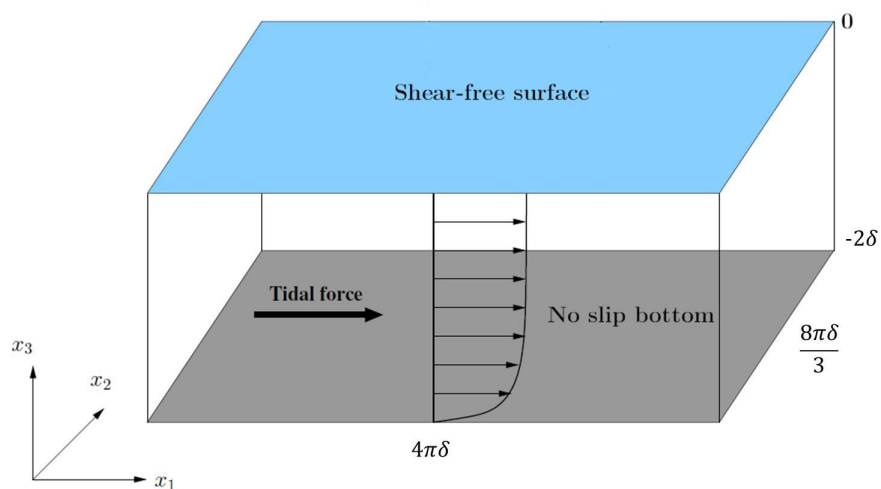

Figure 4.1: Problem domain: PG-driven flow

42

The body force (i.e. the tidal force) resulting from this streamwise pressure gradient is calculated such that the Reynolds number based on bottom friction velocity u_τ and water column half depth δ is $Re_\tau = 395$. Consider the non-dimensional, filtered momentum equation, now with this body force F acting in the downstream direction. Note that in this preliminary test, zero surface cooling is applied at the surface, corresponding to a Rayleigh number of zero, and hence the buoyancy term can be temporarily removed.

$$\frac{\partial \bar{u}_i}{\partial t} + \frac{\partial \bar{u}_i \bar{u}_j}{\partial x_j} = -\frac{\partial \bar{p}}{\partial x_i} + \frac{1}{Re_\tau} \frac{\partial^2 \bar{u}_i}{\partial x_j^2} + \frac{\partial \tau_{ij}^{SGS}}{\partial x_j} + \frac{1}{2} \delta_{i1} \tag{4.1}$$

Although turbulent flows feature highly irregular behavior of flow properties, statistical properties including time and space averages can show significantly more regular behavior. We can demonstrate the turbulence structure by considering velocity fluctuations on a vertical plane in the flow, partially averaged over the streamwise (x_1) direction and time. In our notation, note that angled brackets represent an averaged component and a prime denotes a fluctuation. Figure 4.2 shows the a) downstream, b) cross-stream and c) vertical components of these partially averaged velocity fluctuations in the form of colormaps on this two-dimensional plane.

As discussed in Chapter 1, open channel flow can be characterized by full-depth turbulent structures acting as a secondary component to the mean flow. Furthermore, recall the description of a plane Couette flow featuring counter rotating cellular structures, elongated in the downstream direction. Now, consider the center panel of Figure 4.2, and observe the presence of regions of positive and negative velocity fluctuations lining the upper and lower walls of the domain; these represent regions of convergence and divergence of velocity fluctuations at the surface and bottom of the channel. The convergence zone where negative fluctuations meet positive ones leads into

43

a coherent region of negative vertical velocity fluctuation, representing a region of down-welling visible in the bottom panel of Figure 4.2. Similarly, a bottom convergence zone in terms of the crosswind velocity fluctuation leads into a coherent region of positive vertical velocity fluctuation. These up and downwelling regions and corresponding divergence and convergence regions form a closed cellular pattern and indicate the presence of cellular structures resolved in the LES. This suggests that under neutrally stratified conditions, this constant tidal force-driven flow is characterized by full-depth, streamwise cells similar to Couette cells observed in plane Couette flow. A more detailed statistical analysis of these cellular structures present in a constant tidal force-driven flow will be provided in the next chapter, alongside quantification of the strength of these cells with respect to similar cells driven by convection.
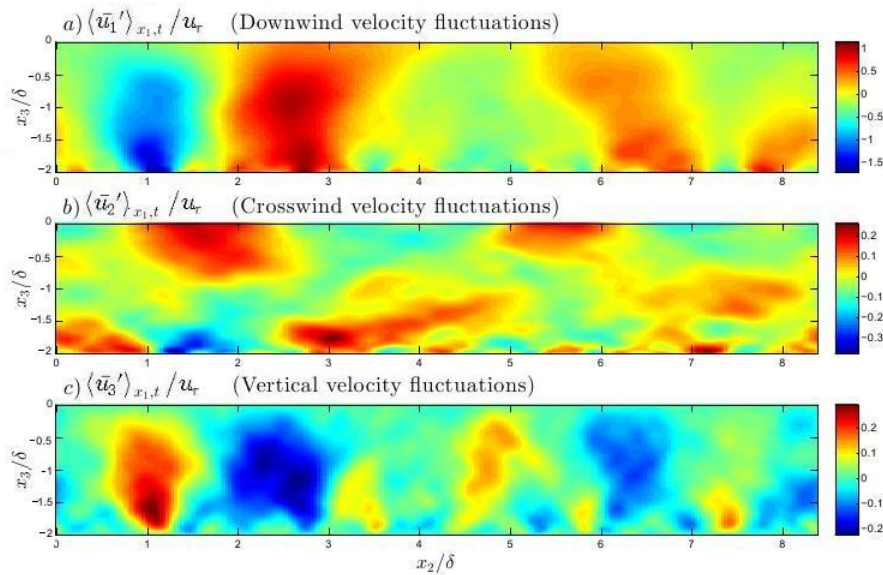

Figure 4.2: Vertical plane colormaps of velocity fluctuations: PG-driven case. Fluctuations are partially averaged in time and the downstream (x_1) direction. u_τ is the bottom stress friction velocity.

4.3   Wind-Driven

In our simple wind-driven flow, tidal forcing is not accounted for, and nor are surface wave effects (i.e. Langmuir forcing). A constant surface wind stress is applied such that the Reynolds number $Re_\tau = u_\tau \delta / \nu$ is 395 where now u_τ is the wind stress friction velocity. However, note that in this configuration with or without Langmuir forcing (shown in Figure 4.3), in the mean, the bottom (bed) stress will be equal to the wind stress. Thus in the mean the bottom friction velocity is equal to the wind stress friction velocity.
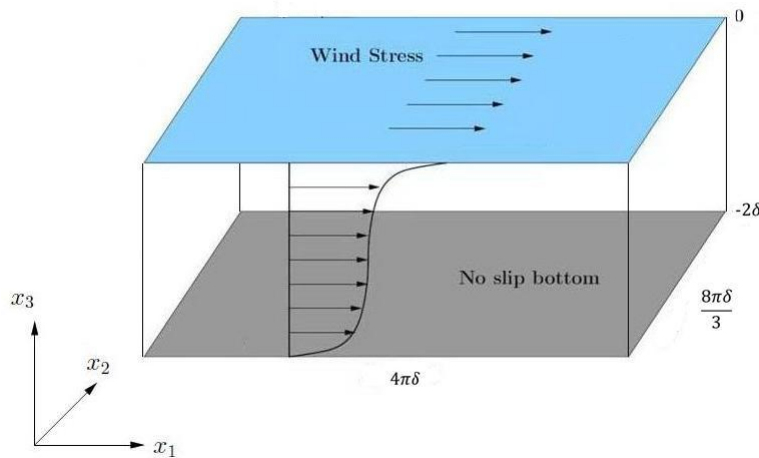
Figure 4.3: Problem domain: Wind-driven flow

Here, the only forcing mechanism is imposed as a surface boundary condition, and as such the governing equation remains as

$$\frac{\partial \bar{u}_i}{\partial t} + \frac{\partial \bar{u}_i \bar{u}_j}{\partial x_j} = -\frac{\partial \bar{p}}{\partial x_i} + \frac{1}{Re_\tau} \frac{\partial^2 \bar{u}_i}{\partial x_j^2} + \frac{\partial \tau_{ij}^{SGS}}{\partial x_j} \tag{4.2}$$

Note that the Reynolds number of 395 as used in the current problems is significantly smaller than the real world problem. As mentioned in Chapter 1, Tejada-Martinez et al (2009) [31] con-

45

ducted LES of this flow together with Langmuir forcing with $Re_\tau = 395$ representative of the shallow coastal domain used for the field measurements of Gargett at al. (2004) [8]. As validation of the appropriateness of the Reynolds number of 395 for the purposes of the study, after initial testing was complete, the resultant velocities were dimensionalized using the actual surface friction velocity observed in the field, as opposed to the one corresponding to $Re_\tau = 395$. In doing this, the results were scaled up to the real-world scale. This presented fluctuating velocities of approximately 5-8 cm/s in magnitude which were closely comparable to the results found in the field by Gargett et al. in [8]. As such, we assume that for the purposes of our simple LES flows representative of the coastal environment, we may work with the Reynolds number set as $Re_\tau = 395$.

In the present flow described through Figure 4.3, the surface shear is again able to lead to the generation of full-depth rotating cell structures secondary to the mean flow. It can be seen in Figure 4.4b that these regions of surface and bottom convergence and divergence, and full-depth regions of positive and negative vertical velocity fluctuations representing regions of up- and downwelling, again constitute a full-depth cellular pattern resolved in the LES. In this case (with wind only) there are several cells present, and the magnitude of the crosswind and vertical fluctuations are greater than that of the pressure-gradient driven case described in Section 4.2. In this case the magnitudes of the fluctuation velocities are nearly the same as those of Couette cells [21]. This suggests a constant surface wind stress is able to initiate the development of cellular structures similar to those observed in plane Couette flows ([13], [21]). These Couette-like cells are similar to those generated by a constant tidal body force in the previous section although stronger and more coherent; just over two clear cell pairs can be identified in the partially averaged velocity fluctuations on a similar vertical plane shown in Figure 4.4.
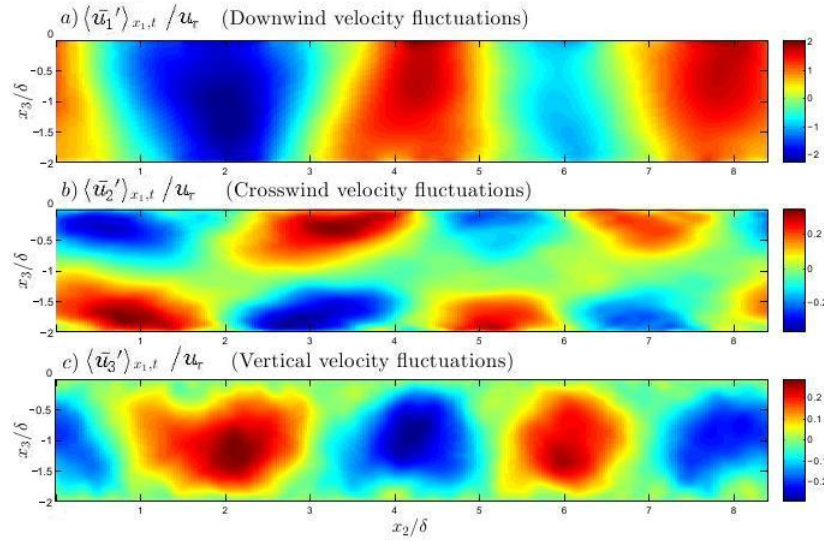
46

Figure 4.4: Vertical plane colormaps of velocity fluctuations: Wind-driven case. Fluctuations are partially averaged in time and the downstream (x_1) direction. u_τ is the wind stress friction velocity.

4.4 Wind and Langmuir-Driven

The third fundamental flow for our purposes is that driven by wind and Langmuir forcing, the latter induced by the interaction of the wind-driven current and surface gravity waves and in which a tidal body force is not present. The flow domain will be the same as Figure 4.3. In these tests, the surface waves are not resolved directly due to the high computational cost, so as mentioned in Chapter 1, we can apply a parameterization for the generation of LC. The Craik-Leibovich vortex forcing (or Langmuir forcing) mechanism was first proposed by Craik and Leibovich (1976) and consists of a term in the momentum equations modeling the interaction between the Stokes drift, driven by the surface waves, and the vertical shear of the current [5]. The C-L vortex force is the vector cross product between the Stokes drift velocity and the vorticity of the flow; the parameters in this force are the dominant wavelength and amplitude of the surface waves used to define the Stokes drift velocity profile.

47

Inclusion of the C-L force greatly reduces the complexity of the problem as it eliminates the need to resolve the surface waves giving rise to LC. Instead, the top of the flow domain is simply taken to be bounded by a flat (non-deforming) surface denoting the mean water height. As discussed in the introductory chapter, there are several examples of the use of the C-L vortex force in LES ([27], [15])

Recall our basic non-dimensional governing equation

$$\frac{\partial \bar{u}_i}{\partial t} + \frac{\partial \bar{u}_i \bar{u}_j}{\partial x_j} = -\frac{\partial \bar{p}}{\partial x_i} + \frac{1}{Re_\tau}\frac{\partial^2 \bar{u}_i}{\partial x_j^2} + \frac{\partial \tau_{ij}^{SGS}}{\partial x_j} \tag{4.3}$$

Adding a forcing term to represent the Langmuir circulation leads to the Craik-Leibovich equations

$$\frac{\partial \bar{u}_i}{\partial t} + \frac{\partial \bar{u}_i \bar{u}_j}{\partial x_j} = -\frac{\partial \bar{p}}{\partial x_i} + \frac{1}{Re_\tau}\frac{\partial^2 \bar{u}_i}{\partial x_j^2} + \frac{\partial \tau_{ij}^{SGS}}{\partial x_j} + \frac{1}{La_t^2}\varepsilon_{ijk}\phi_j^s\bar{\omega}_k \tag{4.4}$$

where La_t is the turbulent Langmuir number, the ratio of wind friction velocity u_τ to characteristic Stokes drift velocity u_s and defined as

$$La_t = \sqrt{u_\tau/u_s} \tag{4.5}$$

This value provides a measure of the strength of wind-driven shear forcing relative to wave forcing. The strength of the Langmuir cells is thus inversely proportional to La_t. For our purposes, La_t is 0.7 based on the field measurements of [8]. The characteristic Stokes drift velocity is $u_s = \omega\kappa a^2$ where ω is the dominant frequency, κ is the dominant wavenumber and a is the dominant amplitude of the surface waves. The non-dimensional Stokes drift velocity, which decays with depth, is defined

48

as

$$\phi_1^s = \frac{\cosh(2(\kappa x_3 + 1))}{2\sinh^2(2\kappa)}, \quad \phi_1^s = \phi_3^s = 0 \tag{4.6}$$

Shorter wavelength surface waves lead to a more rapid decay of the Stokes drift velocity, and hence a greater Stokes drift velocity shear at the surface. Unless otherwise stated, the characteristic wave length used in the present tests is $\lambda = 6H$, and thus $\kappa = 2\pi/\lambda = 2\pi/6H$. This and the above turbulent Langmuir number of 0.7 were both observed during the full-depth Langmuir supercell observations of [8]. Finally note that the Stokes drift also affects the pressure resulting in a modified pressure, denoted here as simply $\bar{p}$ in Equation 4.4. The interested reader is directed to [31] for details of this.

From the same vertical plane colormaps of velocity fluctuations described previously, a coherent cellular structure is again visible in the case driven by wind and Craik-Leibovich vortex forcing (see Figure 4.5). Unlike the Couette-like cells in Figure 4.4, the crosswind velocity fluctuation is characterized by surface intensification similar to Couette cells, a convergence zone where negative crosswind velocity fluctuations meet positive ones, leading into a coherent region of negative vertical velocity fluctuation. Similarly, a bottom convergence zone in terms of the crosswind velocity fluctuation leads into a coherent region of positive vertical velocity fluctuation. These regions of surface and bottom convergence and divergence, and full-depth regions of positive and negative vertical velocity fluctuations representing regions of up- and down-welling, constitute one full-depth Langmuir supercell resolved in the LES, comparable in structure to those observed in the field in [8]. Notice the increased strength, coherence and cross-stream width of this cell structure when compared to the weaker cells more comparable to Couette-like structures seen in the previous two flows.
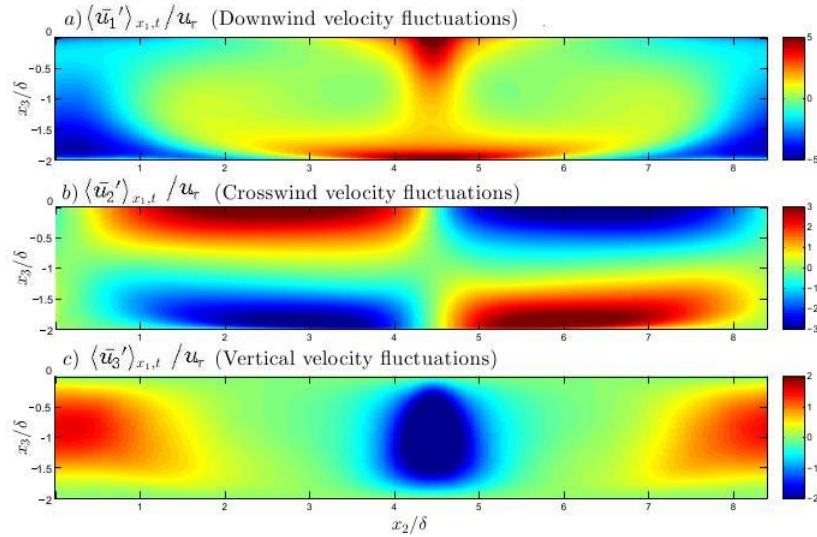
49

Figure 4.5: Vertical plane colormaps of velocity fluctuations: LC-driven case. Fluctuations are partially averaged in time and the downstream (x_1) direction. u_τ is the wind stress friction velocity.

4.5 Chapter Summary

This brief introduction to the basic problem setup and the fundamental three-dimensional full-depth (secondary to the mean flow) cellular structure present in each of our major flows of interest is intended to provide a foundation for the analysis of how forcing mechanisms acting in conjunction with each other can alter the turbulent structure of shallow domain flows. In the following four chapters, these large secondary structures will be analyzed in several ways including, but not limited to, mean velocity and temperature profiles, root mean square of velocity fluctuations and budgets of turbulent kinetic energy (TKE) and TKE components. As our combinations of forcing mechanisms of interest are applied, these results will then be compared in detail to gain a clear insight into how each forcing mechanism affects the basic turbulent structures described above.

50

Chapter 5:

Results: Surface Cooling (PG-driven and Wind-driven Flows)

The focus of this chapter will be the impact of the application of a constant surface cooling flux of varying magnitudes on our flows driven by both a pressure gradient and a constant wind stress, with a comparable study of the wind/Langmuir-driven flow to follow in Chapter 6. Initially, a summary of the manner in which this heat flux is applied in terms of the governing equations and boundary conditions will be provided.

Recall our governing equations for momentum and temperature advection-diffusion, outlined in Chapter 3:

$$\frac{\partial \bar{u}_i}{\partial t} + \frac{\partial \bar{u}_i \bar{u}_j}{\partial x_j} = -\frac{\partial \bar{p}}{\partial x_i} + \frac{1}{Re_\tau}\frac{\partial^2 \bar{u}_i}{\partial x_j^2} + \frac{\partial \tau_{ij}^{SGS}}{\partial x_j} + Ra_\tau \theta_f \hat{k} \tag{5.1}$$

$$\frac{\partial \bar{\theta}}{\partial t} + \frac{\partial \bar{\theta}\bar{u}_j}{\partial x_j} = \frac{1}{Re_\tau Pr}\frac{\partial^2 \bar{\theta}}{\partial x_j^2} + \frac{\partial q_j^{SGS}}{\partial x_j} \tag{5.2}$$

where the final term on the right hand side of Equation 5.1 is the buoyancy term featuring the Rayleigh number, which is representative of the strength of surface buoyancy relative to shear and defined as

$$Ra_\tau = \frac{\beta g \delta^2}{u_\tau^2}\frac{Q}{k} \tag{5.3}$$

51

We may additionally introduce to the temperature equation a thermal source term s designed to maintain a constant mean temperature, hence

$$\frac{\partial \bar{\theta}}{\partial t} + \frac{\partial \bar{\theta} \bar{u}_j}{\partial x_j} = \frac{1}{Re_\tau Pr} \frac{\partial^2 \bar{\theta}}{\partial x_j^2} + \frac{\partial q_j^{SGS}}{\partial x_j} + s \tag{5.4}$$

where $s = \frac{1}{2PrRe_\tau}$. We apply a constant negative temperature gradient corresponding to surface cooling. In dimensionless form this temperature gradient is -1 given the non-dimensionalizing characteristic temperature chosen in Chapter 3. Zero normal flow and zero shear stress are also imposed at the upper surface.

5.1 PG-Driven

Note to reader: a significant portion of the content of Section 5.1 was originally published in [34]. See Appendix D for permissions.

In this section the major differences in statistical equilibrium dynamics are considered between the pressure gradient driven flow with no convection-induced buoyancy and thus $Ra_\tau = 0$, the primary features of which were described in Chapter 4, and a flow with convection-induced buoyancy such that $Ra_\tau = 5000$. Note that in the $Ra_\tau = 0$ case, the temperature is subjected to the same surface boundary condition as in the case with non-zero Ra_τ (i.e. $(\partial \bar{\theta}/\partial x_3)_s = -1$). The difference between between these two cases is that for $Ra_\tau = 0$ the temperature evolves as a passive scalar when the buoyancy term is absent. The Reynolds number is set as $Re_\tau = 395$ and $Pr = 7$. The domain for this case is shown in Figure 5.1.
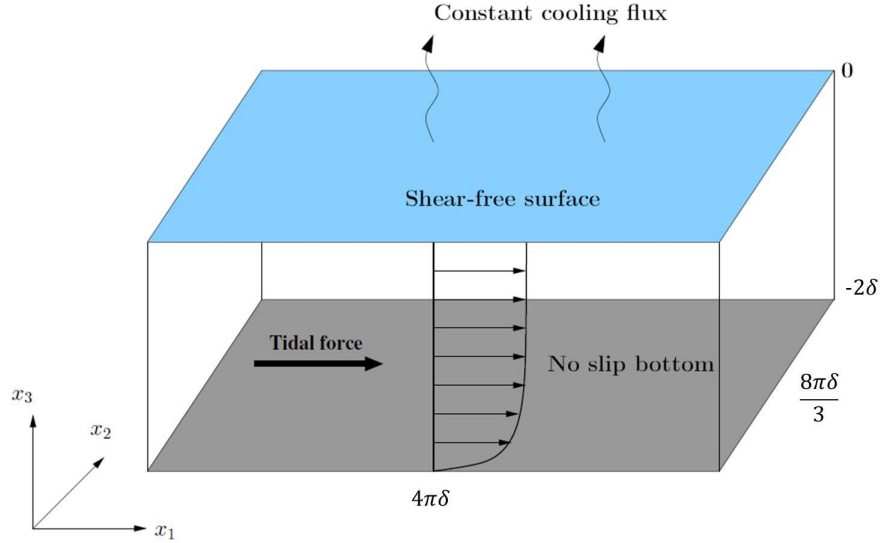
Figure 5.1: Problem domain: PG-driven flow with cooling

Most turbulent quantities analyzed are averaged over x_1, x_2 and time t. The averaging serves to decompose the quantities; for example, the velocity components are defined as $\bar{u}_i = \langle \bar{u}_i \rangle + \bar{u}'_i$ where $\bar{u}'_i$ is a resolved velocity fluctuation. Averages were obtained after the flows had reached statistical equilibrium. Note that the variables presented in the following results are dimensional and hence are scaled by a reference or characteristic scale. Most variables are scaled by the bottom friction velocity u_τ or the temperature θ^*.

We may consider the mean stream-wise velocity profiles ($u_1^+ = \langle \bar{u}_1 \rangle / u_\tau$ where u_τ is the bottom friction velocity) as a function of depth both in standard units (Figure 5.2a) and in wall units (Figure 5.2b), the latter with emphasis on the viscous sub-layer ($x_3^+ \leq 5$), the buffer layer ($5 \leq x_3^+ \leq 30$) and the log layer ($30 \leq x_3^+ \leq 100$). Profiles are shown for tidally driven flows with $Ra_\tau = 5000$ and $Ra_\tau = 0$. Considering first the full column depth, it can be seen that in the $Ra_\tau = 0$ flow the gradient of the velocity profile remains positive and non-constant. Under application of the surface cooling-induced buoyancy, increased turbulent mixing leads to full depth homogenization, inducing a roughly uniform mean stream-wise velocity profile over the bulk region of the flow.

53

The log law profile representative of the near-wall behavior expected of a typical turbulent flow at a solid boundary is indicated by the dotted line in Figure 5.2b. The flow with $Ra_\tau = 0$ is characterized by this well developed log law. The increase to $Ra_\tau = 5000$ leads to a deviation from the log law. The curvature of the profile away from the expected log profile is behavior typically seen at higher elevations from the bottom where the log region ends and a wake region begins.
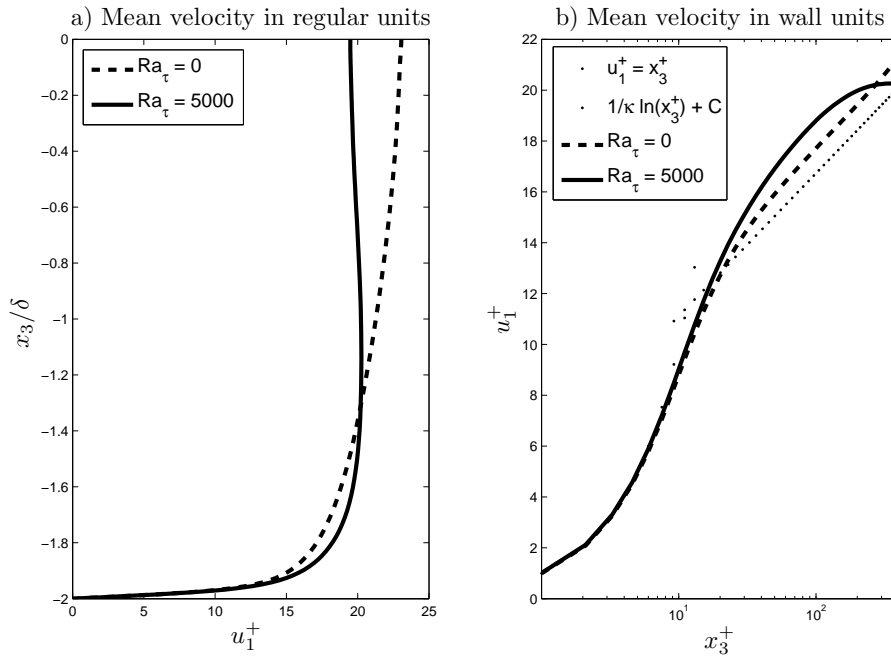

Figure 5.2: Mean velocity profiles: PG-driven case with cooling. a) Mean streamwise velocity profile as a function of depth and b) Mean streamwise velocity in wall units. In the theoretical log law, $\kappa = 0.41$ and $C = 5.5$. $x_3^+ = u_\tau z/\nu$ where z measures the height above the bottom wall. Also note that $x_3 = 0$ is the surface and $x_3/\delta = -2$ is the bottom wall

As observed in Chapter 4 (Figure 4.2), pressure gradient-driven open channel flow under certain forcing conditions has been found to be characterized by large turbulent structures acting as a secondary component to the mean flow. We may consider velocity fluctuations across various planes of the domain in order to visualize these structures. In the first of these visualizations, the streamwise velocity fluctuations on a horizontal plane at mid-depth in the water column are

54

compared for the cases $Ra_\tau = 0$ and $Ra_\tau = 5000$. It can be seen that in the former case (Figure 5.3b), the velocity fluctuations on the horizontal plane are characterized by streamwise, elongated streaks alternating in sign in the cross-stream direction. These streaks correspond to the Couette-like cell structures visualized in Chapter 4. When the cooling is applied (in the case with $Ra_\tau = 5000$) these cells merge, resulting in wider, more coherent streaks (Figure 5.3a).
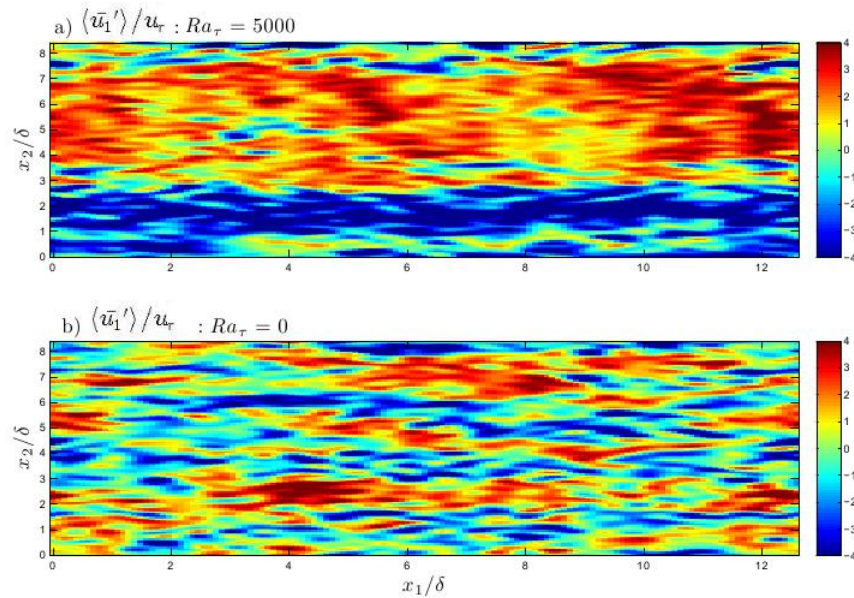

Figure 5.3: Horizontal plane colormaps of velocity fluctuations: PG-driven case with and without cooling. Plane is taken to be at mid-depth.

In order to further analyze the three dimensional structure associated with these elongated streamwise streaks it is possible to return to partially averaged instantaneous velocity fluctuations on a vertical ($x_2 - x_3$) plane averaged over the streamwise direction x_1 and time. Figures 5.4 and 5.5 show the a) cross-stream, b) vertical, and c) streamwise components of partially averaged velocity fluctuations for the $Ra_\tau = 0$ and $Ra_\tau = 5000$ cases respectively. Recall the observation in Chapter 4 of the weak closed cellular structure observed in the case without a surface cooling flux and with a constant pressure gradient or tidal force. Now notice that for the $Ra_\tau = 5000$

case, cross-stream velocity fluctuations are again characterized by surface intensification and a surface convergence zone: negative fluctuations meet positive fluctuations (Figure 5.5a) and lead into a coherent full-depth region of negative vertical velocity fluctuation (Figure 5.5b). Similarly, a bottom convergence zone in terms of cross-stream velocity fluctuations leads into a coherent full-depth region of positive vertical velocity fluctuation. The surface and bottom convergence zones in terms of cross-stream velocity fluctuation and the associated strongly positive and negative regions in the vertical velocity fluctuation indicate the presence of a full-depth convective supercell resolved in the LES. Observe that this cell structure is significantly stronger and more coherent than in the case with $Ra_\tau = 0$. The cross-stream width of the supercell is approximately 4 times its height. The vertical mixing induced by the up- and down- welling regions (or limbs) of the convective supercell (Figure 5.5b) in the case with $Ra_\tau = 5000$ is the cause of the homogenization in mean velocity visible in Figure 5.2 ultimately inducing a deviation from the log law observed earlier. As the fluctuations in the $Ra_\tau = 0$ case are not as strong nor coherent and resemble Couette cell structures similar to those found in [21] and [15], they are not sufficiently strong to generate an equivalent level of vertical mixing.

The organized low- and high-speed large-scale streaks at the horizontal mid-depth plane shown in Figure 5.3 correspond to the streamwise full-depth cells seen in Figures 5.4 and 5.5. All flows considered are characterized by a negative Reynolds shear stress $\langle \bar{u}_1' \bar{u}_3' \rangle$ throughout the entire water column, as will be seen later. By definition, this negative Reynolds shear stress implies a negative correlation between streamwise and vertical velocity fluctuations. Thus, full-depth downwelling limbs of the cells in Figures 5.4b and 5.5b coincide with full-depth regions of generally positive streamwise velocity fluctuation in Figures 5.4c and 5.5c. When viewed on a horizontal plane, the

56

latter correspond to the elongated streaks of positive streamwise velocity fluctuations observed in
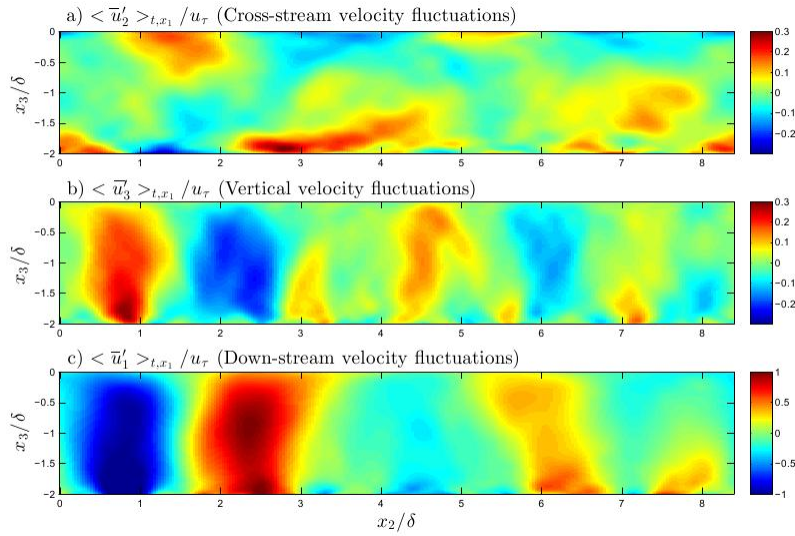
Figure 5.3.

Figure 5.4: Vertical plane colormaps of velocity fluctuations: PG-driven case without cooling. Fluctuations are partially averaged in time and the downstream (x_1) direction.
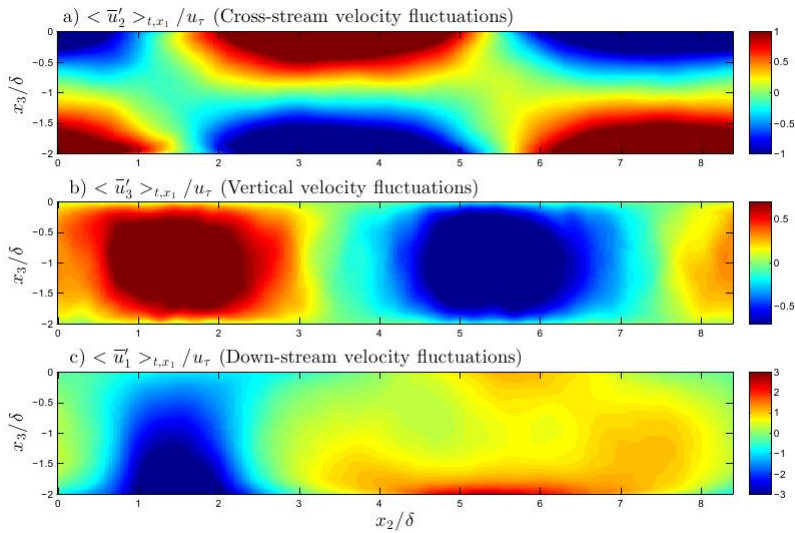

Figure 5.5: Vertical plane colormaps of velocity fluctuations: PG-driven case with cooling ($Ra_\tau = 5000$). Fluctuations are partially averaged in time and the downstream (x_1) direction.

The partially averaged fluctuations in Figures 5.4 and 5.5 have been averaged over 11 flow-throughs, leading to the organized cells seen in these figures. Although there may be some cross-

57

stream meandering and intermittent strengthening and weakening of the instantaneous streamwise-elongated cell structures, without a cross-wind mean flow (as is the case here) the cell movement in the x_2 direction will not be substantial enough to average out to 0 over time. The Couette cells obtained in [21] were found to be nearly stationary in the cross-stream direction leading to coherent structures after averaging in time and x_1, similar to the present computations.
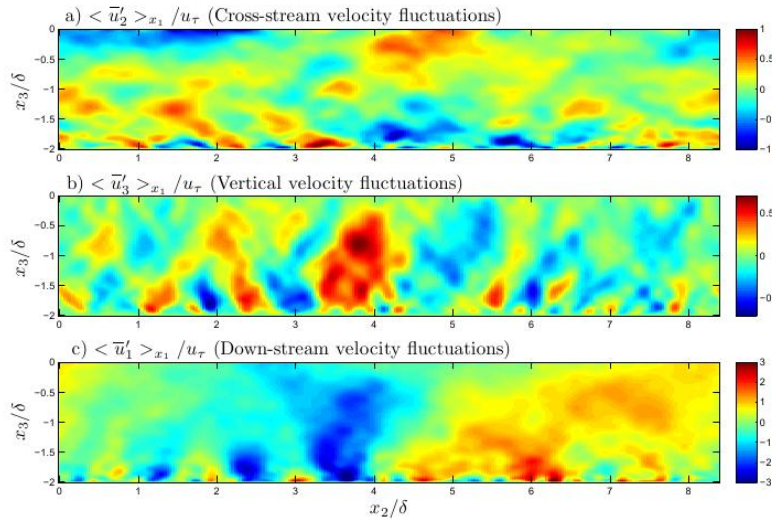

Figure 5.6: Vertical plane colormaps of instantaneous velocity fluctuations: PG-driven case with cooling ($Ra_\tau = 1000$).

The dependence of the convective supercells on the Rayleigh number can be supported by instantaneous snapshots of velocity fluctuations at intermediate Ra_τ values. Starting with $Ra_\tau = 0$ and gradually increasing the Rayleigh number allowed the observation of the transition from a pair of Couette-like cells to one convective cell. As exhibited in the color figures shown in Figures 5.6-5.8, the up and down-welling regions of the convective cell become significantly more coherent and visible as Ra_τ increases: note that the large scale structure is significantly more coherent at $Ra_\tau = 1500$ when compared with $Ra_\tau = 1200$. Based on these instantaneous snapshots of velocity fluctuations we infer the direct dependence of convective supercell development and strengthening

58

on Rayleigh number. Quantification of the strength of the convective supercells will be provided
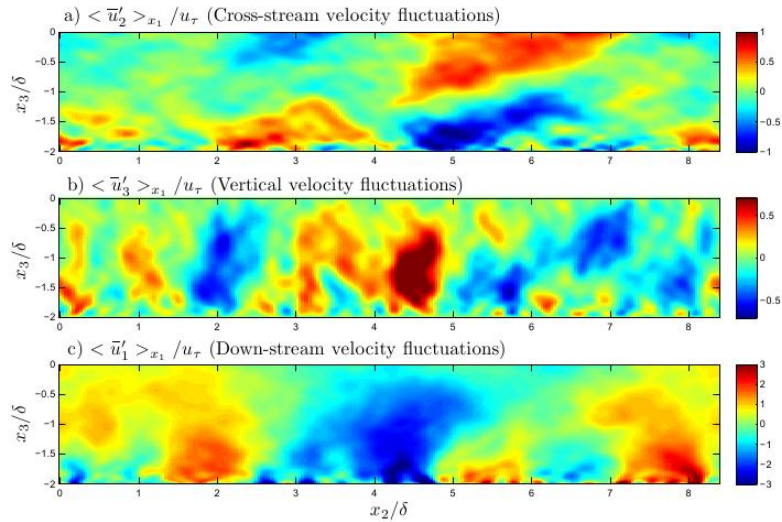
in the next section.

Figure 5.7: Vertical plane colormaps of instantaneous velocity fluctuations: PG-driven case with cooling ($Ra_\tau = 1200$).
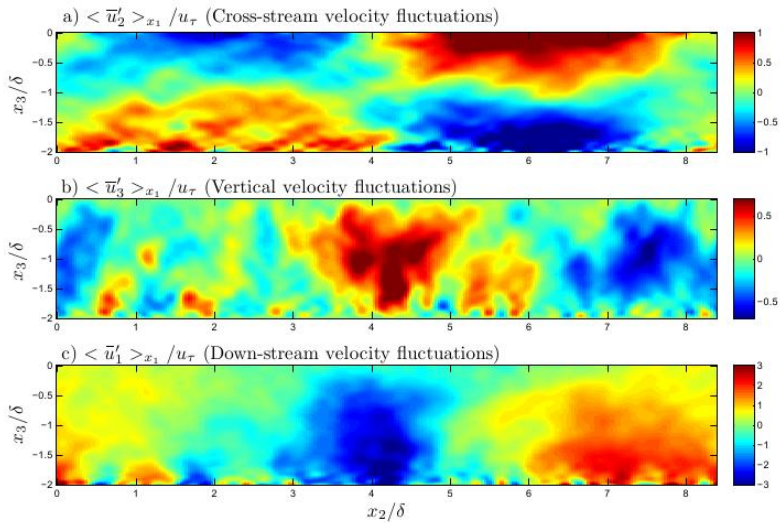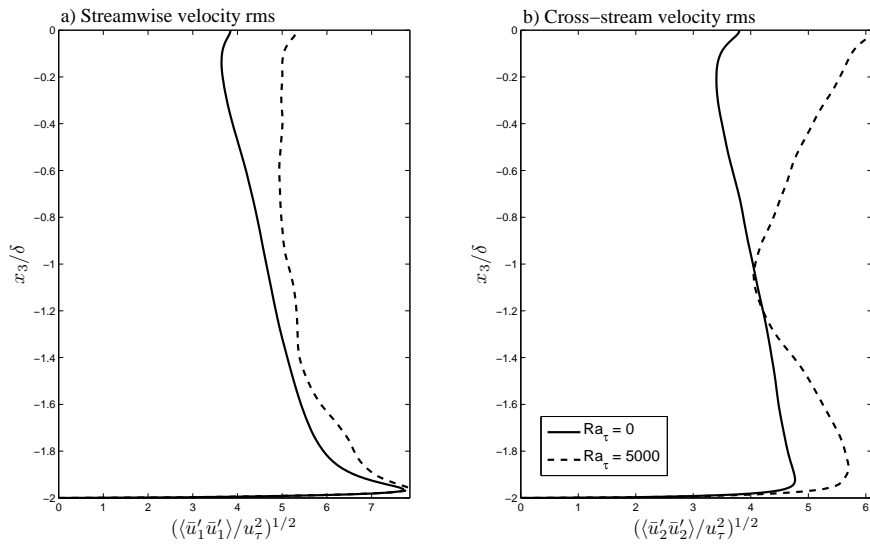

Figure 5.8: Vertical plane colormaps of instantaneous velocity fluctuations: PG-driven case with cooling ($Ra_\tau = 1500$).

As noted earlier, in order to distinguish between the mean flow and the turbulent fluctuations,

we employ a decomposition in which the LES velocity is decomposed as $\bar{u}_i = \langle \bar{u}_i \rangle + \bar{u}_i'$, where

59

brackets denote averaging over time and the downstream and cross-stream directions, and the prime indicates the velocity fluctuation component. To assess the impact of surface buoyancy, a comparison of the root mean square (RMS) of these velocity fluctuations for the case with $Ra_\tau = 5000$ and the case with $Ra_\tau = 0$ are presented, alongside the comparable figure for the fluctuating component of the temperature. The RMS of velocity and temperature fluctuations are computed as $u_1^{rms} = \langle \bar{u}_1'^2 \rangle^{1/2}$, $u_2^{rms} = \langle \bar{u}_2'^2 \rangle^{1/2}$, $u_3^{rms} = \langle \bar{u}_3'^2 \rangle^{1/2}$, and $\theta^{rms} = \langle \bar{\theta}'^2 \rangle^{1/2}$, respectively.

Figure 5.9: RMS of horizontal velocity fluctuations: PG-driven case with cooling

In the downstream RMS profile (Figure 5.9a), it can be seen that in the case with $Ra_\tau = 5000$ that there is an increase in RMS of velocity fluctuations from that in the case with $Ra_\tau = 0$. This increase is primarily induced by the full depth regions of intensified positive and negative streamwise velocity fluctuations characterizing the convective supercell, which are significantly stronger than those observed in the weaker cells characterizing $Ra_\tau = 0$. In Figure 5.9b we see that the flow with convection possesses greater cross-stream velocity fluctuations in the lower and upper halves of the water column, primarily attributed to the bottom divergence and surface convergence of the

60

convection cell resolved in the LES. In Figure 5.10a, the downwelling and upwelling limbs of the convection cell induce greater vertical velocity fluctuations. Finally, in Figure 5.10b it is possible to see diminishing of the temperature fluctuations due to homogenization throughout the bulk of the water column when $Ra_\tau = 5000$.
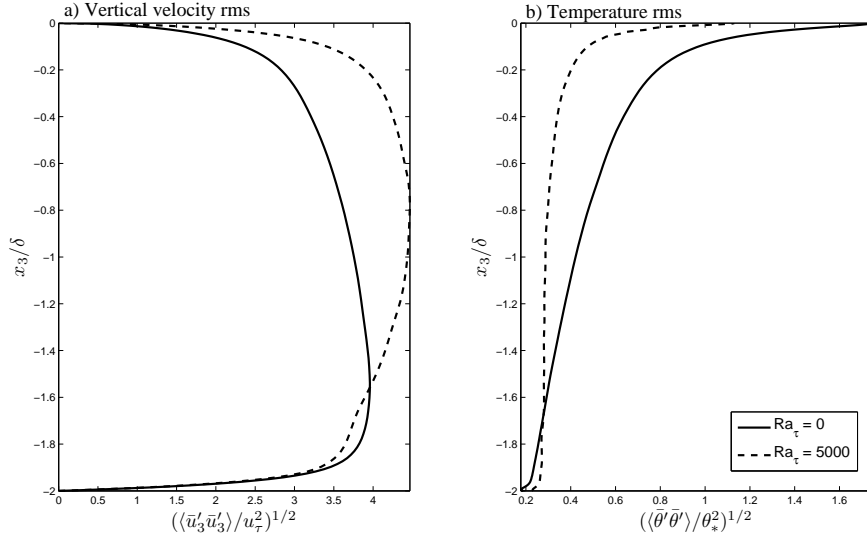

Figure 5.10: RMS of vertical velocity and temperature fluctuations: PG-driven case with cooling

Additionally, in order to quantify the strengthening of the cells with increasing Ra_τ visible in the colormaps presented in Figures 5.6-5.8, the following triple decomposition of an LES-resolved variable can be employed

$$\bar{\phi} = \langle\bar{\phi}\rangle_{x_1,x_2} + \bar{\phi}' \quad \text{with} \quad \bar{\phi}' = \langle\bar{\phi}\rangle_{x_1} + \bar{\phi}'' \tag{5.5}$$

where $\langle\cdot\rangle_{x_1,x_2}$ denotes averaging in the streamwise and cross-stream directions and $\langle\cdot\rangle_{x_1}$ denotes averaging in the streamwise direction only. Here, the resolved turbulent fluctuation has been decomposed into its largest scale $\langle\bar{\phi}'\rangle_{x_1}$ (corresponding to the large scale cellular structure previously analyzed in Figures 5.6-5.8) and smaller scales $\bar{\phi}''$.

61

By applying the above decomposition to the vertical velocity component to define $\bar{u}_3' = \langle \bar{u}_3' \rangle_{x_1} + \bar{u}_3''$ it is possible to assess the contribution of the full-depth cells to the turbulent vertical velocity fluctuations, indicating the relative strength of the up- and down-welling limbs. Applying the above decomposition, the instantaneous vertical velocity variance can be calculated as

$$\langle \bar{u_3}' \bar{u_3}' \rangle_{x_1,x_2} = \langle \langle \bar{u_3}' \rangle_{x_1} \langle \bar{u_3}' \rangle_{x_1} + \bar{u_3}'' \bar{u_3}'' + 2\bar{u_3}'' \langle \bar{u_3}' \rangle_{x_1} \rangle_{x_1,x_2} \tag{5.6}$$

where the contribution due to full-depth coherent cells (CC) is defined as

$$\langle \bar{u}_3' \bar{u}_3' \rangle_{CC} = \langle \langle \bar{u}_3' \rangle_{x_1} \langle \bar{u}_3' \rangle_{x_1} \rangle_{x_1,x_2} \tag{5.7}$$

Figure 5.11 shows the respective contributions to resolved instantaneous vertical velocity variance of the full-depth circulation present at increasing values of the Rayleigh number. Notice that as the Rayleigh number increases, corresponding to an increase in the surface buoyancy, the vertical velocity fluctuations associated with the large-scale convection cells are enhanced significantly.

The mean temperature and vertical turbulent heat flux are shown in Figure 5.12. In Figure 5.12a it can be seen that the increased mixing in the $Ra_\tau = 5000$ case leads to greater homogenization of the mean temperature throughout the water column and a correspondingly thinner surface thermal boundary layer with respect to the $Ra_\tau = 0$ case. The turbulent vertical heat flux in Figure 5.12b shows a linear profile throughout the bulk of the flow domain in both cases, yet again demonstrates a decrease in size of the thermal boundary layer corresponding to the increase in Rayleigh number. Vertical turbulent heat flux is greater in the $Ra_\tau = 5000$ case throughout the water column.
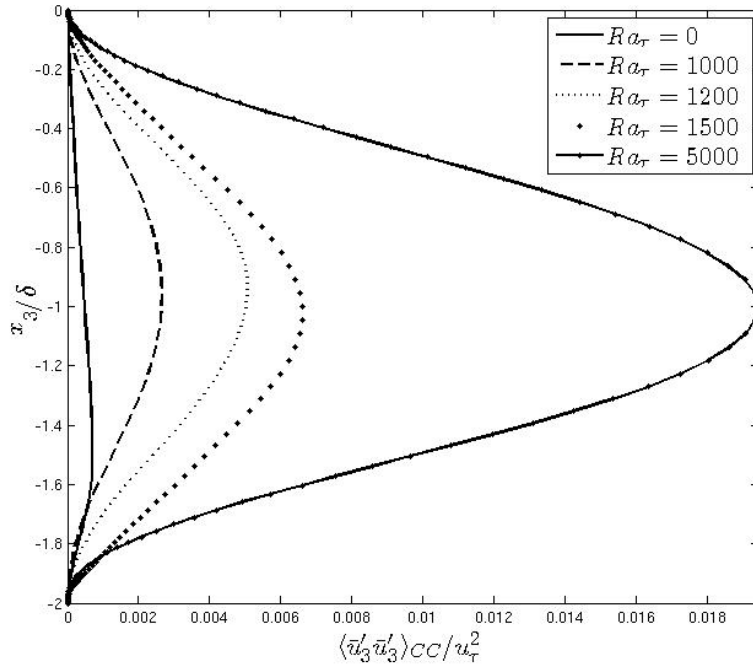
Figure 5.11: Instantaneous vertical velocity variance for varying values of Ra_τ: PG-driven case
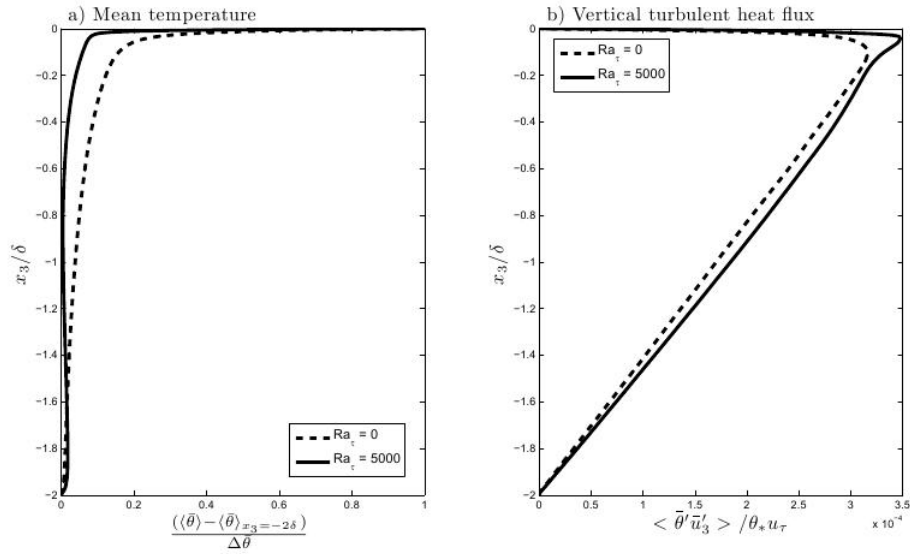

Figure 5.12: Temperature profiles: PG-driven case with cooling. a) Mean temperature and b) vertical turbulent heat flux throughout full water column depth. Note that $\Delta\bar{\theta} = \langle\bar{\theta}\rangle_{x_3=0} - \langle\bar{\theta}\rangle_{x_3=-2\delta}$.

63

Next we consider the sinks and sources of turbulent kinetic energy (TKE) and energy transfers between TKE components. Following the classical Reynolds decomposition, we consider the transport equation for resolved turbulent kinetic energy as follows

$$\frac{\partial \bar{q}}{\partial t} = A + D + \varepsilon + T^{SGS} + \varepsilon^{SGS} + P + T + B \tag{5.8}$$

where $\bar{q} = \langle \bar{u}'_i \bar{u}'_i \rangle / 2$ is the resolved TKE and

$$
\begin{aligned}
A &= -\frac{\partial \langle \bar{p}' \bar{u}'_3 \rangle}{\partial x_3} \\
D &= \frac{1}{Re_\tau} \frac{\partial^2 \bar{q}}{\partial x_3^2} \\
\varepsilon &= -\frac{1}{Re_\tau} \left\langle \frac{\partial \bar{u}'_i}{\partial x_j} \frac{\partial \bar{u}'_i}{\partial x_j} \right\rangle \\
T^{SGS} &= \frac{\partial \langle \tau'_{i3} \bar{u}'_i \rangle}{\partial x_3} \\
\varepsilon^{SGS} &= -\langle \tau'_{ij} \bar{S}'_{ij} \rangle \\
P &= -\langle \bar{u}'_1 \bar{u}'_3 \rangle \frac{\partial \langle \bar{u}_1 \rangle}{\partial x_3} \\
T &= -\frac{\partial \langle \bar{u}_j' \bar{q} \rangle}{\partial x_j} \\
B &= Ra_\tau \langle \theta_f \bar{u}'_3 \rangle
\end{aligned}
\tag{5.9}
$$

These terms in respective order represent the pressure transport rate (A), the viscous diffusion rate (D), the viscous dissipation rate (ε), the SGS transport rate (T^{SGS}), the SGS dissipation rate (ε^{SGS}), the mean shear production rate (P), the turbulent transport rate (T) and the buoyancy production rate (B).
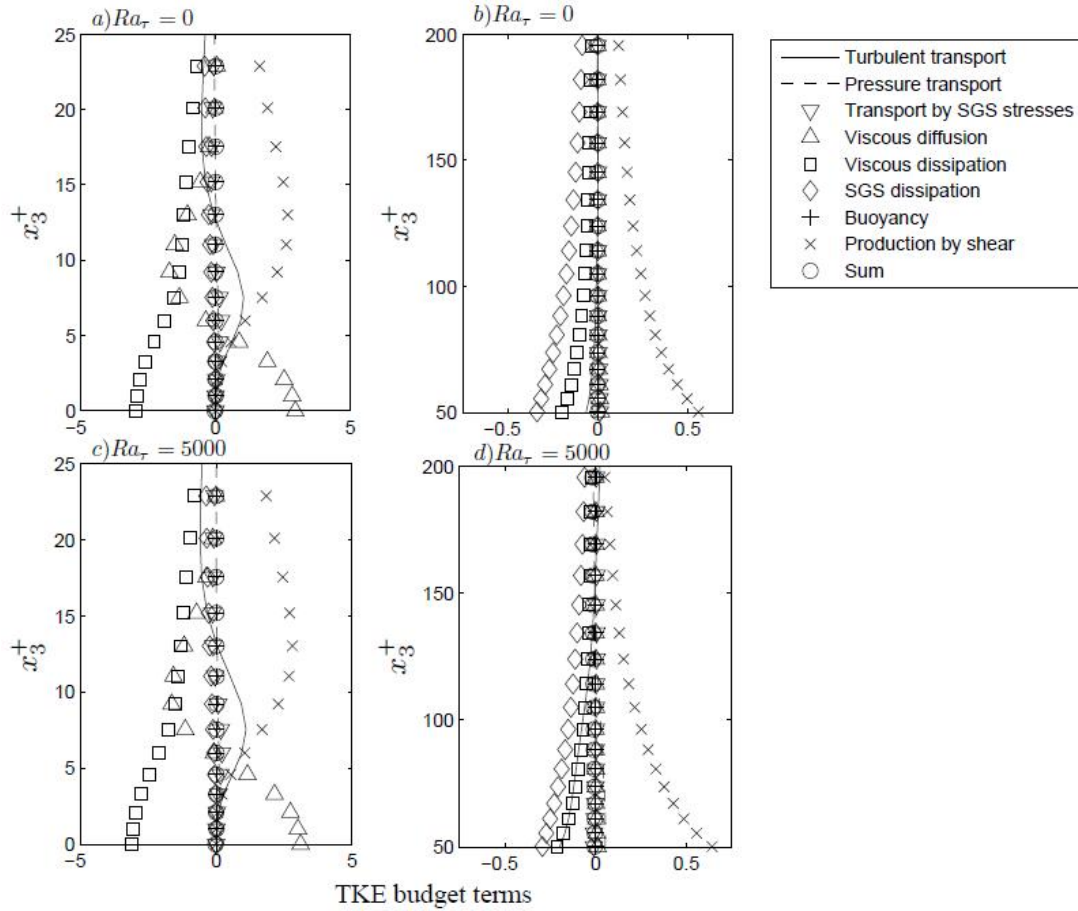
64

Figure 5.13: Budgets of turbulent kinetic energy in near-bottom region: PG-driven case with and without surface cooling. Ranges shown are within $0 \leq x_3^+ \leq 25$ from the bottom (left) and within $50 \leq x_3^+ \leq 200$ from the bottom (right). Budget terms are scaled by u_τ^2.

Profiles of these TKE budget terms are shown in Figures 5.13 and 5.14. Figure 5.13 presents

the sources and sinks of the TKE budget close to the bottom wall for the cases with $Ra_\tau = 0$ and

$Ra_\tau = 5000$. Shown are regions between $0 \leq x_3^+ \leq 200$ in order to allow further understanding of

the impact of cooling on bottom boundary layer dynamics. Note that the budget terms sum to zero

in both flows ($Ra_\tau = 0, 5000$) as the flows are in statistical equilibrium.

It is possible to see that close to the wall, the behavior of the budget terms is almost identical for

the cases with $Ra_\tau = 0$, $Ra_\tau = 5000$ cases. The main difference is that turbulent transport provides

a significant sink in the region $x_3^+ < 75$ shown for the $Ra_\tau = 5000$ case.
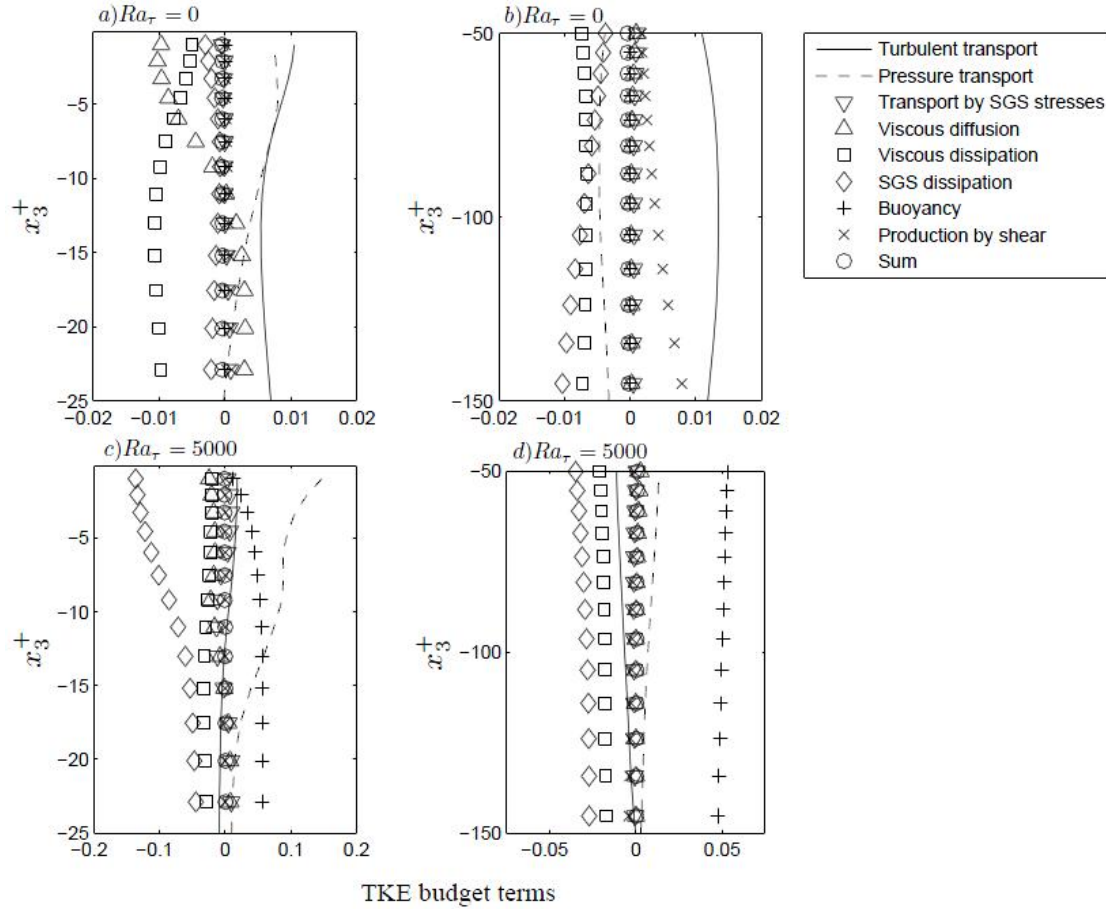
65

Figure 5.14: Budgets of turbulent kinetic energy in near-surface region: PG-driven case with and without surface cooling. Ranges shown are within $0 \leq x_3^+ \leq 25$ from the surface (left) and within $50 \leq x_3^+ \leq 200$ from the surface (right). Budget terms are scaled by u_τ^2.

It is seen that the turbulent transport within this log layer region disrupts the classical balance between production by mean shear and dissipation (viscous and SGS). However, looking at comparable figures for the near surface region over domain sections from $0 \leq x_3^+ \leq 200$ from the upper surface (see Figure 5.14), there is a noticeable difference in the cases with and without convection. The latter (Figure 5.14a) features a balance between a combination of large positive turbulent transport components, and large negative viscous diffusion, viscous dissipation and SGS dissipation components. When convection is applied, viscosity components decrease significantly in their relative contribution, SGS dissipation taking over as the main sink and being balanced by the now

66

present and significant buoyancy energy source and an increased pressure transport term (Figure 5.14c). Considering the region $50 \leq x_3^+ \leq 150$ from the upper surface (Figures 5.14b,d), the impact of buoyancy is again clear, with this becoming the largest source of TKE by a significant margin.

The transport equations for the TKE components and the Reynolds shear stress $- < \bar{u}_1' \bar{u}_3' >$ may be obtained from

$$\frac{\partial \langle \bar{u}_i' \bar{u}_j' \rangle}{\partial t} = A + D + \varepsilon + T^{SGS} + \varepsilon^{SGS} + PSR + P + T + B \tag{5.10}$$

where

$$A = -\frac{\partial}{\partial x_3}[\delta_{j3}\langle \bar{\pi}' \bar{u}_i' \rangle + \delta_{i3}\langle \bar{\pi}' \bar{u}_j' \rangle]$$

$$D = \frac{1}{Re_\tau}\frac{\partial^2 \langle \bar{u}_i' \bar{u}_j' \rangle}{\partial x_3^2}$$

$$\varepsilon = -\frac{2}{Re_\tau}\left\langle \frac{\partial \bar{u}_i'}{\partial x_k}\frac{\partial \bar{u}_j'}{\partial x_k} \right\rangle$$

$$T^{SGS} = \frac{\partial}{\partial x_3}[\langle \tau_{j3}' \bar{u}_i' \rangle + \langle \tau_{i3}' \bar{u}_j' \rangle]$$

$$\varepsilon^{SGS} = -\langle \tau_{ik}' \frac{\partial \bar{u}_j'}{\partial x_k} \rangle - \langle \tau_{jk}' \frac{\partial \bar{u}_i'}{\partial x_k} \rangle \tag{5.11}$$

$$PSR = 2\langle \bar{\pi}' \bar{S}_{ij}' \rangle$$

$$P = -\langle \bar{u}_i' \bar{u}_3' \rangle \frac{\partial \langle \bar{u}_j \rangle}{\partial x_3} - \langle \bar{u}_j' \bar{u}_3' \rangle \frac{\partial \langle \bar{u}_i \rangle}{\partial x_3}$$

$$T = -\frac{\partial \langle \bar{u}_i' \bar{u}_j' \bar{u}_3' \rangle}{\partial x_3}$$

$$B = Ra_\tau[\delta_{i3}\langle \theta_f \bar{u}_j' \rangle + \delta_{j3}\langle \theta_f \bar{u}_i' \rangle]$$

67

These terms represent the pressure transport rate (A), the viscous diffusion rate (D), the viscous dissipation rate (ε), the SGS transport rate (T^{SGS}), the SGS dissipation rate (ε^{SGS}), the pressure-strain redistribution (PSR), the mean shear production rate (P), the turbulent transport rate (T) and the buoyancy term (B).

To limit the scope of presentation, we include only the budgets of resolved Reynolds shear stress $-\langle \bar{u}'_1 \bar{u}'_3 \rangle$ (obtained by substituting $i = 1$ and $j = 3$ into the above equation), and the reader is directed to Walker et al. (2014) [34] for an extended discussion on the budgets of the individual TKE components as well as the budgets of vertical turbulent heat flux $- < \bar{u}'_3 \bar{\theta} >$.

Considering the $-\langle \bar{u}'_1 \bar{u}'_3 \rangle$ budgets in the viscous wall region (see Figures 5.15a,c), pressure strain redistribution is the main sink in the cases with $Ra_\tau = 0$ and $Ra_\tau = 5000$, while pressure transport and mean shear are the principal sources. More drastic differences between these cases are observed in the log-layer region (Figures 5.15b,d) where in the $Ra_\tau = 0$ case, production by mean shear is primarily balanced by pressure strain redistristribution, whereas in the $Ra_\tau = 5000$ case, production by mean shear is primarily balanced by pressure transport. Note here that the cooling-induced buoyancy acts as a relatively small source compared with mean shear production.

Reynolds shear stress budgets near the surface are dramatically different in the two cases considered (Figures 5.16b,d). In the $Ra_\tau = 5000$ case, the main source is production by buoyancy as mean shear acts as a sink (in contrast with mean shear production in the $Ra_\tau = 0$ case). In the region $50 < x_3^+ < 150$ from the surface for the case with $Ra_\tau = 5000$ (Figure 5.16d), production by mean velocity shear becomes negative implying that vertical transport is non-local, attributed to the upwelling and downwelling limbs of the convective supercell. Thus, a model of $-\langle \bar{u}'_1 \bar{u}'_3 \rangle$ should consider non-local transport in addition to the usual eddy viscosity-based local term.
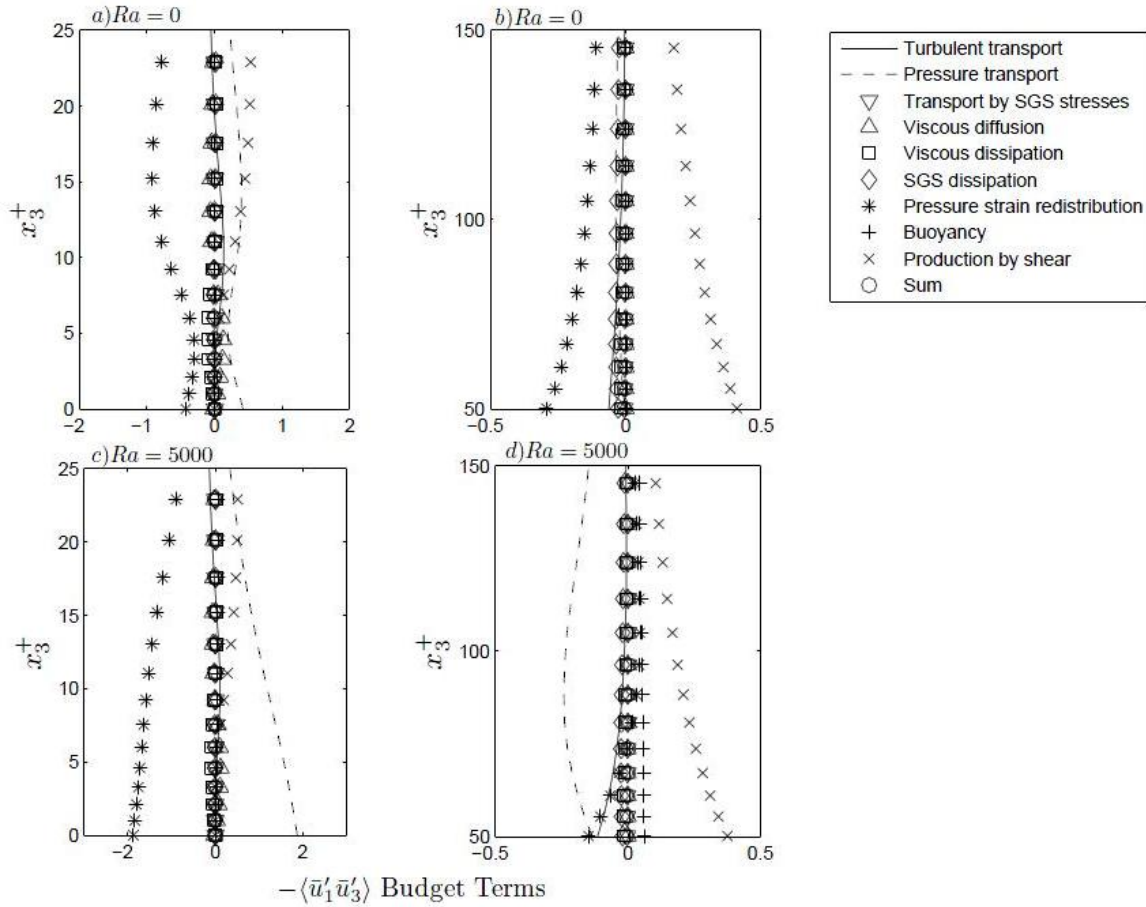
68

Figure 5.15: Budgets of Reynolds shear stress in near-wall region: PG-driven case with and without surface cooling. Ranges shown are within $0 \le x_3^+ \le 25$ from the surface (left) and within $50 \le x_3^+ \le 200$ from the surface (right). Budget terms are scaled by u_τ^2.

We have analyzed diagnostics of flows with Rayleigh numbers of 0 (no cooling-induced buoyancy) and 5000 (cooling-induced buoyancy) in LES of a constant pressure gradient (tidal force) driven open channel flow with a no-slip bottom wall which can be considered a simple representation of a tidally driven shallow ocean region. The turbulent structures have been analyzed by means of plane color figures of velocity fluctuations, mean velocity profiles both in the bulk flow and in the bottom boundary layer, RMS of velocity and temperature fluctuations, and budgets of TKE, Reynolds shear stress and vertical turbulent heat flux.
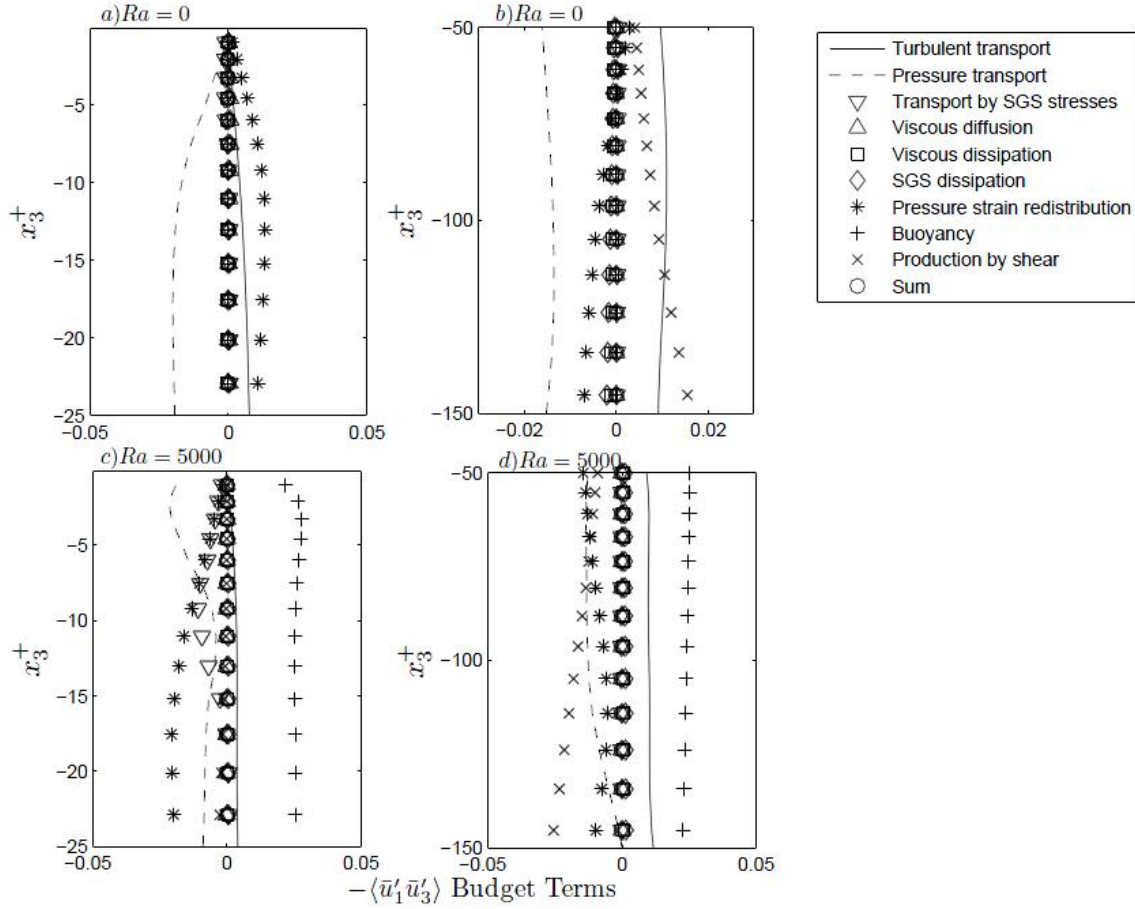
69

Figure 5.16: Budgets of Reynolds shear stress in near-surface region: PG-driven case with and without surface cooling. Shows $-\langle \bar{u}_1' \bar{u}_3' \rangle$ in near-surface region within the range $0 \leq x_3^+ \leq 25$ from the surface (left) and within $50 \leq x_3^+ \leq 200$ from the surface (right). Budget terms are scaled by u_τ^2.

It was found that buoyancy generated by surface cooling generates large convective supercells secondary to the mean flow in the form of pairs of parallel counter-rotating streamwise-elongated vortices in which the cross-stream width of one cell pair is approximately four times its height. The case with $Ra_\tau = 0$ is characterized by Couette-like cells similar to those found under maximim tidal forcing conditions in the oscillating pressure gradient-driven open channel flow of [15]. Buoyancy induced by surface cooling leads to merging and strengthening of these cells, ultimately giving rise to a full-depth convective supercell. This large convective structure resolved in the LES disrupts

classical boundary layer dynamics such as the typical log-law velocity profile of a turbulent flow over a no-slip wall and the balance between production of TKE by mean shear and molecular and SGS dissipation.

These results identified large convective cells under surface cooling buoyancy forcing conditions for the first time and have important implications for parameterizations of the Reynolds shear stress in coarse grid models that do not resolve the turbulence, and for further computational study on the factors which both cause and influence full-depth vertical mixing, in shallow shelf regions. The latter observation motivates the following tests involving the application of surface cooling to our other fundamental flow problems driven by wind alone, and by wind and Langmuir forcing.

5.2 Wind-Driven

As the intermediate step in the testing of the impact of surface cooling on our range of flows, the case driven by a surface wind stress only and in the absence of a tidal pressure gradient was simulated at two cooling strengths: $Ra_\tau = 5000$ and $Ra_\tau = 211$. The Rayleigh number of 211 was calculated based on field measurements of LC in a coastal region by Gargett et al. (2004) where the observed wind stress was approximately $0.1\,\mathrm{N/m^2}$ and represents a surface cooling flux of approximately $200\,\mathrm{W/m^2}$. As heat fluxes of this magnitude are observed frequently in coastal environments, we refer to this as a *moderate* surface cooling flux. A Rayleigh number of 5000 represents our *strong* cooling flux. From here it is intended to gain some insight into not only if the same effects are visible in this different flow setup, but also how significant the magnitude of the cooling flux is in determining the intensity of cooling effects on large-scale flow structures.

71

For both the wind-driven flow, and the wind and Langmuir-forced flow to be discussed in Chapter 6, the flow domain is shown below in Figure 5.17. The flow is driven by a wind stress such that $Re_\tau = 395$ based on the wind friction velocity. Note that in this configuration in the mean the bottom friction velocity is equal to u_τ.
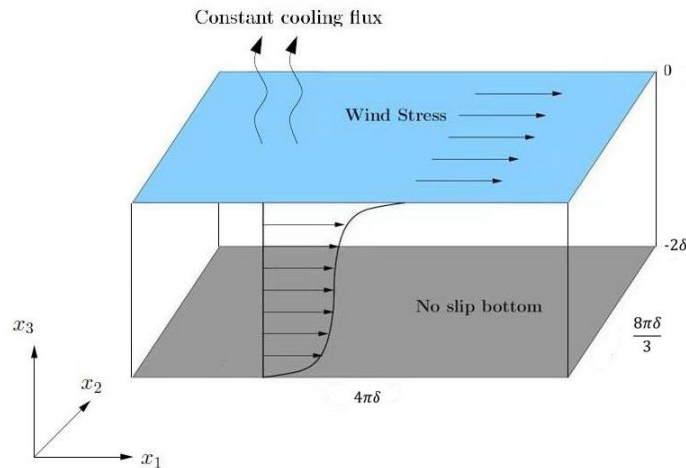

Figure 5.17: Problem domain: Wind-driven flow with cooling

As before, we may consider the flow velocity profiles, both in the full-depth channel and in the bottom boundary region, for our three flows of interest. Initially we consider the mean stream-wise velocity profile in standard units for the whole channel, seen on the left. As the Rayleigh number increases from the flow with zero surface cooling described in Chapter 4, we can see the increasing level of mixing leading to a homogeneous velocity profile throughout the bulk of the water column, as was visible in the tidally-driven case. In Figure 5.18 we can see that in these cases with wind only, applying a surface cooling flux represented by $Ra_\tau = 211$ is sufficient to lead to a substantial difference in terms of mean velocity; the log layer profile demonstrates significant disruption when compared to the expected profile which the case without surface cooling applied satisfies with reasonable accuracy (Figure 5.18b). As the Rayleigh number increases the extent of the homogenization caused by the surface cooling increases, reaching closer to the surface.
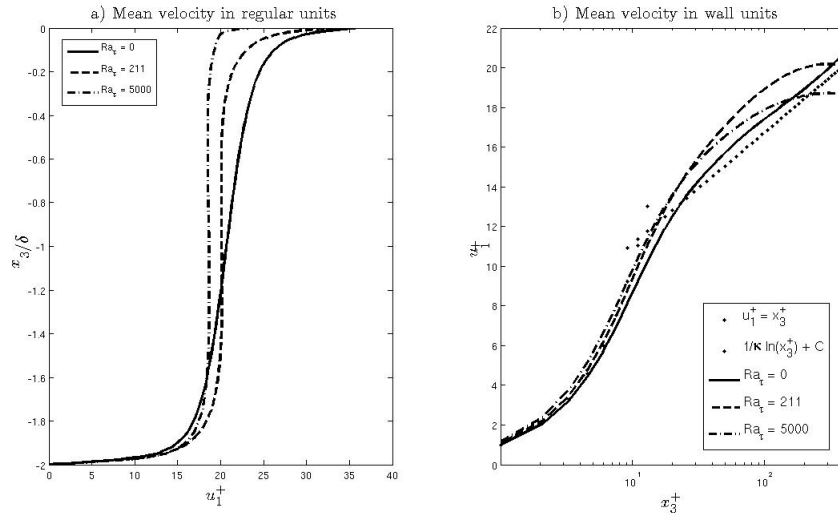
72

Figure 5.18: Mean velocity profiles: Wind-driven case with and without surface cooling. a) Mean streamwise velocity profile as a function of depth and b) Mean streamwise velocity in wall units in the lower half of the water column.

We can additionally consider the mean temperature profile throughout the water column, and also the vertical turbulent heat flux in the same region for each value of the Rayleigh number. On the left, considering the mean streamwise temperature profile, again an increased level of homogenization as the Rayleigh number increases is visible. With no surface cooling when the flow is under the influence of the surface wind forcing only, there is a positive temperature gradient throughout the water column. As Ra_τ increases, the surface thermal boundary layer also becomes noticably thinner.

Recall the cell structures comparable to Couette cells visible on horizontal plane colormaps in the case with wind stress only and zero surface cooling described in Chapter 4. As in the tidally-driven case, we can see the merging and strengthening of these cell structures as the cooling flux increases. The figures below demonstrate this strengthening and merging of cell structures, again visible in terms of the size and intensity of the up- and down-welling regions and surface and bottom convergence and divergence as the cooling flux increases.
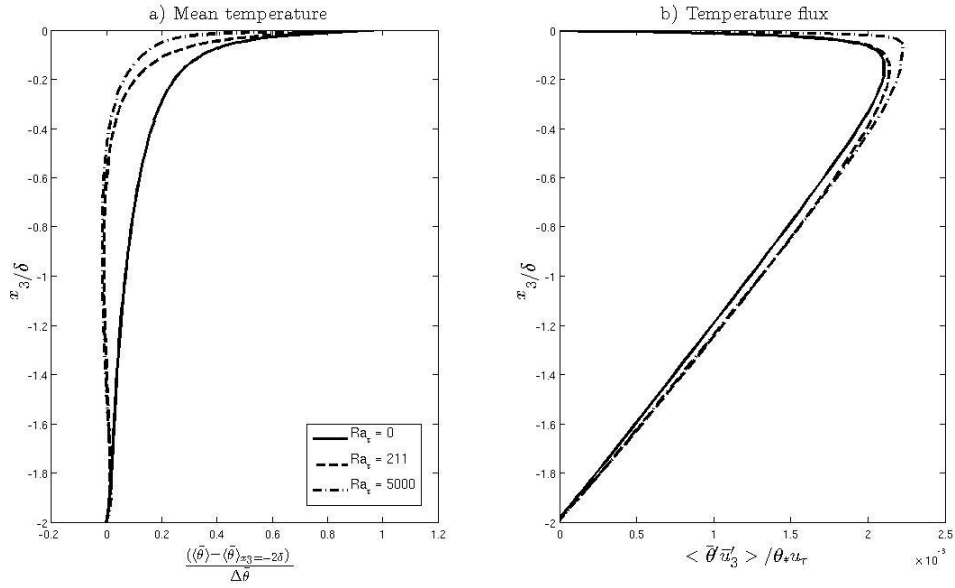
73

Figure 5.19: Temperature profiles: Wind-driven case with cooling. a) Mean temperature and b) vertical turbulent heat flux throughout full water column depth. Note that $\Delta\bar{\theta} = \langle\bar{\theta}\rangle_{x_3=0} - \langle\bar{\theta}\rangle_{x_3=-2\delta}$.
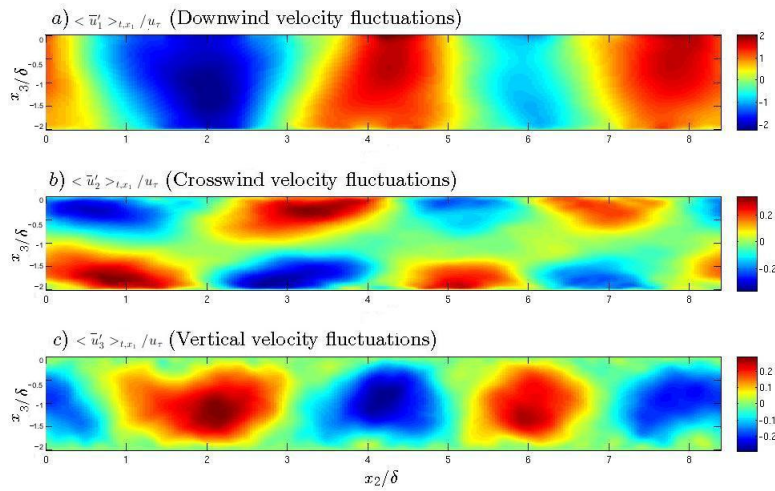

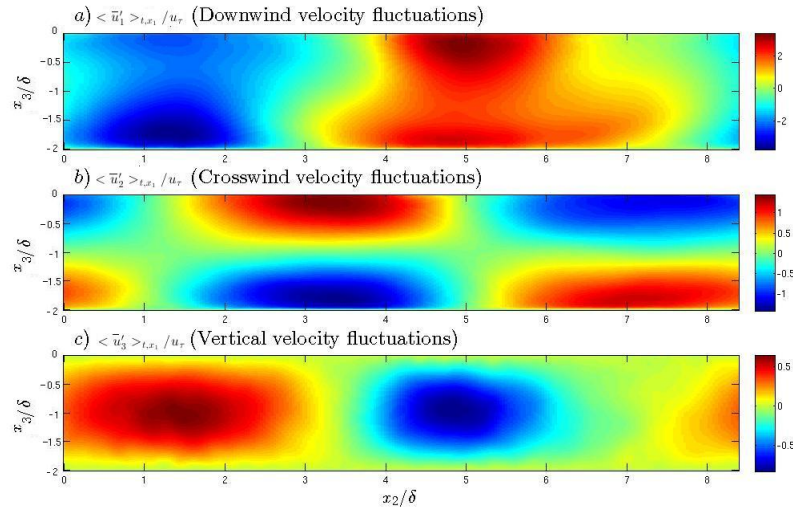Figure 5.20: Vertical plane colormaps of instantaneous velocity fluctuations: Wind-driven case without cooling

Figure 5.21: Vertical plane colormaps of instantaneous velocity fluctuations: Wind-driven case with cooling ($Ra_\tau = 211$)
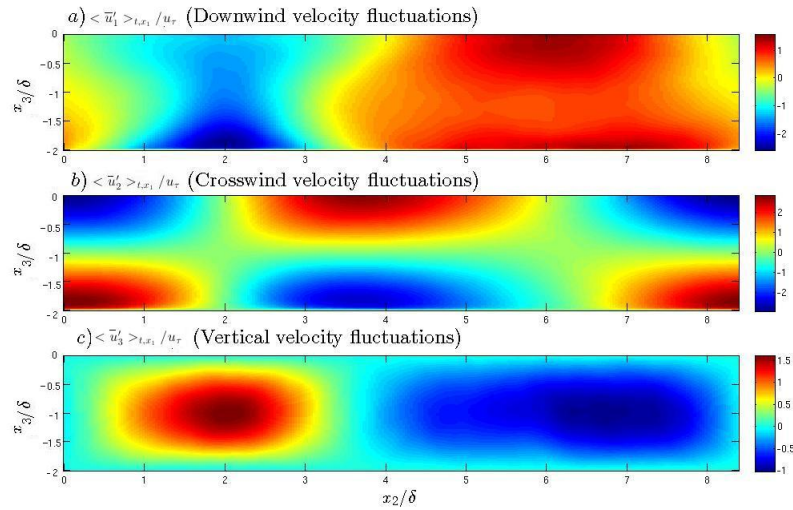

Figure 5.22: Vertical plane colormaps of instantaneous velocity fluctuations: Wind-driven case with cooling ($Ra_\tau = 5000$)

Recall in Section 5.1 the root mean square of velocity fluctuations were analyzed for the case driven by a constant tidal pressure gradient. Here it was observed that the application of strong surface cooling leads to intensification of RMS profiles, with the intensification associated with the convective supercell generated by surface cooling. In a similar fashion to the earlier tests,

75

in the wind-driven case the crosswind RMS profile in Figure 5.23b reflects the development of stronger surface and bottom convergence and divergence zones in the upper and lower halves of the water column as the Rayleigh number increases, suggesting the strengthening of the convective cell structure. Similarly in the vertical RMS in Figure 5.23c when $Ra_\tau = 5000$ is applied the level of turbulence arising from the regions of up and downwelling increases significantly relative to the lower Ra_τ cases.
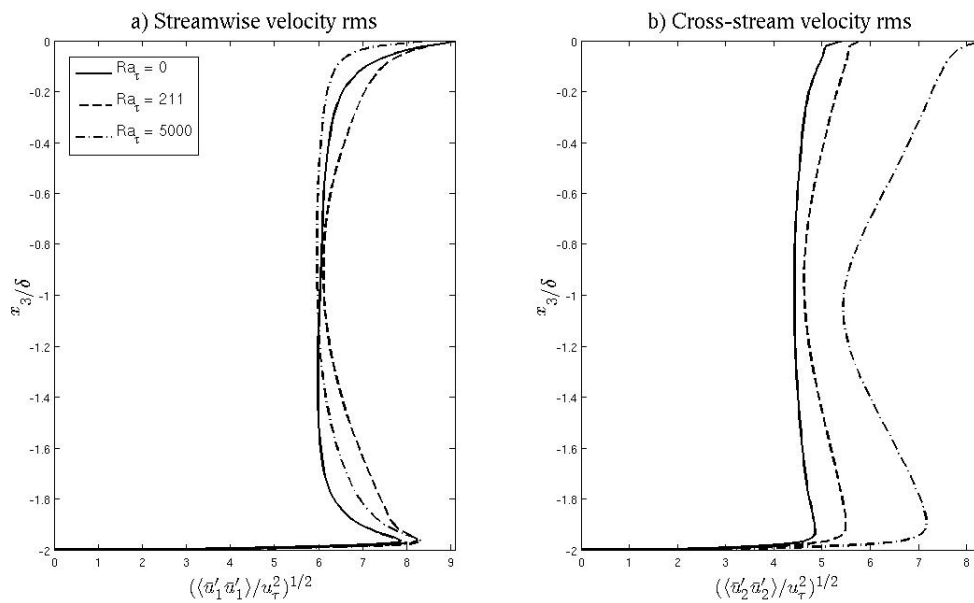

Figure 5.23: RMS of horizontal velocity fluctuations: Wind-driven case with cooling. Similar trends are observed as in the tidally-driven (pressure gradient-driven) case analyzed earlier.

As in the previous studies of pressure gradient-driven flow, the increase in coherent cell strength is significant for both $Ra_\tau = 211$ and $Ra_\tau = 5000$ (Figure 5.25).
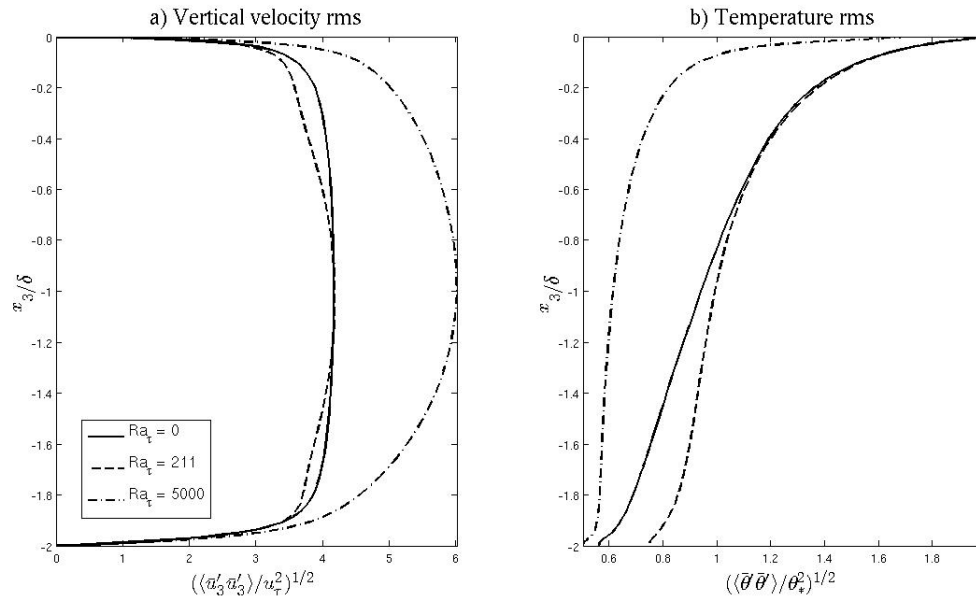
www.manaraa.com

Figure 5.24: RMS of vertical velocity and temperature fluctuations: Wind-driven case with cooling. Similar trends are observed as in the tidally-driven (pressure gradient-driven) case analyzed earlier.
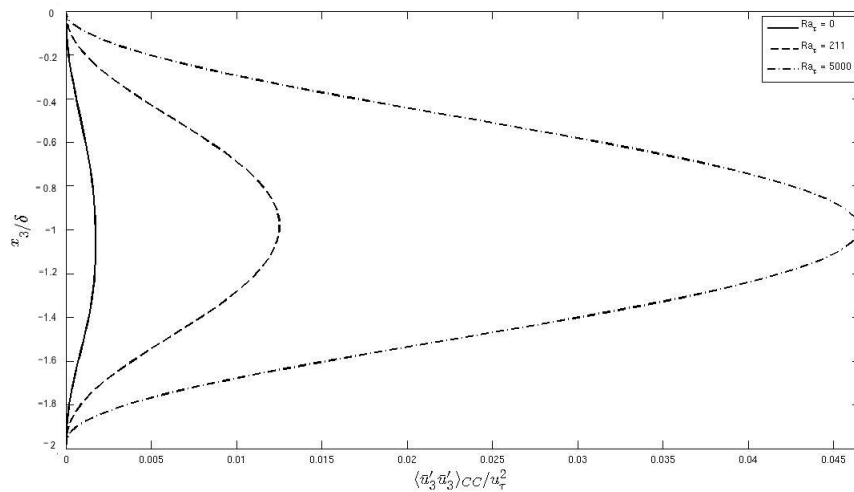

Figure 5.25: Instantaneous vertical velocity variance for varying values of Ra_τ: Wind-driven case

To summarize, the observations of cell strengthening in wind-driven flows are comparable to those found in the constant tidally-driven case. Without surface cooling, full-depth Couette-like cell structures are visible in vertical plane colormaps that are not strong enough to induce full-

77

www.manaraa.com

depth flow homogenization. When surface cooling is applied, these cells are able to strengthen and merge into one large convection supercell structure, so named due to their ability to reach full depth in a shallow water column and cause homogenization of flow properties (i.e. strong vertical mixing).

5.3 Convection Supercells

Recall that in the case with a surface wind stress only and no additional forcing mechanisms, Couette-like coherent cells are visible in terms of partially averaged velocity fluctuations. In the case driven by wind and Langmuir forcing and again without the application of a surface cooling flux (described in Chapter 4), it can be seen that these weak Couette cells present in the wind-driven case strengthen and merge to form one large, coherent full-depth cell. This represents one Langmuir "supercell" as observed both in a shallow coastal domain in the field in[8], [30].

The convection supercells visible in the present chapter for wind-driven flow with surface cooling, although caused by a different mechanism, share many structural similarities with the large scale Langmuir supercells presented in Chapter 4. Both Langmuir supercells and convection supercells are characterized by large counter rotating cell pairs, elongated in the downstream direction, secondary to the mean flow and reaching full depth in a shallow domain. For clarity, below in Figures 26-28 is a direct comparison of vertical plane colormaps of velocity fluctuations for three flows: a wind-driven flow in the absence of both surface cooling and Langmuir forcing, a wind-driven flow with surface cooling only, and a wind-driven flow with Langmuir forcing only (no surface cooling). All flows are at $Re_\tau = 395$. Initially, note the scale of the colorbar for the wind-only case (Figure 5.26); these velocity fluctuations are significantly weaker than those observed

78

in both convection-driven (Figure 5.28) and Langmuir-driven (Figure 5.27) cell structures. It can be seen that under both forcing mechanisms, the weak Couette cells visible in the case with wind alone both strengthen and merge to form one large, coherent cell pair. Although not identical, the resulting cells are similar in size and magnitude.

We may conduct further comparison of the key characteristics of these two types of super-cell (Langmuir-driven and buoyancy-driven) by considering other statistical properties of the three flows. From this, we are able to more clearly demonstrate the shared features of large cells initiated by each respective mechanism.
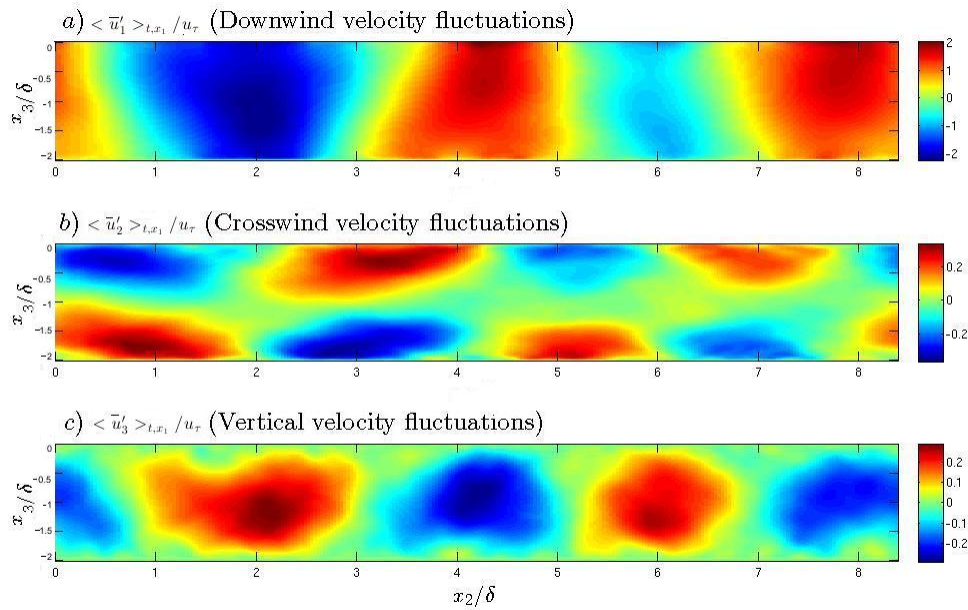

Figure 5.26: Vertical plane colormaps of velocity fluctuations: Wind only. Fluctuations are partially averaged in time and the streamwise (x_1) direction.

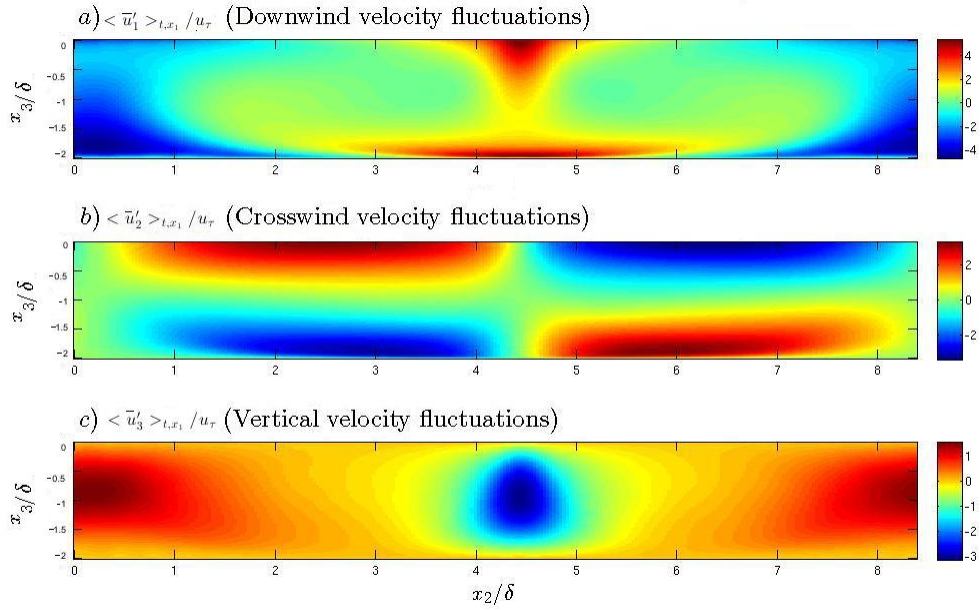Figure 5.27: Vertical plane colormaps of velocity fluctuations: Wind and LC. Fluctuations are partially averaged in time and the streamwise (x_1) direction.
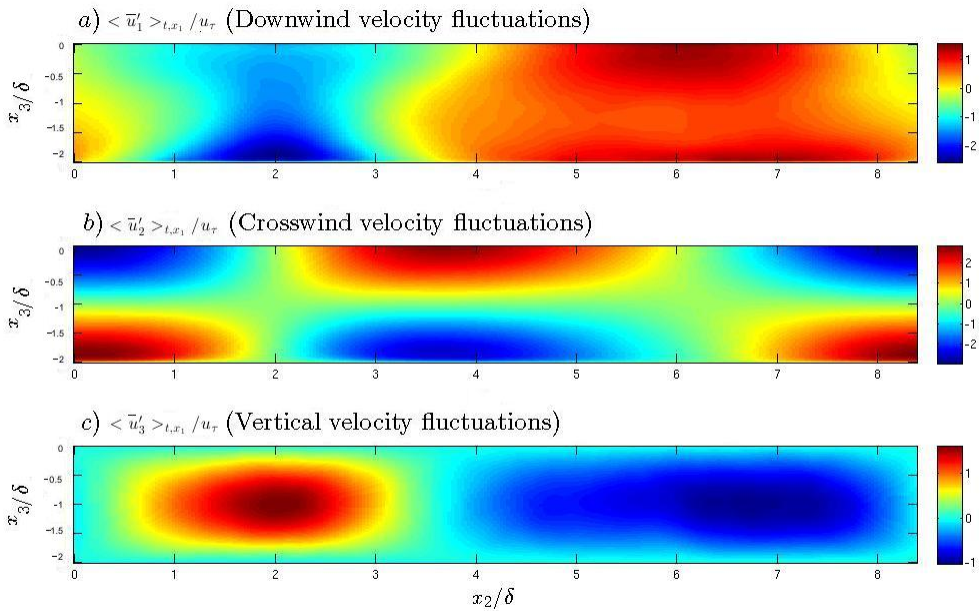

Figure 5.28: Vertical plane colormaps of velocity fluctuations: Wind and cooling ($Ra_\tau = 5000$). Fluctuations are partially averaged in time and the streamwise (x_1) direction.

80

To further assess the similarity of the two forms of supercell identified in the vertical plane colormaps, we can again consider the mean stream-wise velocity profiles as a function of depth in standard units for the full depth of the water column and the bottom boundary layer (with emphasis on the bottom viscous sub-layer ($x_3^+ \leq 5$), the buffer layer ($5 \leq x_3^+ \leq 30$) and the log layer ($30 \leq x_3^+ \leq 100$)).
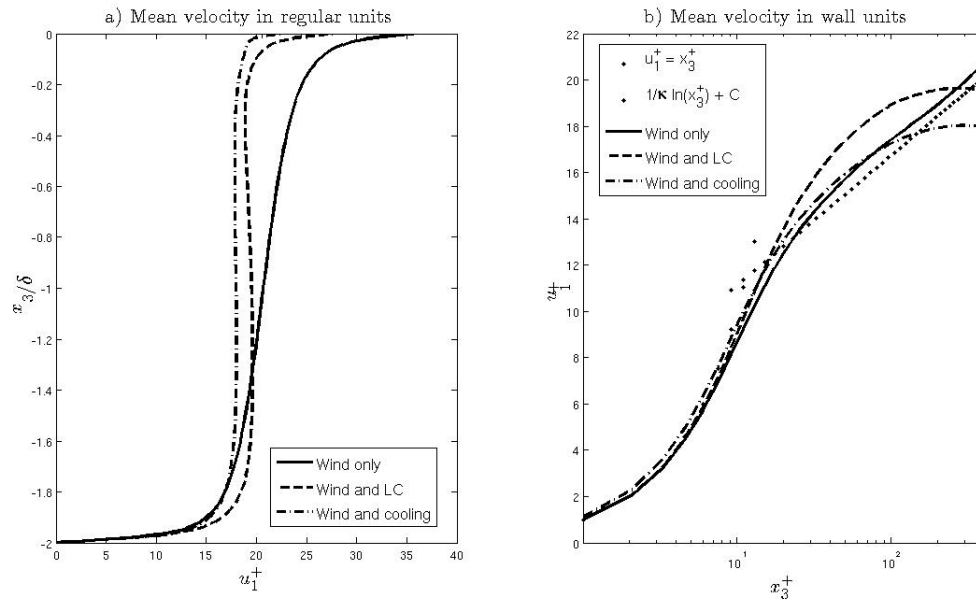

Figure 5.29: Mean velocity profiles: Supercell comparison. a) Mean streamwise velocity profile as a function of depth and b) Mean streamwise velocity in wall units at lower wall

Figure 5.29a shows the mean velocity profiles in the full depth of the water column for our three flows, and we can primarily see that in the case without either LC or cooling present, the velocity demonstrates an S-shaped profile featuring a positive gradient throughout the water column, as is to be expected in a simple wind-driven flow. This profile is altered in both cases with an additional mechanism applied. In both the case with LC and the case with surface cooling, the increased vertical mixing induced by the presence of a full-depth supercell leads to greater homogenization throughout the full depth of the water column and a significant narrowing of the surface boundary

81

layer. In Figure 5.29b, where the wind-driven flow is approximately characterized by an expected log law profile (indicated in the figure by the dotted line) which represents the behavior of a typical boundary layer flow, in both the case with LC and surface cooling this log law profile is strongly disrupted by the presence of a supercell.

Additionally, we can again consider the RMS of velocity fluctuations, computed as $u_1^{rms} = \langle \bar{u}_1'^2 \rangle^{1/2}$, $u_2^{rms} = \langle \bar{u}_2'^2 \rangle^{1/2}$ and $u_3^{rms} = \langle \bar{u}_3'^2 \rangle^{1/2}$ respectively, where as previously brackets represent Reynolds averaging.
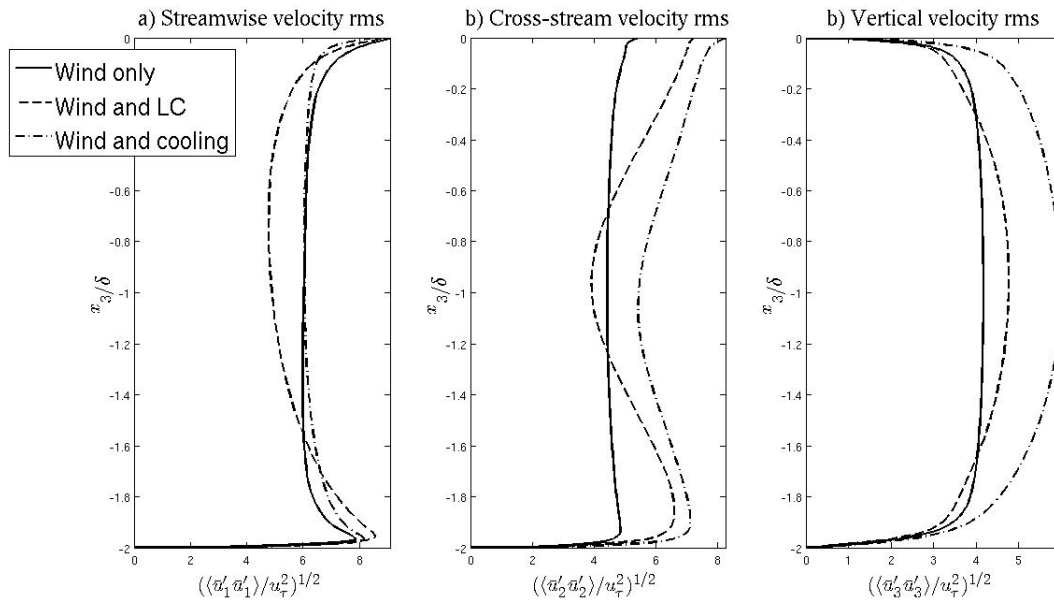

Figure 5.30: RMS of velocity fluctuations: Supercell comparison. Wind and LC refers to flow with Langmuir supercells.

In Figure 5.30 it can be seen that for the case with wind only, the velocity RMS is approximately homogeneous in the bulk of the water column. In contrast, in the cases featuring Langmuir-driven supercells and convection-driven supercells, the regions of surface and bottom convergence and divergence of the cells are identifiable by the higher magnitudes of crosswind velocity RMS at the near surface and near bottom of the water column when compared to the mid-depth, visible in the

82

center panel in Figure 5.30. In the panel on the right, observe that the vertical velocity RMS are at a maximum in the middle of the water column, representative of the full-depth up- and down-welling limbs of the Langmuir and convective supercells relative to the Couette-like cells in the flow with wind stress only.

We can also consider budgets of TKE for these three cases with surface wind stress only and with Langmuir forcing and surface cooling respectively acting in isolation. The transport equation for resolved turbulent kinetic energy now featuring a Stokes-drift shear production term representing the contribution of the Langmuir forcing, can be defined as follows

$$\frac{\partial \bar{q}}{\partial t} = A + D + \varepsilon + T^{SGS} + \varepsilon^{SGS} + P + T + B + Q$$

$$A = -\frac{d\langle \bar{p}' \bar{u}_3' \rangle}{dx_3}$$

$$D = \frac{1}{Re_\tau} \frac{d^2 \bar{q}}{dx_3^2}$$

$$\varepsilon = -\frac{1}{Re_\tau} \left\langle \frac{\partial \bar{u}_1'}{\partial x_3} \frac{\partial \bar{u}_1'}{\partial x_3} \right\rangle$$

$$T^{SGS} = \frac{d\langle \tau_{13}' \bar{u}_1' \rangle}{dx_3}$$

$$\varepsilon^{SGS} = -\langle \tau_{13}' \bar{S}_{13}' \rangle \qquad\qquad (5.12)$$

$$P = -\langle \bar{u}_1' \bar{u}_3' \rangle \frac{d\langle \bar{u}_1 \rangle}{dx_3}$$

$$T = -\frac{d\langle \bar{u}_3' \bar{q} \rangle}{dx_3}$$

$$B = Ra_\tau \langle \theta_f \bar{u}_3' \rangle$$

$$Q = -\frac{1}{La_\tau^2} \langle u_1' u_3' \rangle \frac{d\phi_1^s}{dx_3}$$

where $\bar{q} = \langle \bar{u}_i' \bar{u}_i' \rangle / 2$ is the resolved TKE and again, these terms in respective order represent the pressure transport rate (A), the viscous diffusion rate (D), the viscous dissipation rate (ε), the SGS

83

transport rate (T^{SGS}), the SGS dissipation rate (ε^{SGS}), the mean shear production rate (P), the turbulent transport rate (T), the buoyancy production rate (B) and the Stokes drift shear production rate (Q). Note that the budget terms sum to zero in all cases, as the flows are in statistical equilibrium. From this we can get an indication of how each respective mechanism contributes to TKE generation, particularly in the upper half of the water column, prior to analyzing budgets of TKE when both are present in the upcoming chapter.
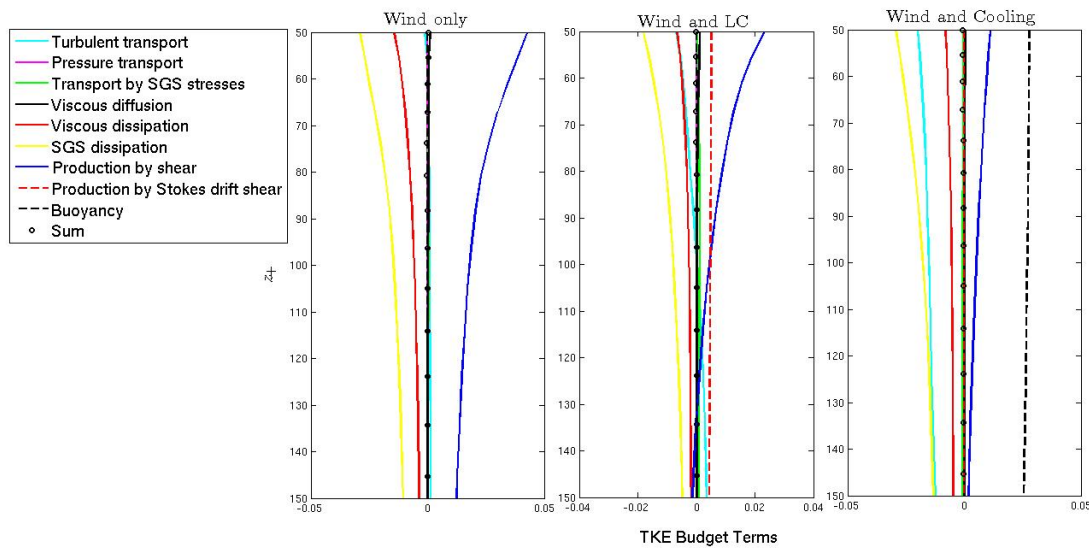

Figure 5.31: Budgets of turbulent kinetic energy in the upper half of the water column: Supercell comparison. Components are scaled by u_τ^2. Cases shown are a) wind only, b)wind and LC and c) wind and surface cooling. z^+ denotes distance from the surface in plus units.

In the case with wind only, on the left in Figure 5.31, we can see the production by mean shear is the sole source of turbulent kinetic energy, and is balanced by SGS dissipation and viscous dissipation only. In contrast, when the Langmuir forcing is present in the center panel, production by Stokes drift shear becomes an active source, and is balanced by an increase in the magnitude of turbulent transport. We can see that in the case with surface cooling applied, the buoyancy now becomes an active source and, in a similar manner to the Langmuir forcing, leads to a correspond-

84

ing increase in turbulent transport. Although the magnitudes of the contributions of each of our respective mechanisms vary, the general pattern of behavior remains consistent.
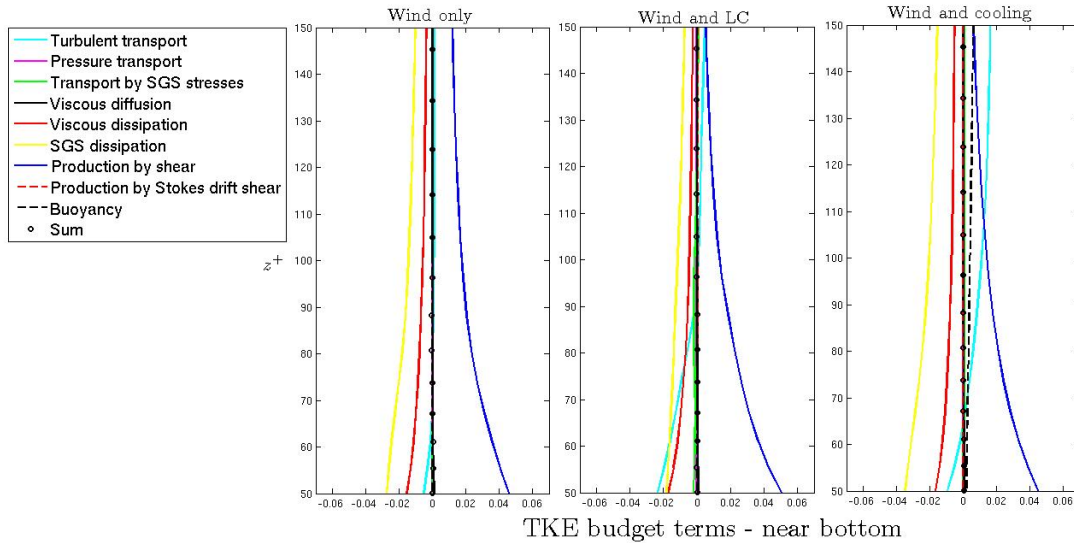

Figure 5.32: Budgets of turbulent kinetic energy in the lower half of the water column: Supercell comparison. Components are scaled by u_τ^2. Cases shown are a) wind only, b)wind and LC and c) wind and surface cooling.

The development of these similar structures under the application of both surface cooling and Langmuir forcing suggested there may be the possibility of full-depth cells in the field being convection-driven, or possibly being "hybrid" cells: generated by a combination of both wind- and wave-driven Langmuir forcing and surface cooling effects. In order to analyze this possibility, the next test to be addressed in Chapter 6 focused on the application of a surface cooling flux, again at both moderate and strong intensities, to a flow with pre-existing full-depth Langmuir supercells. Based on this preliminary understanding of the similarities in cell structures we can compare the turbulence statistics for the flows in which both mechanisms are present and compare flow statistics at each value of the Rayleigh number, with the intention of assessing the respective contribution of each mechanism to the strength and coherence of full-depth cellular structures.

Chapter 6:

Results: Wind and Langmuir-forced Flows with Surface Cooling

Several observations have been made in the LES tests described in the previous chapter. In flows driven by either a constant tidal pressure gradient or a constant surface wind stress, coherent cellular structures acting as a secondary motion to the mean flow and similar to Couette cells observed in a plane Couette flow can be found to develop. When a constant surface cooling flux is applied to these flows, these cellular structures strengthen and merge to form a large, full-depth convection "supercell", again oriented downwind, elongated in the downstream direction and strong enough to cause substantial vertical mixing and homogenization of flow properties.

The goal of the current chapter is to assess the impact of a combination of convection and Langmuir forcing on the turbulence statistics of wind-driven flows in a domain representative of a shallow coastal shelf region. We intend to gain a clearer insight into the relative contribution of each forcing mechanism in the generation of full-depth cell structures as the intensity of surface cooling increases. Furthermore, findings will also be interpreted in terms of the Hoenikker number and Rayleigh number to assess the level of agreement with earlier estimates of the point of transition from Langmuir-dominated to convection-dominated turbulence. It is hoped that the findings of the present study will verify existing field observations and potentially aid the more accurate identification of the nature of cells observed in coastal ocean regions. Additionally it is hoped that these findings will aid the future parameterization of these large structures in coastal circulation models. The major differences in equilibrium dynamics are again examined between three flows:

1) with LC and zero surface heat flux (thus $Ra_\tau = 0$); 2) with LC and a moderate surface cooling flux (such that $Ra_\tau = 211$) and 3) with LC and a strong surface cooling flux (such that $Ra_\tau = 5000$). Again most turbulent quantities analyzed are ensemble-averaged (over x_1, x_2 and time t) and were obtained after the flows had reached statistical equilibrium. Note that the variables presented in the following results are dimensional and hence are scaled by a reference or characteristic scale. All flows are at $Re_\tau = 395$ based on the wind stress fiction velocity. As noted earlier, in the mean the bottom friction velocity is equal to u_τ.

As previously, the large turbulent structures present in our flows corresponding to Langmuir supercells can be visualized in terms of velocity fluctuations averaged over the downwind direction x_1 and time in order to capture the well maintained structures of the flow. Figures 6.1, 6.2 and 6.3 show the a) downwind, b) cross-wind and c) vertical components of these partially averaged velocity fluctuations, for the $Ra_\tau = 0$, $Ra_\tau = 211$ and $Ra_\tau = 5000$ cases respectively.

In all cases the Langmuir supercell structure is visible in these colormaps. The zones of surface and bottom convergence and divergence, and full-depth regions of positive and negative vertical velocity fluctuations representing up- and down-welling limbs, constitute a full-depth supercell resolved in the LES as was seen in the earlier colormaps of flows with LC.

Now, these velocity fluctuations across the vertical plane of the domain can provide some insight into the impact of an increasing Rayleigh number on the Langmuir supercell resolved. All three cases appear very similar, indicating that the application of cooling is not significantly altering the shape of the cells; their cross-stream width and height is being maintained. However, an increased level of symmetry and an increase in the intensity of the up- and down-welling regions is visible at the maximum Rayleigh number.
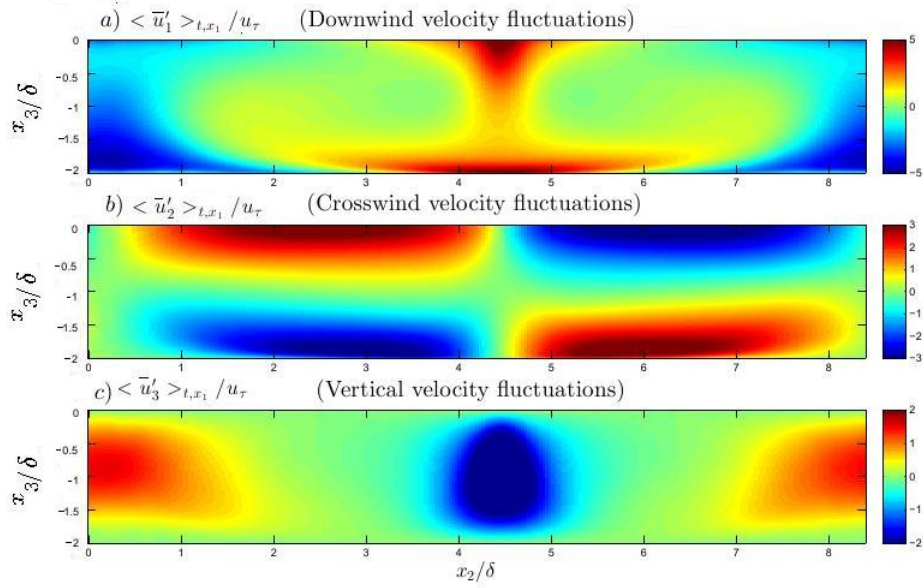
87

Figure 6.1: Vertical plane colormaps of velocity fluctuations: Wind and Langmuir forced flow without cooling. Fluctuations are partially averaged in time and downstream (x_1) direction.
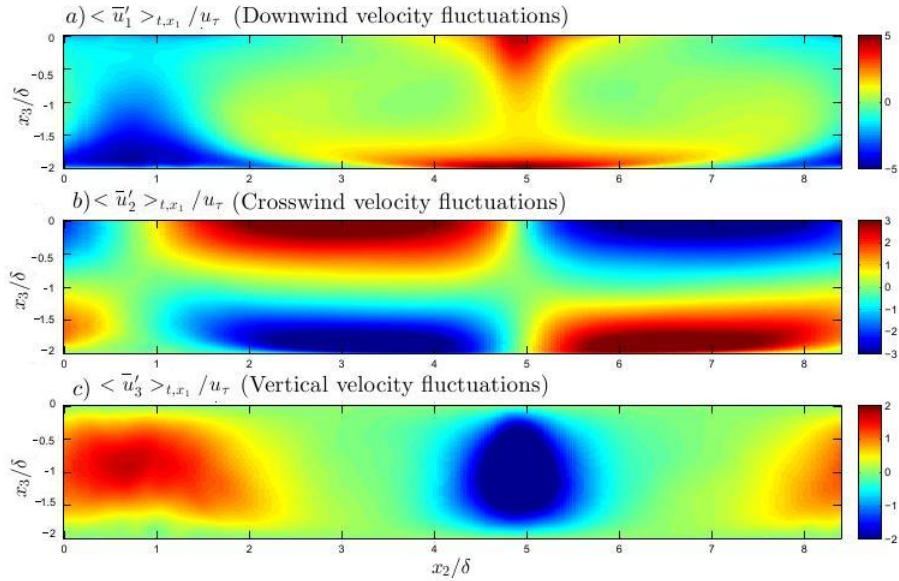

Figure 6.2: Vertical plane colormaps of velocity fluctuations: Wind and Langmuir forced flow with cooling ($Ra_\tau = 211$). Fluctuations are partially averaged in time and downstream (x_1) direction.
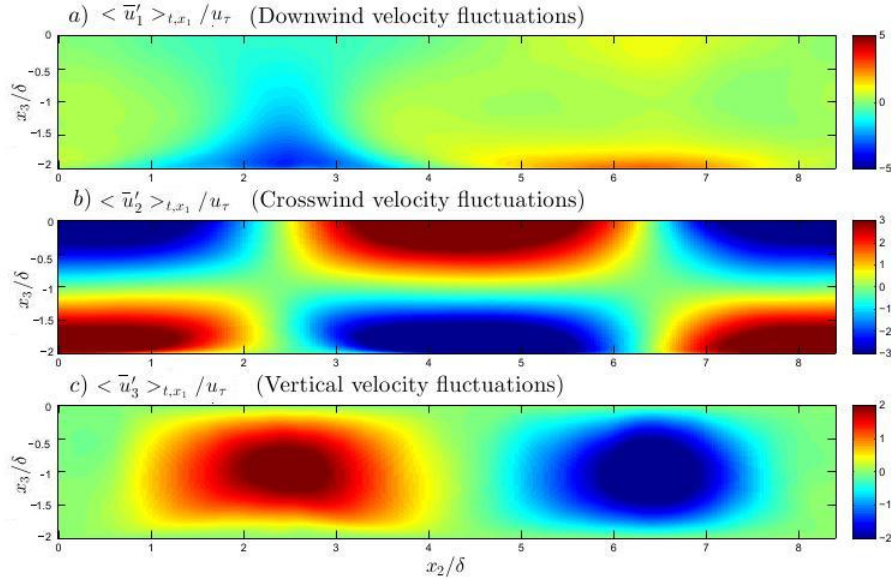
88

Figure 6.3: Vertical plane colormaps of velocity fluctuations: Wind and Langmuir forced flow with cooling ($Ra_\tau = 5000$). Fluctuations are partially averaged in time and downstream (x_1) direction.

Next we may again consider the mean stream-wise velocity profiles as a function of depth in standard units, now for the full depth of the water column, the surface boundary layer, and the bottom boundary layer (the latter two with emphasis on the viscous sub-layer ($x_3^+ \leq 5$), the buffer layer ($5 \leq x_3^+ \leq 30$) and the log layer ($30 \leq x_3^+ \leq 100$)). Profiles are shown for wind-driven flows with LC featuring $Ra_\tau = 0$, $Ra_\tau = 211$ and $Ra_\tau = 5000$, and additionally profiles from the wind-driven flow without either Langmuir circulation or a surface heat flux (again denoted *wind-only*) are also included for comparison.

Considering first the mean stream-wise velocity profile in standard units for the whole column depth (Figure 6.4a), it can be seen that in the $Ra_\tau = 0$ case with LC present, the vertical turbulent mixing induced by the full-depth up- and down-welling limbs of the Langmuir cell structure described previously causes homogenization of the flow velocity throughout the bulk of the water column. As already seen in Chapter 4, this leads to a uniform profile over the bulk region of the

89

flow. When the strong surface cooling is applied at a value of $Ra_\tau = 5000$, this homogenization reaches further up toward the surface, making the surface boundary layer thinner and suggesting an increase in the strength of the vertical mixing. Note the velocity profile with a Rayleigh number of 211 is not noticeably different from the LC case without surface cooling.

In the center panel (Figure 6.4b) is seen the mean velocity deficit in terms of wall units in the upper half of the water column. The log law profile is indicated in the figure by the dotted line, and represents the behavior of a typical turbulent flow at a wind-driven surface; it is clear to see that a wind-driven case without LC nor surface cooling closely follows this expected profile. In all flows with LC we see the disruption of the classical log-law velocity profile characterizing a traditional turbulent boundary layer, and when cooling with $Ra_\tau = 5000$ is applied this disruption is at a maximum.

In the third panel on the right hand side of Figure 6.4 is the flow velocity in wall units in the bottom boundary layer region. Again, the log law profile expected of a typical turbulent flow over a no-slip boundary is indicated by the dotted line. Initially note the close correlation between the log layer behavior of the flow without LC nor cooling (wind-only) and the expected theoretical log layer profile. At all Rayleigh numbers, the application of LC again leads to the disruption of the usual log law velocity profile characterizing a traditional turbulent boundary layer. The curvature of the profile away from the expected log profile is behavior typically seen at greater distances from the wall where the log region ends and a wake region begins. However, notice here that as the Rayleigh number increases to 5000, the magnitude of the velocity actually becomes closer to that in the expected profile. This milder log law disruption corresponds to the increased level of symmetry of the up- and down-welling regions visible in the vertical plane colormaps shown earlier in Figure 6.3 for the LC case with $Ra_\tau = 5000$.

Notice the case with LC and $Ra_\tau = 211$ demonstrates little, if any, difference from the case with LC and $Ra_\tau = 0$ in these velocity profiles, a suggestion that the moderate surface cooling may be too weak to cause significant alterations to the structure of pre-existing Langmuir supercells.
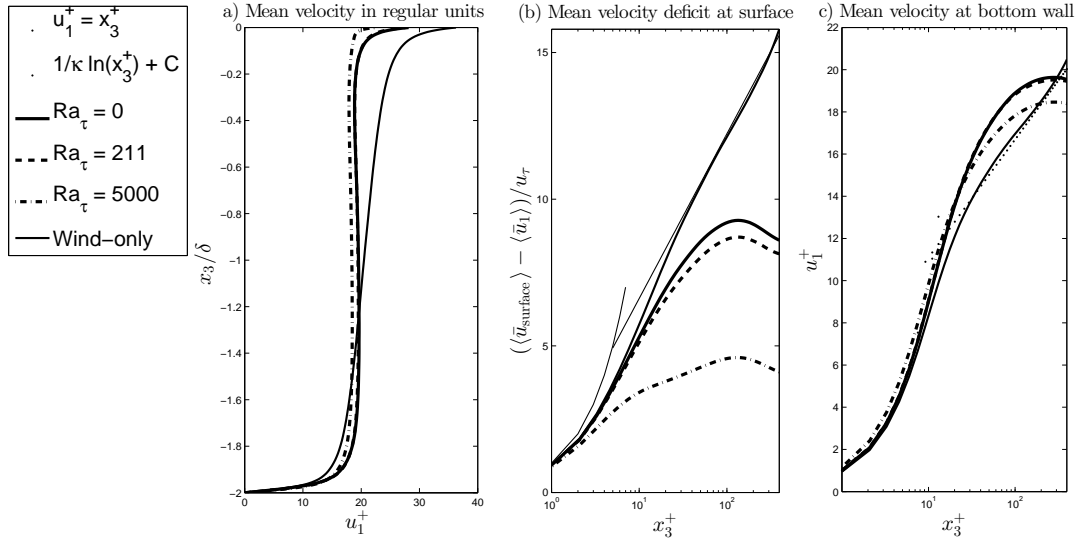

Figure 6.4: Mean velocity profiles: Wind-driven flow with LC and cooling. a) Mean streamwise velocity profile as a function of depth, b) Mean streamwise velocity deficit in wall units at upper surface with x_3^+ denoting distance to the surface in plus units and c) Mean streamwise velocity in wall units at lower wall with x_3^+ denoting distance to the bottom in plus units.

To further assess the impact of cooling, a comparison of the root mean square (RMS) of the velocity fluctuations described previously can again be conducted for the cases with $Ra_\tau = 0$, $Ra_\tau = 211$ and $Ra_\tau = 5000$ (Figure 6.5). First observe the influence of the cell structure in the RMS profiles. For all cases with LC, the regions of surface and bottom convergence and divergence of the supercell structures (observed earlier in Figures 6.1-6.3) are identifiable by the higher magnitudes of crosswind velocity RMS at the near surface and near bottom of the water column when compared to the mid-depth, visible in the center panel in Figure 6.5b. In the panels in Figure 6.5b and 6.5c, observe that the crosswind and vertical velocity RMS both increase with increasing Ra_τ and thus strength of supercell structure.

91

Considering next downwind velocity RMS, we can see in Figure 6.5a on the left the case with $Ra_\tau = 5000$ demonstrates an increased velocity fluctuation in the middle of the water column with a less distinct gradient in the respective upper and lower halves of the water column than the cases with $Ra_\tau = 0$ and $Ra_\tau = 211$ due to the increased turbulent mixing and homogenization in this case.
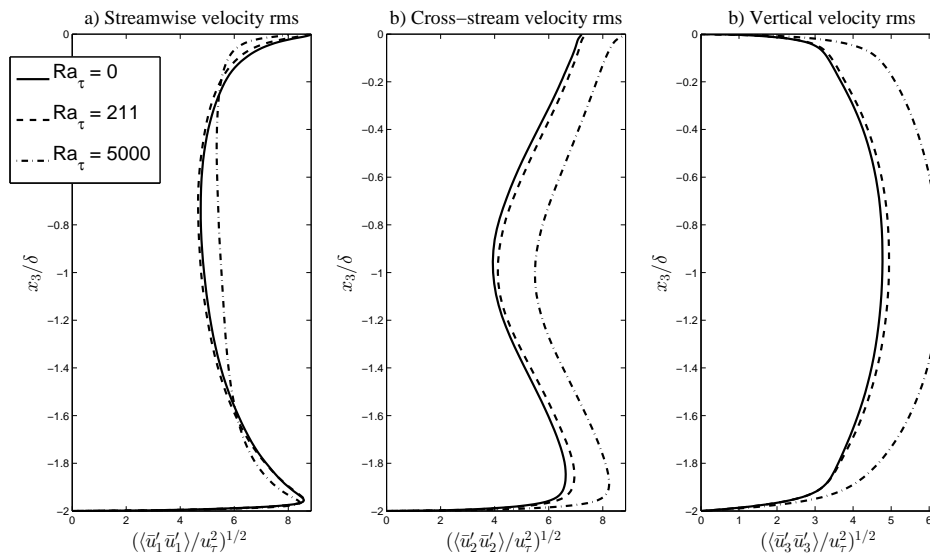

Figure 6.5: RMS of velocity fluctuations: Wind-driven flow with LC and cooling

Another revealing diagnostic of the structure of the turbulence is the depth trajectory of the Lumley invariants of the resolved Reynolds stress anisotropy tensor (mapped as a function of distance from the bottom of the channel), which for a realizable flow must lie within the Lumley triangle [24]. We can map these "Lumley invariants" using the second and third invariants of the

anisotropy tensor b_{ij}:

$$b_{ij} = \frac{< \bar{u}'_i \bar{u}'_j >}{2\bar{q}} - \frac{\delta_{ij}}{3}$$

$$I = trace(b_{ij}) = 0$$

$$II = b_{ij}b_{ji} \qquad (6.1)$$

$$III = b_{ij}b_{jk}b_{ki}$$

Now $II^{(1/2)}$ is a measure of the magnitude of the anisotropy. The location of the coordinate ($II^{(1/2)}$, $III^{(1/3)}$) is a measure of the shape of the anisotropy (the state of the resolved turbulence). All possible states of fluctuating motion are constrained to lie within the triangular region shown in Figure 6.6. The two sides emanating from 0 represent axisymmetric turbulence; the origin represents 3-D isotropic turbulence. The right hand side edge of the triangle, where $III > 0$, is turbulence for which two eigenvalues of the Reynolds stress tensor are smaller than the third: the upper right corner of the triangle corresponds to one-component turbulence. The left hand side in which $III < 0$ corresponds to turbulence in which two eigenvalues are larger than the third: the upper left corner of the triangle corresponds to two-component isotropic turbulence. The bottom vertex of the triangle corresponds to three-component isotropic turbulence.

In flows without surface cooling or Langmuir forcing, we would expect to see the typical structure of shear-dominated turbulence, in which the downstream component ($< \bar{u}'_1 \bar{u}'_1 >$) is greater than the vertical ($< \bar{u}'_2 \bar{u}'_2 >$) and cross stream ($< \bar{u}'_3 \bar{u}'_3 >$) components, particularly in the middle of the water column as the distance away from the bottom wall increases. This leads to a 'one-component' or 'cigar shaped' profile. In a flow in which wind- and wave-forcing lead to the generation of LC, in the near-bottom and near-surface regions the Lumley profile should reveal a

93

two-component structure in which the downwind and crosswind components are of the comparable magnitude and both are much greater than the vertical component due to the convergence and divergence of the supercells in these regions.
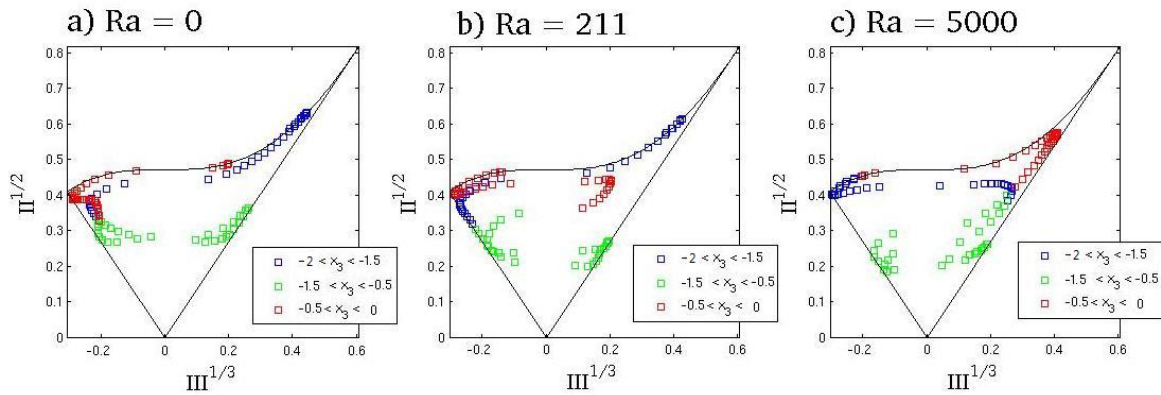

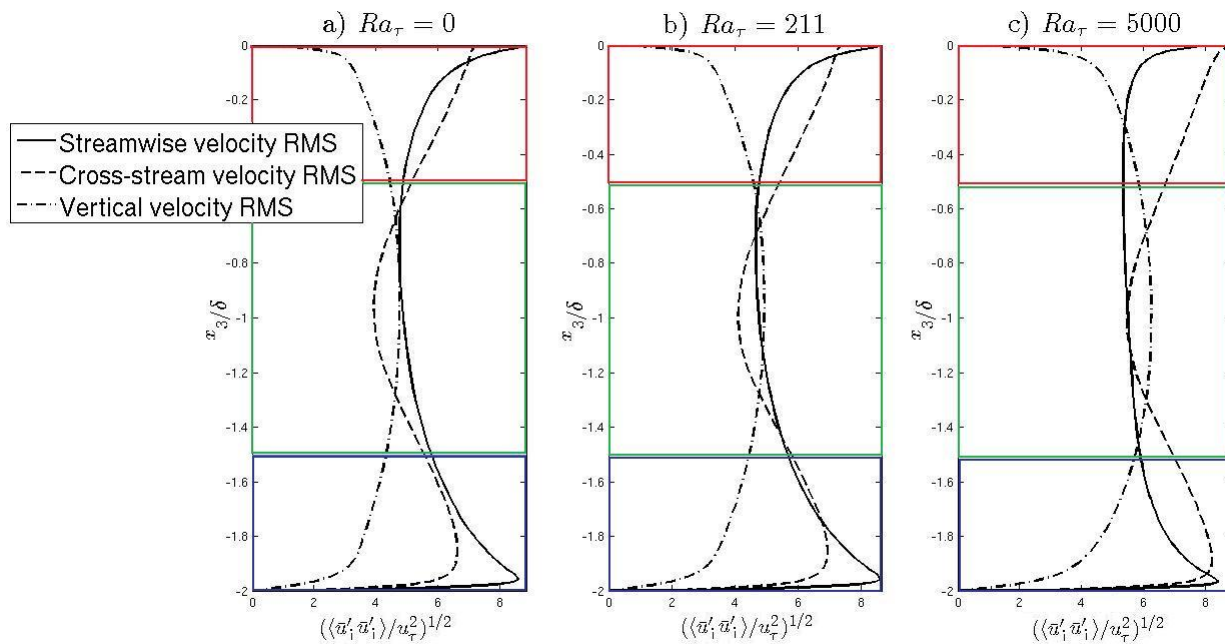Figure 6.6: Lumley invariants: Wind and Langmuir forced cases with surface cooling

Figure 6.7: RMS of velocity fluctuations in regions identified by Lumley invariants: Wind-driven flow with LC and cooling

We can consider these Lumley invariants for our three flows with Rayleigh numbers of 0, 211 and 5000 respectively. Initially, see the left hand side panels in Figures 6.6 and 6.7, representing

94

the case with LC only and no surface cooling flux. In the Lumley invariant maps, we can see that at the very bottom of the water column, the flow is dominated by one-component turbulence, transitioning into two-component with increasing distance from the lower wall (but remaining in the lower $1/4$ of the water column). Near the surface, the flow is characterized by two-component turbulence tending towards one-component turbulence as the surface is approached. If we compare this to the RMS of velocity fluctuations for the same flow, we can see this corresponds to the shear-driven maximum in the streamwise component of rms ($< \bar{u}_1' \bar{u}_1' >$) near the wall, which, as distance from the wall increases, is then matched in magnitude by the cross-stream component ($< \bar{u}_2' \bar{u}_2' >$) where the zone of bottom divergence of the resolved Langmuir supercell is strong. Similarly in the upper half of the water column, with increasing distance from the surface $< \bar{u}_2' \bar{u}_2' >$ becomes significant due to the region of surface convergence of the supercell, again leading to a two-component structure; the RMS profiles demonstrate the comparable magnitude of $< \bar{u}_1' \bar{u}_1' >$ and $< \bar{u}_2' \bar{u}_2' >$ here. Again, wind shear leads to $< \bar{u}_1' \bar{u}_1' >$ being dominant right at the surface and tending the flow towards one-component turbulence.

When maximum cooling is applied at a Rayleigh number of 5000, notice at the very bottom of the water column, in contrast to the case with $Ra_\tau = 0$, both $< \bar{u}_1' \bar{u}_1' >$ and $< \bar{u}_2' \bar{u}_2' >$ are large and comparable in magnitude, hence the map of Lumley invariants begins in the top left of the triangle: a two-component state. As distance from the wall increases, $< \bar{u}_2' \bar{u}_2' >$ increases in magnitude to become dominant in the flow at $Ra_\tau = 5000$ (and hence the Lumley invariant map shows movement into one-component turbulence towards the right of the triangle) due to the increased strength of the regions of divergence of the supercell near the lower wall. Similarly in the surface region, the intensity of the convergence zone leads the cross-stream component to be significantly larger than the downstream and vertical velocity RMS resulting in the Lumley invariants map moving

95

to the right side edge of the triangle. Notice in the complex mid-depth region, as distance from the surface increases into the "green" region, we see the dominance of cross-stream fluctuations be overtaken by dominance of vertical fluctuations where the regions of up- and down-welling characterising the Langmuir-convective supercell are strong.

As we have previously established, by plotting the vertical velocity variance we can quantify the strength of the cells visible on the vertical plane colormaps in Figures 6.1-6.3. Recall the instantaneous vertical velocity variance can be calculated as

$$\langle \bar{u_3}' \bar{u_3}' \rangle_{x_1,x_2} = \langle \langle \bar{u_3}' \rangle_{x_1} \langle \bar{u_3}' \rangle_{x_1} + \bar{u_3}'' \bar{u_3}'' + 2\bar{u_3}'' \langle \bar{u_3}' \rangle_{x_1} \rangle_{x_1,x_2} \tag{6.2}$$

where the contribution due to large-scale coherent cell structures is defined as

$$\langle \bar{u}_3' \bar{u}_3' \rangle_{CC} = \langle \langle \bar{u}_3' \rangle_{x_1} \langle \bar{u}_3' \rangle_{x_1} \rangle_{x_1,x_2} \tag{6.3}$$

Although it has seemed from the results shown above the $Ra_\tau = 0$ and $Ra_\tau = 211$ cases are exhibiting nearly the same turbulence intensities, it is visible from the magnitude of the vertical velocity variance that the application of moderate surface cooling does in fact lead to an increase in cell strength when compared to the case with a zero surface heat flux, somewhat enhancing the circulation originally driven by LC (Figure 6.8). At a Rayleigh number of 5000 this increase in cell strength is more pronounced.
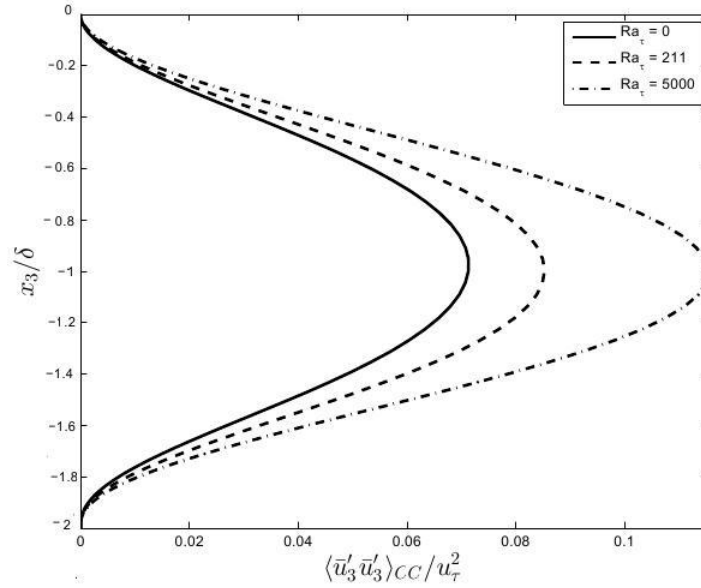
96

Figure 6.8: Instantaneous vertical velocity variance for varying values of Ra_τ: Wind-driven flow with LC

Next we may consider the sinks and sources of turbulent kinetic energy (TKE) where the transport equation for resolved turbulent kinetic energy now featuring a Stokes-drift shear production term representing the contribution of the Langmuir forcing was defined in Chapter 5.

Initially, consider budgets of TKE for the three preliminary tests described earlier: a flow with surface wind stress only, and flows with Langmuir forcing and surface cooling respectively acting in isolation. From this we can get an indication of how each respective mechanism contributes to TKE generation, particularly in the upper half of the water column, prior to analyzing budgets of TKE when both are present.

In the case with wind only, on the left in Figure 6.9, we can see the production by mean shear is the sole source of turbulent kinetic energy, and is balanced by SGS dissipation and viscous dissipation only. In contrast, when the Langmuir forcing is present in the center panel, production by Stokes drift shear becomes an active source, and is balanced by an increase in the magnitude

97

of turbulent transport corresponding to the increased vertical mixing. We can see that in the case with surface cooling applied, the buoyancy now becomes an active source and, in a similar manner to the Langmuir forcing, leads to a corresponding increase in turbulent transport. Although the magnitudes of the contributions of each of our respective mechanisms vary, the general pattern of behavior remains consistent. For example in flows with LC and surface cooling, mean shear becomes negative at depths below the surface, thereby becoming a sink of TKE.
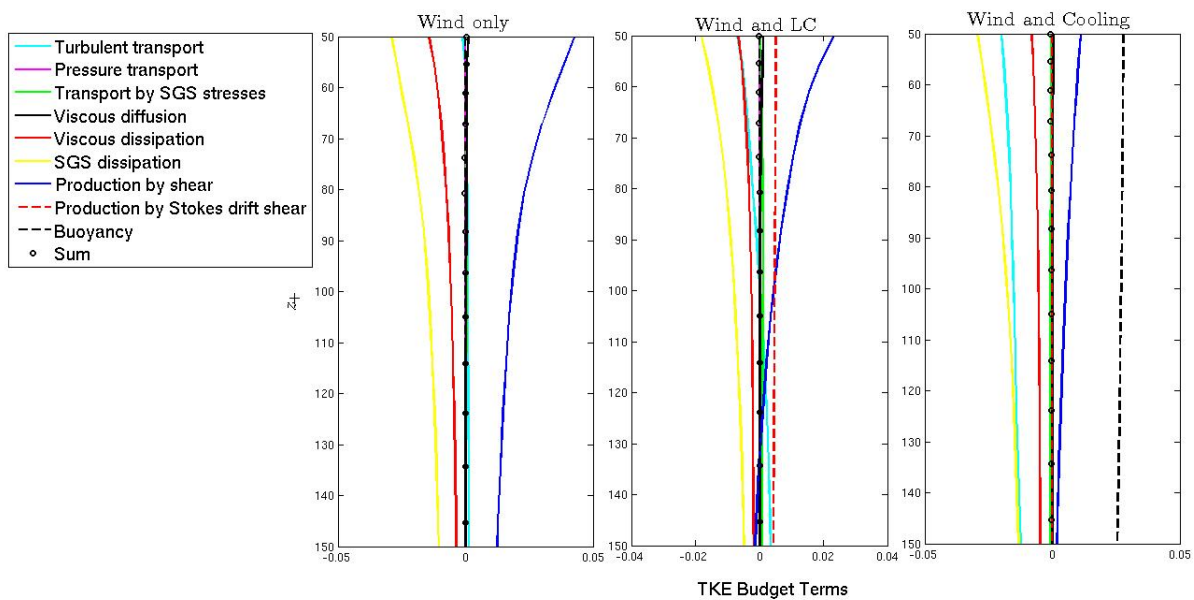
Figure 6.9: Budgets of turbulent kinetic energy in the upper half of the water column: Supercell comparison. Shown are cases with a) wind only, b)wind and LC and c) wind and surface cooling with $Ra_\tau = 5000$. Budgets are scaled by u_τ^2. z^+ denotes the distance to the surface in plus units.

Now we may consider the sinks and sources of turbulent kinetic energy in the upper half of the water column in our flows with both mechanisms present, in order to assess the impact of the combinations of forcing mechanisms on surface dynamics.
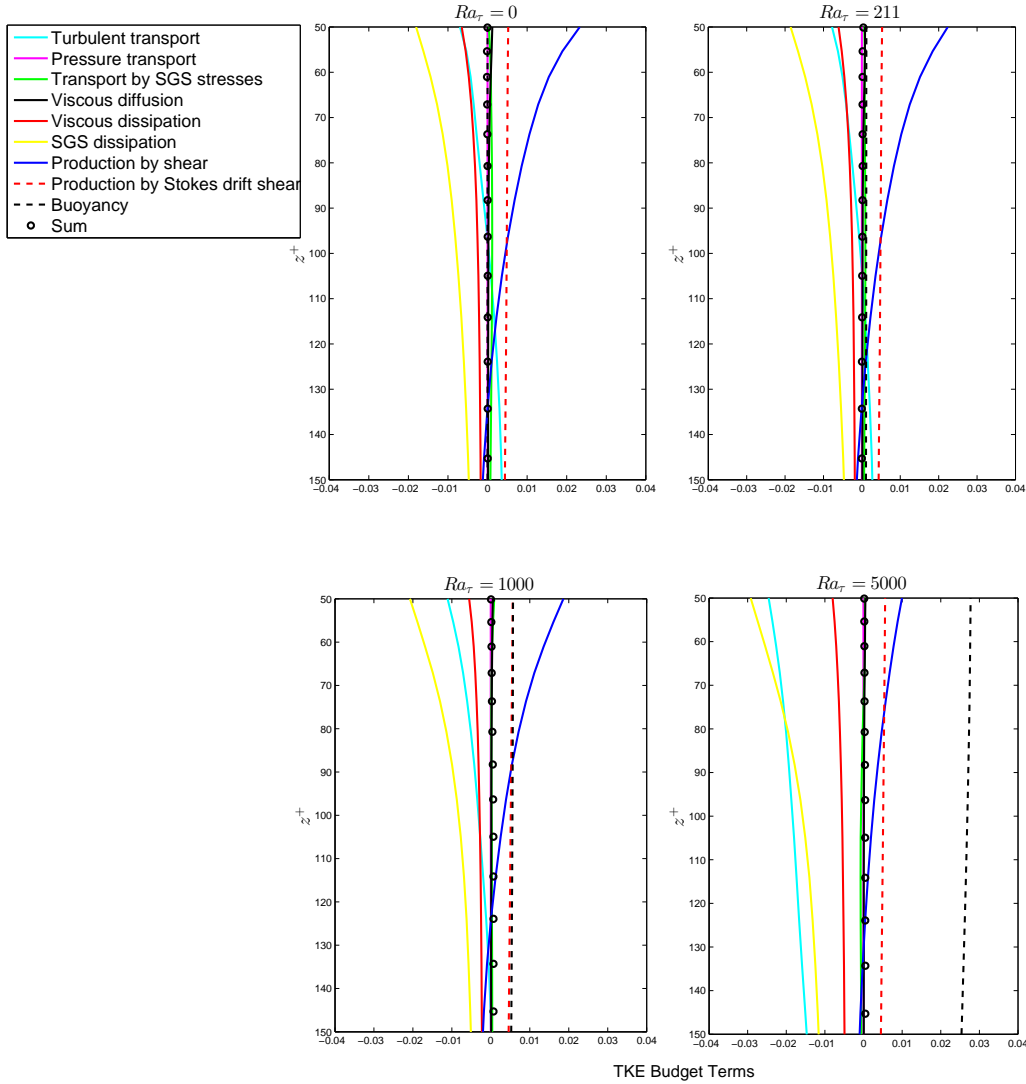
98

Figure 6.10: Budgets of turbulent kinetic energy in the upper half of the water column: Wind and LC case with surface cooling. Shown are cases with a) $Ra_\tau = 0$, b) $Ra_\tau = 211$, c) $Ra_\tau = 1000$ and d) $Ra_\tau = 5000$ respectively. Budgets are scaled by u_τ^2. z^+ denotes distance to the surface in plus units.

In the cases with $Ra_\tau = 0$ and $Ra_\tau = 211$, visible in the two upper panels of Figure 6.10, it can be seen that mean shear and Stokes drift shear dominate TKE production. When maximum cooling is applied by $Ra_\tau = 5000$, as seen in the lower right panel, buoyancy clearly dominates over Stokes drift shear as the main source of turbulent kinetic energy by a significant margin, suggesting the turbulent structures visible in the case with $Ra_\tau = 5000$ are primarily driven by the cooling-

99

induced buoyant motion. Based on the implication that at some point between the original two non-zero Rayleigh numbers of 211 and 5000 a transition had occurred from Langmuir-dominated to convective-dominated turbulence, it was possible to determine the point at which this transition occurred. This involved finding the value of the Rayleigh number for which buoyancy would overtake Stokes drift shear in terms of being the main source of turbulent kinetic energy. From the panel in the bottom left of Figure 6.10 it can be seen that at a Rayleigh number of 1000, these sources are approximately equal in their contribution. Hence, for any Rayleigh number above $Ra_\tau = 1000$, the expectation is that convection will be the primary source of turbulent kinetic energy. Note that viscous dissipation is a significant sink in all 4 cases, with SGS dissipation and turbulent transport being the most prominent sinks and increasing in magnitude to balance the increasing buoyancy with increasing Rayleigh numbers. Additionally, there is a visible increase in turbulent transport with the increase in Rayleigh number.

Quantification of the point at which a transition from Langmuir to convective turbulence may occur has been attempted by means of the Hoenikker number Ho, defined as the ratio of the buoyant forcing that drives thermal convection to the Craik-Leibovich vortex force that drives LC (Li and Garrett, 1995). It was suggested by McWilliams et al. (1997) that $Ho > 1$ leads to the transition to convection-driven turbulence. Following this, Li et al. (2005) observed that the value of Ho required for this transition to occur is around $Ho = O(1)$, and additionally that "typical" heat fluxes and wind speeds generate only $Ho = O(0.01)$.

It is possible to consider the findings of the present LES of wind and Langmuir-forced flow now in terms of the Hoenikker number, formally defined by:

$$Ho = \frac{-2\beta g Q}{\rho_0 C_p \kappa u_s u_\tau^2} \qquad (6.4)$$

where again β is the thermal expansion coefficient, g is the gravitational acceleration, Q is the net heat flux, ρ_0 the density, C_p the specific heat and κ is the wavenumber of the dominant surface waves. The Hoenikker number is negative when the surface heat flux is stabilizing, and positive when the surface heat flux is destabilizing. Our primary Rayleigh numbers of 211 and 5000 correspond to Hoenikker numbers of approximately 1 and 25, respectively. A Rayleigh number of 1000 generates $Ho = 4.7$, suggesting that when $Ho > 4.7$, the transition to convection-driven turbulence has occurred. This value lies comfortably within the approximate ranges identified by Li et al., and McWilliams et al of $Ho = O(1)$ and $Ho > 1$ respectively, for convection-dominated turbulence.

More recently, Gargett and Grosch (2014) have also suggested that convection is dominant when $\log(Ra) > 7.5$ and $\log(La) > 0$, where Ra is a Rayleigh number defined in a slightly different manner to the one used in the present testing but still describing the importance of destabilizing buoyancy forces relative to the same inertial forces, and La is a Langmuir number defined as $La = La_t^2$; the definition of La_t was provided earlier in Chapter 3. We may conduct a similar analysis of the expected transition to convection-dominated turbulent using this method. The definition of the Rayleigh number by Gargett and Grosch (2014) is

$$Ra = \frac{\beta g}{k}(Q t_*^2) \qquad (6.5)$$

101

(adapted to use the notation of the present thesis) where again β is the coefficient of thermal expansion, k the thermal conductivity and Q the heat flux, and now we include new variable t_* which is defined as

$$t_* = (\frac{dU_s}{dx_3}\frac{\partial <u_1>}{\partial x_3})^{-1/2} \tag{6.6}$$

where dU_s/dx_3 and $\partial <u_1>/\partial x_3$ are the dimensional vertical gradients of Stokes drift and mean streamwise velocity at the surface. Using this definition we can calculate that the moderate surface cooling ($Ra_\tau = 211$) defined in the present LES, which demonstrated minimal impact on full-depth LC in our statistical analysis, features a value of $log(Ra) = 5.58$, below the threshold for convection-driven turbulence of 7.5 as defined by Gargett and Grosch. The case in the current LES for which we observed the Langmuir forcing and surface cooling-induced buoyancy were of approximately equal magnitude in their contribution to the turbulent kinetic energy ($Ra_\tau = 1000$ by our original definition), leads to $log(Ra) = 7.19$ using the new methodology. This corresponds well with our hypothesis that as the Rayleigh number Ra_τ in our original definition increases beyond 1000 convection-driven turbulence is able to dominate production of TKE. When $Ra_\tau = 1500$ by our original definition, the analysis of Gargett and Grosch suggests that $log(Ra) = 7.59$, within the range for which they hypothesize convection is able to dominate.

Next we can consider budgets of resolved Reynolds stress, again in the surface region. The transport equations for the resolved Reynolds shear stress $- <\bar{u}_1' \bar{u}_3'>$, again now with the inclusion of a term accounting for the production by Stokes drift shear, are

$$\frac{\partial \bar{q}}{\partial t} = A + D + \varepsilon + T^{SGS} + \varepsilon^{SGS} + PSR + P + T + B + Q \tag{6.7}$$

102

where

$$A = -\frac{d\langle \bar{p}'\bar{u}_1'\rangle}{dx_3}$$

$$D = \frac{1}{Re_\tau}\frac{d^2\langle \bar{u}_1'\bar{u}_3'\rangle}{dx_3^2}$$

$$\varepsilon = -\frac{2}{Re_\tau}\left\langle \frac{\partial \bar{u}_1'}{\partial x_3}\frac{\partial \bar{u}_3'}{\partial x_3}\right\rangle$$

$$T^{SGS} = \frac{d\langle \tau_{13}'\bar{u}_3'\rangle}{dx_3}$$

$$\varepsilon^{SGS} = -\langle \tau_{13}'\frac{\partial \bar{u}_3'}{\partial x_3}\rangle - \langle \tau_{33}'\frac{\partial \bar{u}_1'}{\partial x_3}\rangle \tag{6.8}$$

$$PSR = 2\langle \bar{P}'\bar{S}_{13}'\rangle$$

$$P = -\langle \bar{u}_3'\bar{u}_3'\rangle\frac{d\langle \bar{u}_1\rangle}{dx_3}$$

$$T = -\frac{d\langle \bar{u}_1'\bar{u}_3'\bar{u}_3'\rangle}{dx_3}$$

$$B = Ra_\tau\langle \theta_f\bar{u}_1'\rangle$$

$$Q = \frac{1}{La_\tau^2}\langle \bar{u}_1'\bar{u}_1'\rangle\frac{d\phi_1^s}{dx_3}$$

These terms represent the pressure transport rate (A), the viscous diffusion rate (D), the viscous dissipation rate (ε), the SGS transport rate (T^{SGS}), the SGS dissipation rate (ε^{SGS}), the mean shear production rate (P), the turbulent transport rate (T), the buoyancy term (B) and the Stokes drift shear production (Q).

We may consider these budgets of Reynolds shear stress in the upper half of the water column within the region between $x_3^+ = 100$ and $x_3^+ = 395$ from the surface to further assess turbulent transport associated with the presence of the full-depth cells. First of all note that the production by mean velocity shear becomes a sink (and thus destruction) between $x_3^+ = 100$ and $x_3^+ = 150$

103

in all the cases described, unlike in wind-driven flow without LC or surface cooling (not shown) where it was a significant source. In the lower regions, in the cases with $Ra_\tau = 0$ and $Ra_\tau = 211$, as long as the mean velocity shear is a sink, turbulent transport (and pressure transport) are balancing this as a source, although still remain smaller in magnitude than the Stokes drift shear production. When $Ra_\tau = 5000$, mean velocity shear is a significantly greater sink and the turbulent transport is correspondingly a greater source, equal in magnitude to the Stokes drift shear. This implies that in a turbulence model of the Reynolds shear stress, the model should include a non-local transport term to account for both LC and cooling.
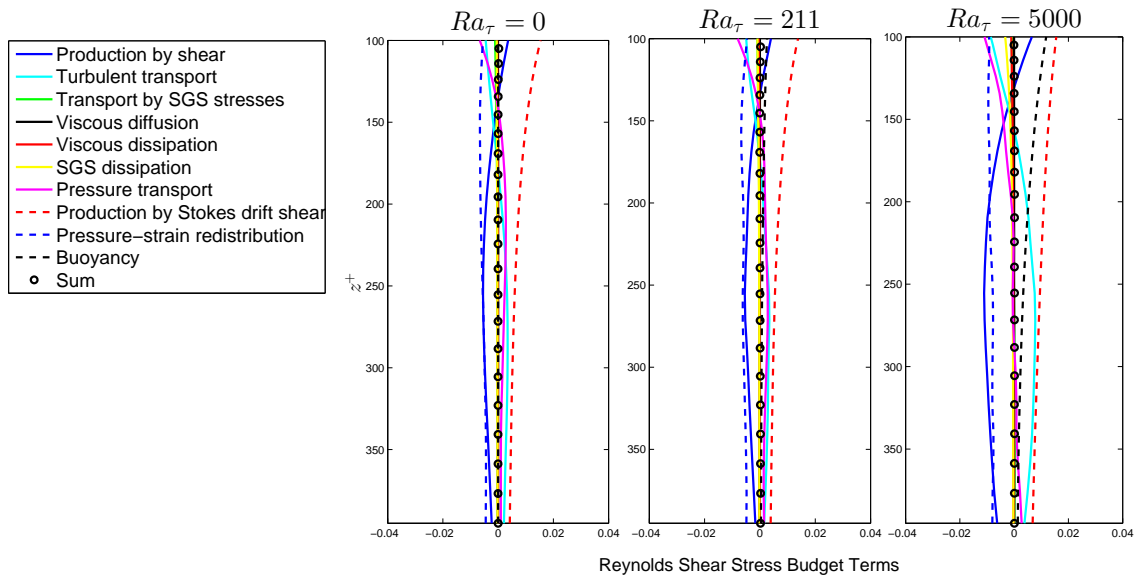
Figure 6.11: Budgets of resolved Reynolds stress in the upper half of the water column: Wind-driven flow with LC and cooling. Terms are scaled by u_τ^2 and shown in the region $100 < x_3^+ < 395$ from the surface of the water column in cases with a) $Ra_\tau = 0$, b) $Ra_\tau = 211$ and c) $Ra_\tau = 5000$ respectively. z^+ measures the distance to the surface in plus units.

We have analyzed diagnostics of flows with Langmuir circulation and either zero surface heat flux, a moderate surface cooling flux or a strong surface cooling flux. The turbulent structures have been analyzed by means of mean velocity profiles, rms of velocity fluctuations, plane colormaps

104

of velocity fluctuations, and budgets of turbulent kinetic energy and Reynolds shear stress. It was found that although the overall cell features remain intact, the increasing of the Rayleigh number (therefore increasing the effect of surface buoyancy relative to surface shear stress) when applied to a fully mixed water column in the presence of Langmuir forcing can lead to strengthening of full-depth structures. At a Rayleigh number of 5000, the increase in cell strength is sufficient to dramatically alter the turbulence dynamics, with buoyancy becoming the dominant source of TKE. However, at a Rayleigh number of 211 representing a moderate surface cooling flux of approximately 200 W/m^2, despite the fact convection appears to create similar turbulent mechanisms to LC at higher values of the heat flux out of the surface, it is unable to overtake Langmuir forcing as the dominant mechanism in turbulence generation, and LC remains the primary cause of large-scale cell structures.

The significant contribution of buoyant forces at sufficiently high Ra_τ values to the turbulence dynamics and cell structure implies there is potential for cells found in the field to be "hybrids", with the turbulence observed being generated by a combination of Langmuir and convective forcing. However, at "typical", or moderate levels of surface cooling flux, turbulent Langmuir number and wave height, it would seem convection is not strong enough to dominate cell generation, only to slightly enhance or strengthen Langmuir-driven motion. This observation is supported by the findings of Scully (2014) who observed in the field that a destabilizing heat flux can augment the circulation driven by LC, generating an increase in vertical velocity fluctuations of approximately 10%, but LC remains the dominant mechanism driving coherent low-frequency motions in the surface boundary layer at surface cooling fluxes up to 400 W/m^2.

Based on additional testing, it appears from the current study that in a flow domain as described in this paper, a Rayleigh number greater than approximately 1000, corresponding to a Hoenikker

105

number of over 4.7, would be required for such cells to be deemed either hybrid or convection-driven, requiring either a significantly higher heat flux or a substantially lower wind stress than those tested in the present work of $Q = 200\,\mathrm{W/m^2}$ and $\tau_w = 0.1\,\mathrm{N/m^2}$ respectively.

Chapter 7:

Results: Tidal Forcing

Based on the observations of the previous two chapters we have reached the following conclusions:

- The application of a constant surface cooling flux to a channel flow driven by either a constant surface shear stress or a constant pressure gradient can lead to the development of full-depth convection supercells, similar in structure to Langmuir supercells observed in the field.

- At typical values of a surface cooling flux as would be expected in the field, although this convective mechanism is able to augment the strength of pre-existing Langmuir cell structures somewhat, it is not sufficiently strong to take over from Langmuir forcing as the dominant mechanism in cell production.

- Based on analysis of the Hoenikker number and alternative forms of the Rayleigh number, we may conclude that a surface heat flux of approximately $1000W/m^2$ would be required for the surface cooling flux to take over as the dominant mechanism in the generation of turbulent kinetic energy, if all other conditions outlined in the previous tests remained constant.

Recall in Chapter 1 we discussed the effect of a crosswind tide on existing cellular structures. In [11] a combination of field observations and LES were used to assess this effect. From field measurements it was observed that during periods of crosswind currents of approximately $0.2m/s$,

107

LC is less coherent than in the absence of crosswind forcing. At an approximately equal crosswind tidal force but with greater wave forcing (ie stronger Langmuir forcing and smaller La_t), the cells remained more coherent, although still not at the full strength of the case without a crosswind tidal force present. In the same study, LES of a comparable flow supported this disruption of cellular structures under a crosswind tidal force and demonstrated the merging of two coherent cell pairs into one weaker cell. Additionally, this study suggested that an attraction mechanism exists between up- and down-welling regions of the cell under this crosswind force leading to the merging of cells. In [17], on the other hand, it was shown via LES that the application of a crosswind forcing component does not fundamentally alter the structure and coherency of the cells, however in this case the wavelength of the surface waves was almost three times greater than that in the LES of [11].

The goal of the present chapter is to consider in greater detail the effects of this crosswind tidal forcing on pre-existing full-depth Langmuir cells through a comparison of flows with different crosswind tidal magnitudes. In the first of these tests at water column mid-depth the crosswind tidal velocity will be approximately 150% of the downwind velocity, and in the second the crosswind tidal velocity will be 50% of the downwind. It is hoped this may provide some insight into how to quantify the effect of this crosswind tide on pre-existing LC based on this single ratio parameter, to complement existing observations and LES studies. Further to this, we can consider the effect of the application of a surface cooling flux to each of these flows to see if this is able to affect the response of the LC to the crosswind force, potentially limiting the extent to which cell weakening may occur. This will be done by analysis of flow characteristics when those tidal forces are fixed, such that we are able to allow the flow to reach a statistically steady state to provide greater insight into the mechanisms at play.

108

As a crosswind forcing mechanism is being applied, these tests were conducted on a flow domain double the width of those already discussed such that $Ly = 16 * \pi/3$ (or in dimensional form approximately 80 m). The intention of this is to ensure the flow domain is able to capture any potential merging of cellular structures in this direction, based on the observations of [11] demonstrating the transition of two cell pairs into one under similar conditions. The base structure of LC in this domain (without surface cooling nor tidal forcing applied) is shown in Figure 7.1 below. This base structure was used as the initial condition for the flows with constant crosswind tidal forcing applied.
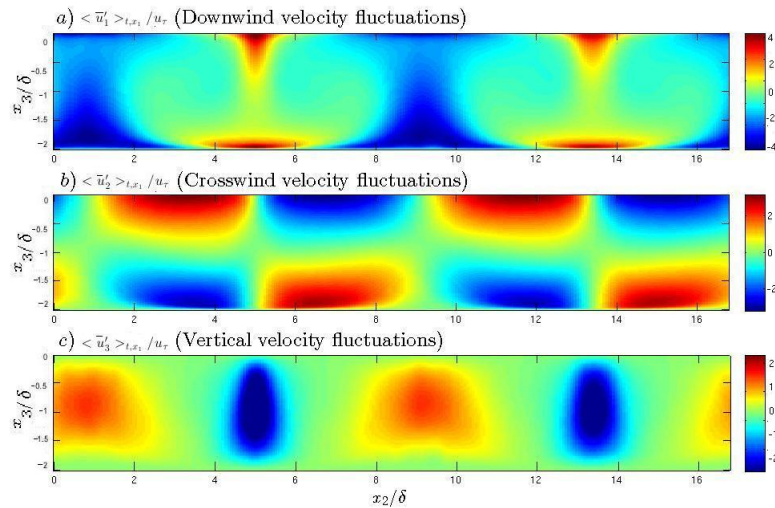
Figure 7.1: Vertical plane colormaps of velocity fluctuations: Wind and Langmuir-forced flow (i.e. flow with LC) without crosswind tide. Fluctuations are partially averaged in time and downstream (x_1) direction.

A constant surface wind stress was applied as previously such that $Re_\tau = 395$ (based on the wind stress friction velocity), acting in a perpendicular direction to the tidal force, and the Langmuir forcing term with parameters $La_t = 0.7$ and $\lambda = 6H = 12\delta$ was present in the governing equation. Zero crosswind shear is applied at the surface. Under this configuration, in the mean, the

109

bottom friction velocity in the downwind direction is equal to the wind stress friction velocity u_τ.

The domain for this test is shown below.
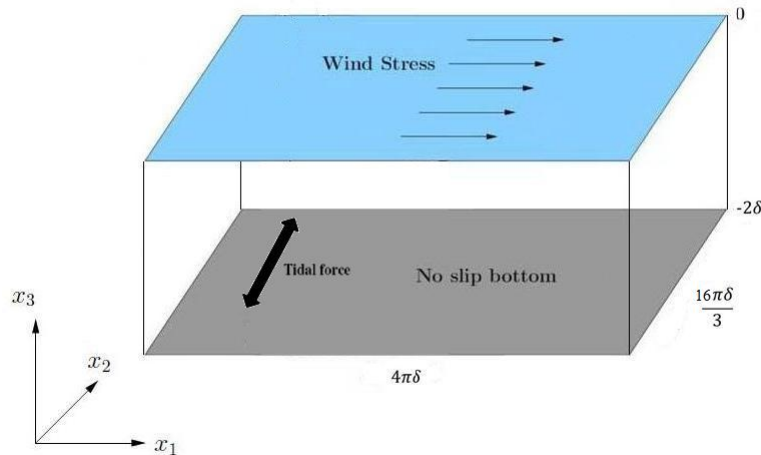
Figure 7.2: Problem domain: Wind, Langmuir and crosswind tidal-driven flow

Consider first the flow behavior under the crosswind tidal force for which a mid-plane velocity ratio of $\frac{u_2^{mid}}{u_1^{mid}} = 1.5$ is achieved (Figure 7.3). When compared to Figure 7.1 above, it is clear to see that the crosswind tidal force is able to almost completely break down the two coherent Langmuir cells observed previously. These coherent supercell structures are replaced with significantly weaker structures, still spanning the full depth of the domain as can be seen in the vertical velocity fluctuations visible in Figure 7.3c, but now significantly thinner in crosswind (x_2) width. Numerous small, weaker structures are observed as opposed to the two large cells present previously. Applying our maximum intensity surface cooling with $Ra_\tau = 5000$ to this same flow, as can be seen in Figure 7.4, appears to have little if any impact on this disruption of the original cells. Results from a case with $Ra_\tau = 211$ were found to be similar (not shown).

110

a) $\langle \bar{u}_1' \rangle_{x_1}/u_\tau$ (Downwind velocity fluctuations)

b) $\langle \bar{u}_2' \rangle_{x_1}/u_\tau$ (Crosswind velocity fluctuations)

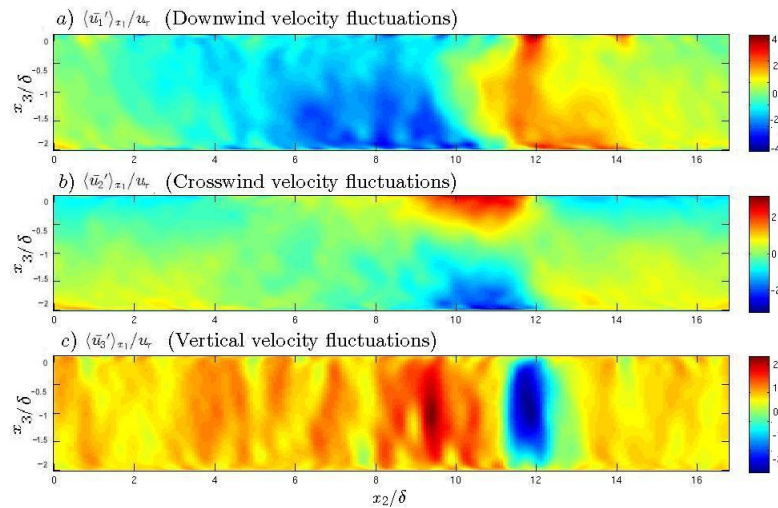c) $\langle \bar{u}_3' \rangle_{x_1}/u_\tau$ (Vertical velocity fluctuations)
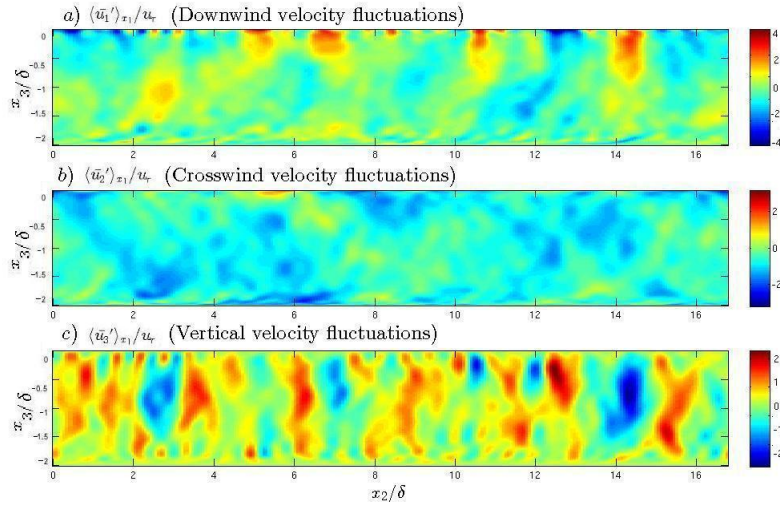
Figure 7.3: Vertical plane colormaps of instantaneous velocity fluctuations: Flow with LC, strong constant crosswind tidal force and no surface cooling ($Ra_\tau = 0$). Fluctuations are partially averaged in the downstream (x_1) direction and scaled with wind stress friction velocity u_τ.

a) $\langle \bar{u}_1' \rangle_{x_1}/u_\tau$ (Downwind velocity fluctuations)

b) $\langle \bar{u}_2' \rangle_{x_1}/u_\tau$ (Crosswind velocity fluctuations)

c) $\langle \bar{u}_3' \rangle_{x_1}/u_\tau$ (Vertical velocity fluctuations)
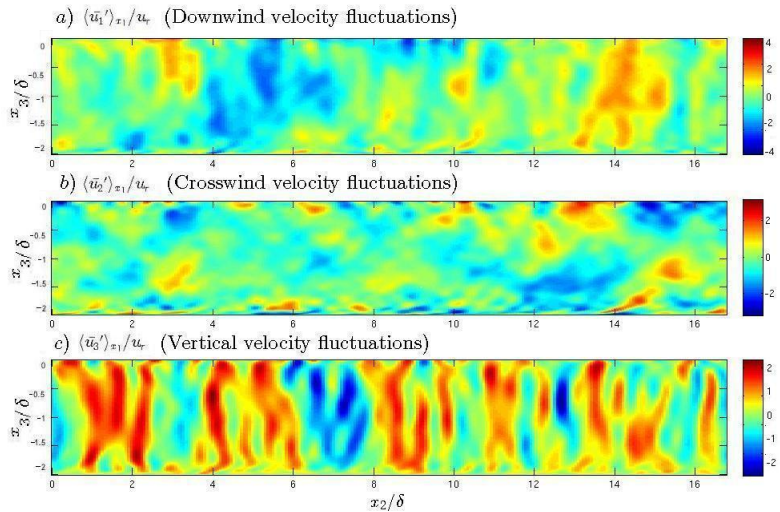
Figure 7.4: Vertical plane colormaps of instantaneous velocity fluctuations: Flow with LC, strong constant crosswind tidal force and surface cooling ($Ra_\tau = 5000$). Fluctuations are partially averaged in the downstream (x_1) direction and scaled with wind stress friction velocity u_τ.

In the case representative of the flow with a weaker crosswind tidal force, the tidal force is applied such that a mid-plane velocity ratio of $\frac{u_2^{mid}}{u_1^{mid}} = 0.5$ is achieved. Figure 7.5 below demonstrates the vertical plane colormaps of velocity fluctuation in this case in the absence of surface cooling.
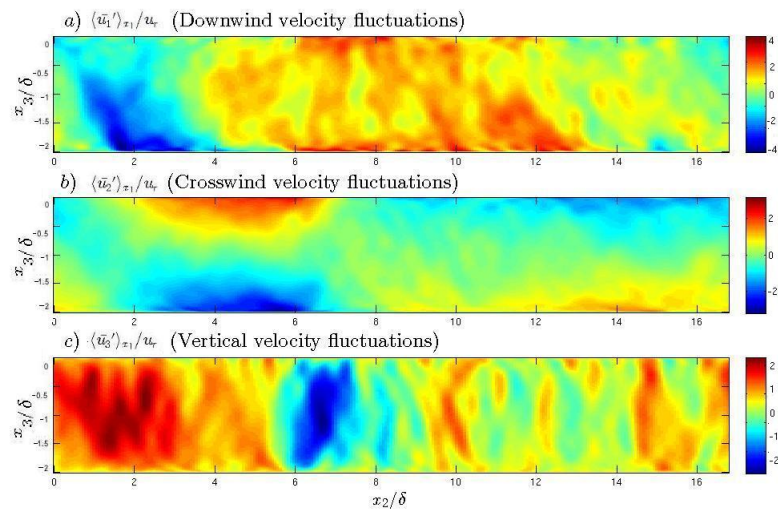
111
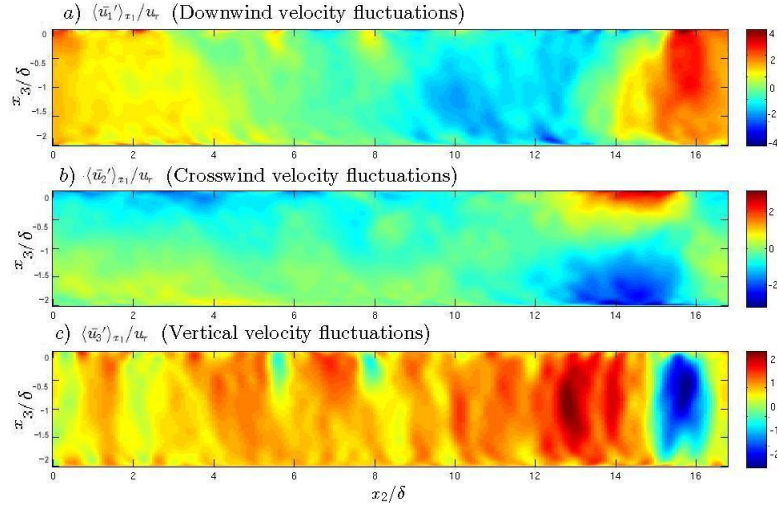
Figure 7.5: Vertical plane colormaps of instantaneous velocity fluctuations: Flow with LC, weak constant crosswind tidal force and no surface cooling ($Ra_\tau = 0$). Fluctuations are partially averaged in the downstream (x_1) direction and scaled with wind stress friction velocity u_τ.

Here, although the original strongly coherent set of two Langmuir supercells is again no longer present, these large turbulent structures do not appear to be broken up by the crosswind forcing in the same manner as with our strong crosswind tidal force. The original cells have both weakened and merged, leaving one less coherent and larger structure surviving, similar to the observations of [11]. When a cooling flux with Rayleigh number of 211 is applied to this flow, very little difference is seen in results (Figure 7.6), however with strong cooling ($Ra_\tau = 5000$) we can see significant strengthening of the single cell (Figure 7.7).

In summary, the implication of the previous results is that when the crosswind tidal forcing is sufficiently strong, Langmuir supercell structures can be broken down into many smaller, weaker full-depth structures, yet at a lower crosswind tidal force large cell structures are able to remain albeit in an altered form: weaker in strength and merged into one, larger cell pair. Further to this, the application of strong surface cooling to this problem setup can lead to stronger structures being

112

maintained despite the crosswind tidal force, larger in crosswind width and with greater fluctuation intensities.

Figure 7.6: Vertical plane colormaps of instantaneous velocity fluctuations: Flow with LC, weak constant crosswind tidal force and no surface cooling ($Ra_\tau = 211$). Fluctuations are partially averaged in the downstream (x_1) direction and scaled with wind stress friction velocity u_τ.

Figure 7.7: Vertical plane colormaps of instantaneous velocity fluctuations: Flow with LC, weak constant crosswind tidal force and no surface cooling ($Ra_\tau = 5000$). Fluctuations are partially averaged in the downstream (x_1) direction and scaled with wind stress friction velocity u_τ.

113

Mean velocity profiles for our cases with a strong tidal force and a weak tidal force further demonstrates the behavior described above. Figure 7.8 shows the full-depth and bottom log layer behavior of the mean velocity for cases with Langmuir forcing only, Langmuir forcing and a strong tidal force with no surface cooling, and this same case with a surface cooling flux at our moderate ($Ra_\tau = 211$) and strong ($Ra_\tau = 5000$) intensities respectively. Note that these figures represent the mean downwind velocity profiles only for comparison to earlier results, analysis of the crosswind mean velocity profiles is omitted for brevity. As expected, in the full water column (Figure 7.8a) the case with Langmuir forcing only demonstrates an S-shaped velocity profile with a homogenized region caused by the strong vertical mixing induced by the cell structures throughout the bulk of the water column. In the case with strong forcing applied (the case with the crosswind to downwind mid-plane velocity ratio of 1.5) this velocity profile demonstrates a positive gradient as the intensity of mixing decreases due to the weakening of the Langmuir cells due to the tide. At a weak surface cooling strength, results are similar. This confirms the cell weakening shown in the vertical plane colormaps above. Notice that when strong surface cooling is applied at a Rayleigh number of 5000, this homogenization again returns to the bulk region of the flow domain, suggesting an increase in turbulent mixing is induced by the surface cooling despite not being visible in the colormaps of velocity fluctuations.

In Figure 7.8 on the right the case with Langmuir circulation demonstrates the typical strong disruption of the expected log law profile. When the crosswind tide is applied this disruption decreases significantly, and the velocity tends closer to a log law. The application of strong cooling to this case leads to the re-establishment of a deviation from a log law.
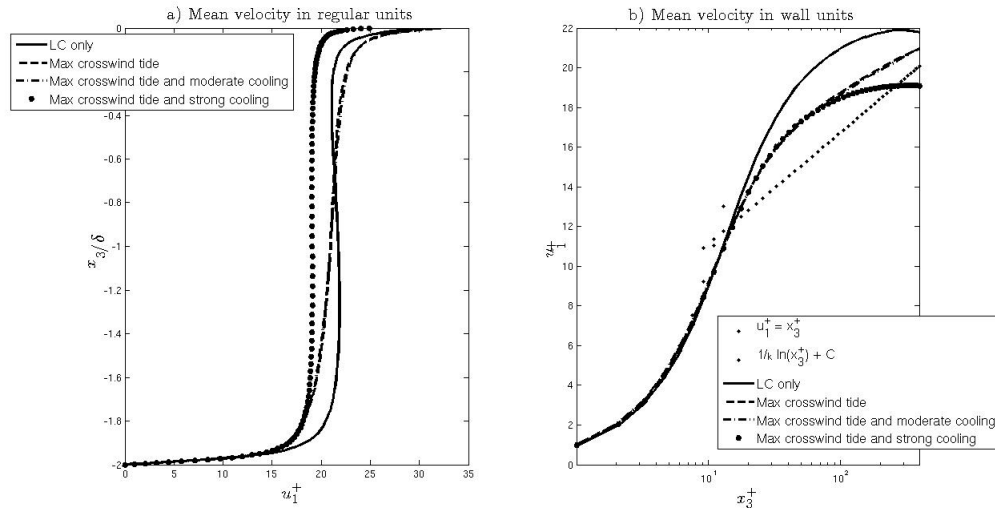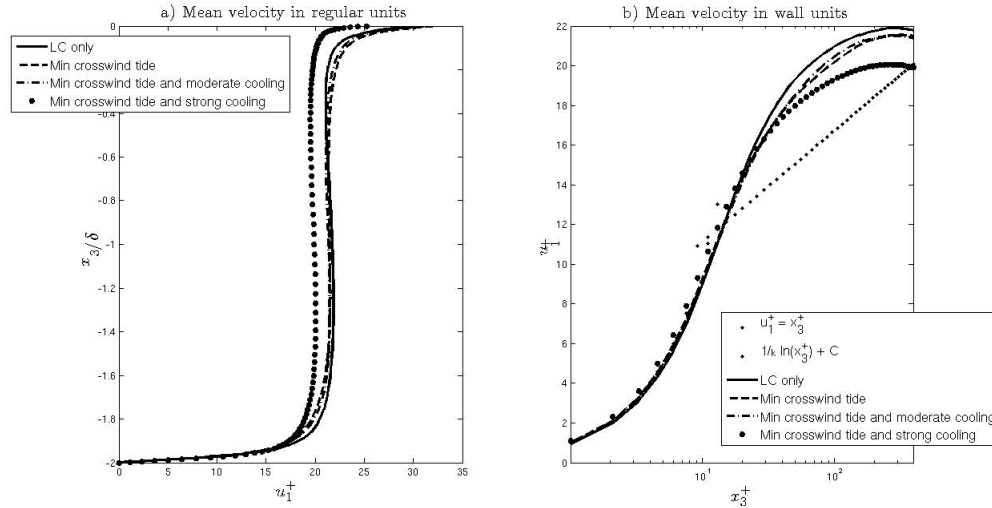
Figure 7.8: Downwind mean velocity profiles: Flows with strong crosswind tide. a) Mean stream-wise velocity profile and b) log law profiles. Velocities are scaled by wind stress friction velocity u_τ.

When the weaker crosswind tidal forcing is applied (the case with crosswind to downwind mid-plane velocity ratio of 0.5), we can see in both panels of Figure 7.9 that the application of the crosswind force does not lead to the same amount of divergence from the Langmuir-only profiles as the previous example. In all cases similar levels of homogenization of the velocity profile throughout the bulk of the water column remain present, and in the log layer the level of disruption associated with the Langmuir turbulence is only slightly reduced. This supports the view that at this lower crosswind tidal force, Langmuir structures are significantly less affected than in the case with the strong crosswind tidal force. In applying a strong cooling flux to this case we see as before that the deviation away from the log law (i.e. the curvature of the mean velocity profile) is enhanced.

115

Figure 7.9: Downwind mean velocity profiles: Flows with weak crosswind tide. a) Mean stream-wise velocity profile and b) log law profiles. Velocities and x_3 in plus units have been defined using wind stress friction velocity u_τ.

RMS profiles of these cases with crosswind tidal forcing demonstrate Langmuir cell weakening. For example, Figure 7.10b shows a decrease in the near-surface crosswind velocity RMS profile in the flow with strong tidal forcing (relative to the flow without tidal forcing) reflecting the weakening of the Langmuir cells near the surface. The opposite trend is observed near the bottom due to the presence of the crosswind mean shear. The presence of the crosswind mean shear also serves to cause homogenization of the vertical RMS of velocity seen in Figure 7.11c. The previous trends are also observed in the flows with weaker tidal crosswind force, but are less pronounced (Figure 7.11). Application of strong cooling enhances the Langmuir cells throughout the water column as seen through the greater RMS of crosswind velocity relative to the other cases (Figures 7.10b and 7.11b).

116
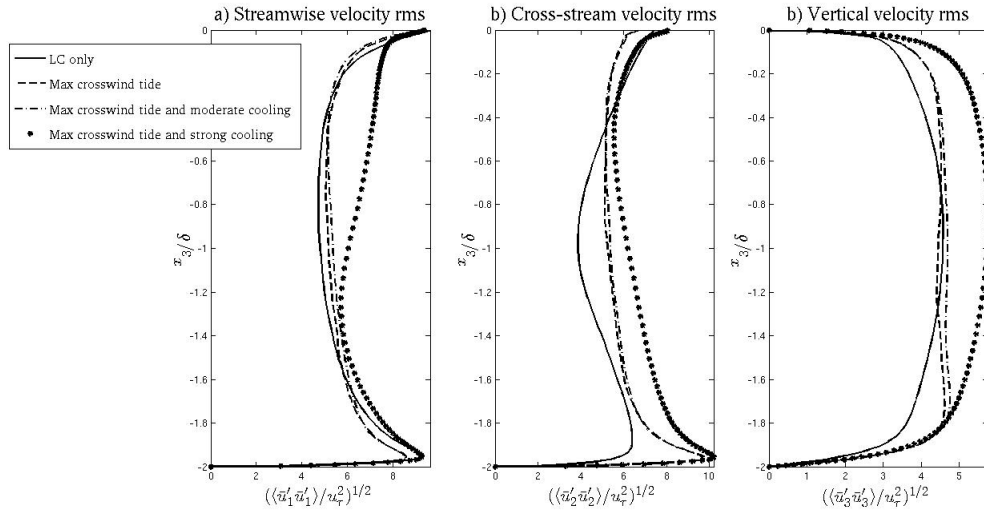
Figure 7.10: RMS of velocity fluctuations: Flows with LC, cooling and strong crosswind tidal force. Fluctuations are scaled by wind stress friction velocity u_τ.
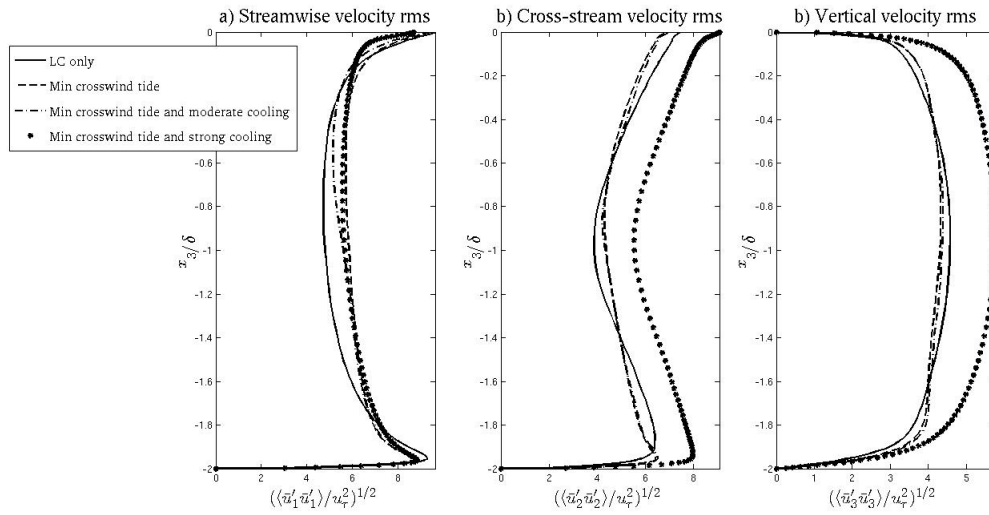
Figure 7.11: RMS of velocity fluctuations: Flows with LC, cooling and weak crosswind tidal force. Fluctuations are scaled by wind stress friction velocity u_τ.

Recall the Lumley invariants described in Chapter 6 and analyzed for our flows with surface cooling and Langmuir circulation only. In order to further assess the process of cell breakdown and, in the weaker crosswind tidal case, the regaining of strength of large-scale structures with a surface cooling flux applied, we can consider similar diagnostics. From a combination of maps

117

of Lumley invariants and a re-plotting of RMS of velocity fluctuations to more clearly show the regions depicted in the Lumley trajectories, we can see how the combination of tidal velocity and a surface temperature flux affect the structure of turbulence.
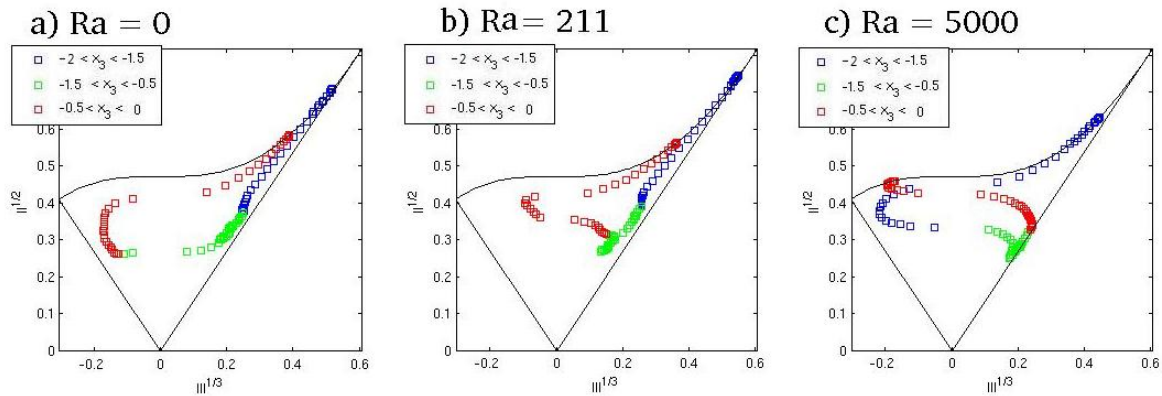
Figure 7.12: Lumley invariants: Flows with strong crosswind tidal force
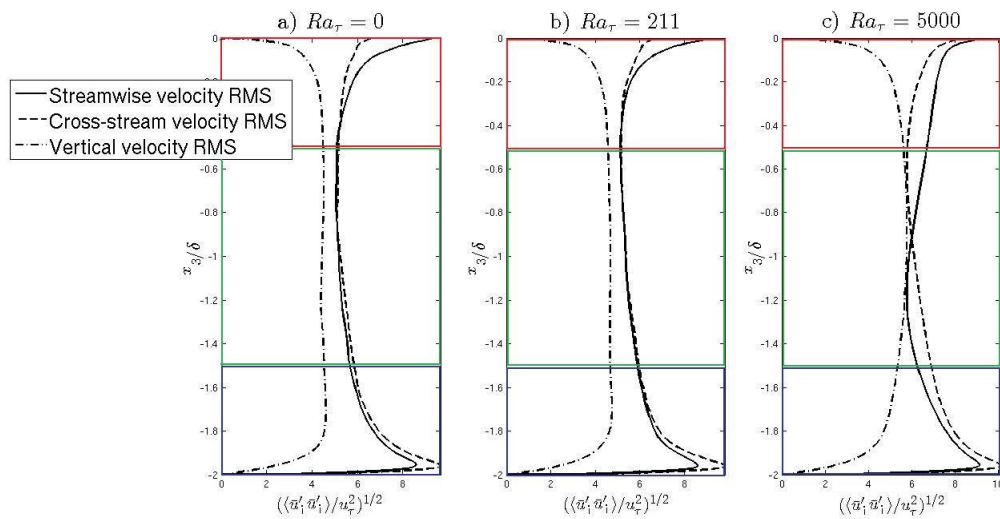
Figure 7.13: RMS of velocity fluctuations in regions identified by Lumley invariants: Flows with strong crosswind tidal forcing

Initially we may consider cases with strong crosswind tidal forcing. In the case with no surface cooling applied and hence just Langmuir forcing and a crosswind tide, a two-component structure is present in the upper $1/4$ of the water column, right at the surface the wind-induced shear leads

118

to a return to one-component turbulence. A similar pattern is visible under the application of a moderate cooling flux ($Ra_\tau = 211$), but under strong surface cooling conditions ($Ra_\tau = 5000$) the slight regaining in strength of Langmuir cells leads to the $< \bar{u}'_2 \bar{u}'_2 >$ now being comparable in magnitude to $< \bar{u}'_1 \bar{u}'_1 >$ and thus two-component turbulence right at the surface.
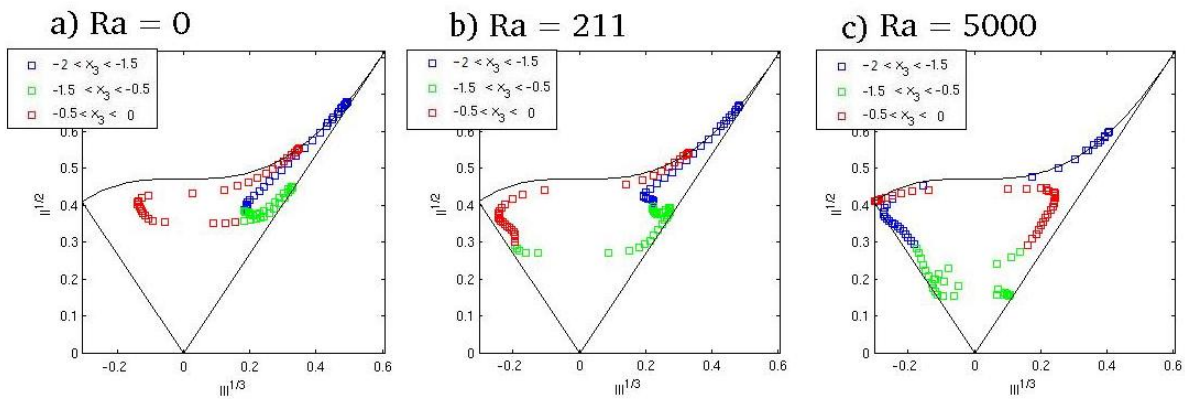
Figure 7.14: Lumley invariants: Flows with weak crosswind tidal force
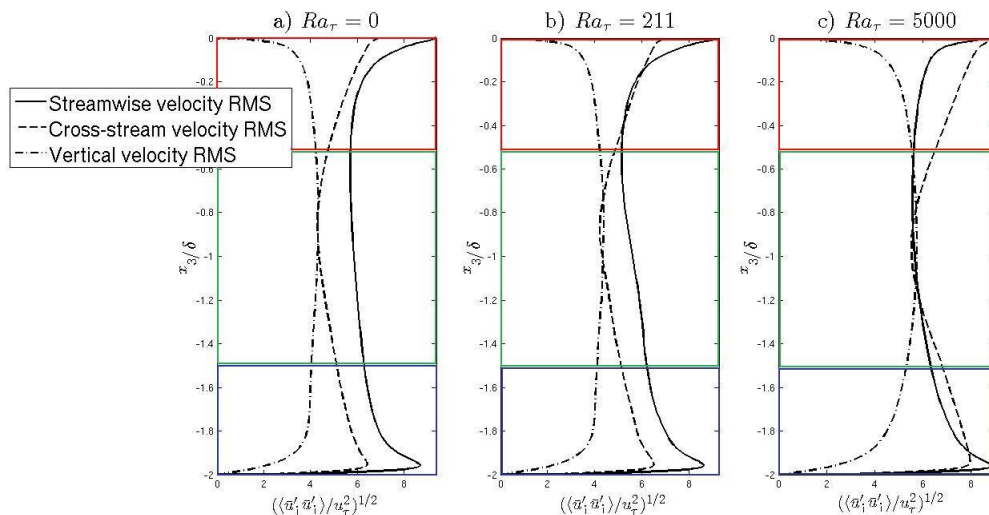
Figure 7.15: RMS of velocity fluctuations in regions identified by Lumley invariants: LC-driven case with minimum crosswind tidal force

In the weak crosswind tidal case, more significant changes are seen as the strength of the surface cooling flux is increased. When the crosswind tide is acting alone on the flow with LC, we can see

119

that the streamwise velocity RMS is the largest component and hence the Lumley depth-trajectory shows a near one-component structure through the bulk of the water column, with the exception of a near-surface region where cross-stream RMS is also significant (potentially due to the weakly remaining Langmuir cell structures visible in the vertical plane colormaps still inducing regions of surface convergence or divergence). As the surface cooling flux increases to the maximum intensity with $Ra_\tau = 5000$, these crosswind velocity fluctuations are seen to increase significantly, overtaking the downstream velocity RMS in the near-surface and near-bottom portions of the water column. This is reflected in the Lumley trajectories where a one-component structure dominates in the bulk of the upper region of the water column, only returning to a two-component structure right at the surface. In the lower half of the water column the intensity of the crosswind RMS component is again large and comparable to the downwind component, leading to a two-component structure throughout much of this region.

From the observations made in the present chapter we can infer that for a strong crosswind tidal force, namely the case in which the crosswind mid-depth mean velocity is approximately 150% of the downwind mid-channel mean velocity, full-depth cellular structures are unable to be maintained. These cells break down into several weaker, narrower structures in which the strong levels of vertical mixing typically associated with the scales of LC are decreased. If, however, this crosswind tidal force is of a lower magnitude, inducing a mid-depth crosswind mean velocity approximately 50% of the downwind velocity, these full-depth Langmuir cells can be found to merge, giving rise to weaker, wider cells than the original structures, in a similar manner to the LES of [11]. Lower intensity mixing is observed, but a wider cell structure remains as opposed to many narrower structures when the crosswind tidal force is at strong intensity. Interestingly,

120

when a strong surface cooling flux is applied to this problem, these cellular structures are able to strengthen, inducing greater vertical mixing.

Chapter 8:

Results: Surface Heating

In large-eddy simulations of stably stratified open channel flow, a stabilizing heat flux has been found to inhibit the development of wall-generated turbulent structures. By imposing a constant heating flux at the channel surface and an adiabatic lower wall, Taylor, Sarkar and Armenio (2005) [29] demonstrated the presence of a stable pycnocline over a well-mixed turbulent region near the lower wall. This pycnocline increased in strength with the increasing of the friction Richardson number (representative of the relative importance of the imposed surface stratification with respect to wall-generated turbulence) and ultimately inhibited the turbulence generated near the bottom no-slip wall. Similar computational tests in which the stable stratification is imposed by a fixed density difference between two solid channel walls, and between a solid lower wall and an upper free-surface, has demonstrated similar inhibitive behavior (Armenio and Sarkar (2002) [3], Nagaosa and Saito (1997) [20], respectively).

As we have established, it has been seen from both field measurements and computational simulations that when a steady surface wind is present, Langmuir circulation can develop in the form of counter-rotating cell pairs aligned with the wind direction, acting secondary to the mean flow. We have seen in Chapter 5 that the application of a surface cooling flux to a flow representative of the shallow coastal ocean can lead to strengthening of the LC structure, and if buoyant forces reached strong enough values they may be able to overtake the Craik-Leibovich vortex (Langmuir)

www.manaraa.com

forcing as the dominant mechanism driving the turbulent motion - although at typical cooling flux values found in shallow coastal oceans convection is unlikely to be this strong.

Based on the knowledge that stable stratification can inhibit turbulence as opposed to strengthening it, the next step in the present series of tests is to use LES to model a shallow coastal ocean with LC under the application of a constant surface heating flux at several strengths represented by a varying Richardson number. Note that for these heating cases we will denote our non-dimensional constant the Richardson number as opposed to the Rayleigh number used for the cooling cases as our emphasis is on stable stratification, but the non-dimensionalization remains the same. Hence, the Richardson number is defined

$$Ri_\tau = \frac{\beta g \delta^2}{u_\tau^2} \frac{Q}{k} \tag{8.1}$$

where now the surface heat flux Q will be positive. As before, u_τ denotes the wind stress: for the flow configuration tested, in the mean, the bottom friction velocity is equal to u_τ. Using a comparison of turbulence statistics as the strength of the heating flux increases with the value of the Richardson number, we can assess not only if the application of stable stratification inhibits the strength of the LC, but also at approximately what values, and to what extent, this occurs.

The flow setup will be identical to the case with LC and cooling in Chapter 6, just with the surface boundary condition representing a positive temperature gradient instead of negative. The domain and mesh size remain the same as before.

As before, we may consider the flow velocity profiles, both over the entire water column and in the bottom boundary region (see Figure 8.1). Note that the spanwise and vertical velocities are nominally zero for this case, as with the cases described in Chapters 4 and 5, as there is no cross-

123

stream forcing mechanism. The streamwise velocity profile is roughly uniform throughout the full depth of the water column in the cases with $Ri_\tau = 0$, $Ri_\tau = 25$ and $Ri_\tau = 100$, due to the high level of vertical mixing induced by the LC (Figure 8.1a). As the Richardson number increases to 500, notice that the majority of the upper half of the water column still shows a near zero-gradient, homogeneous velocity profile despite strong heating intensity. However, in the lower half of the water column, observe that this velocity profile attains a positive gradient similar to that of wind-driven flow without LC and no surface heat flux, suggesting vertical mixing and associated velocity homogenization is no longer reaching full depth.

In the center panel of Figure 8.1 is seen the mean velocity deficit in terms of wall units in the upper half of the water column. The log law profile is indicated in the figure by the thin black line, and represents the behavior of a typical turbulent flow at a wind-driven surface; it is clear to see that a wind-driven case without LC or surface cooling closely follows this expected profile as shown earlier in Chapter 4. In all flows with LC we see the disruption of the classical log-law velocity profile characterizing a traditional turbulent boundary layer. When heating with $Ra_\tau = 500$ is applied this disruption is at a minimum, yet note for future discussion this disruption is still present and significant.

On the right hand side of Figure 8.1 is seen the mean velocity in terms of wall units at the lower wall. The log law profile is again indicated in the upper half of the figure by the narrow black line, and represents the behavior of a typical turbulent flow at a solid bottom wall. The flow in which LC is present without a surface heat flux, or the cases in which the heat flux is low, demonstrate a disruption of the classical log layer profile due to the increased vertical mixing within the water column caused by the LC. When the heating is applied, it is possible to see the flow velocity profile again characterized by the well developed log law profile, indicative of the weakening of

124

the vertical mixing causing the disruption. This suggests that at a Richardson number of 500, the large-scale turbulence is inhibited to a sufficient extent that the flow behavior in the near-wall log layer is similar to a case without LC present.

The interesting thing to note here is that it would seem that at the surface of the channel, although the level of disruption of the boundary layer decreases as the strength of the surface heat flux increases (suggesting some inhibition of the strength of vertical mixing), this level of disruption is still significant and implies that some secondary turbulent structure may still be present. On the contrary, at the bottom of the water column, these mean velocity profiles would suggest that the Langmuir-induced turbulence has been almost completely diminished, as the flow behavior in the bottom log region is almost identical to that in a wind-driven flow without Langmuir forcing. The implication here is that perhaps the application of a stable density gradient through surface heating is able to limit the depth to which large-scale Langmuir supercells are able to penetrate within the water column.
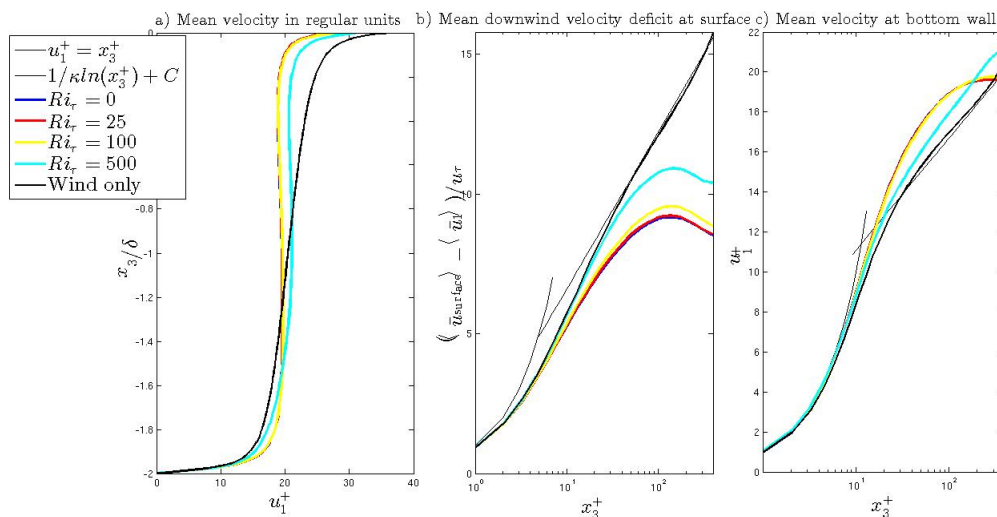
Figure 8.1: Velocity profiles: Flows with LC and surface heating. a) Mean streamwise velocity profile as a function of depth, b) Mean streamwise velocity deficit in wall units at upper surface and c) Mean streamwise velocity in wall units at lower wall. The wind-only case corresponds to wind-driven flow without LC and no surface heat flux.

125

We can consider the mean temperature profile throughout the water column, and also the temperature flux in the same region for each of the values of the Richardson number simulated (see Figure 8.2). As the surface heat flux increases, the thickness of the surface temperature boundary layer correspondingly increases, with the region of high temperature gradient extending to a greater depth from the surface. Considering the case with maximum heating, we can see in this temperature profile that the temperature is approximately constant in the majority of the upper half of the water column (outside the temperature boundary layer region), again due to the mixing of LC. However, a significant positive gradient is present throughout the lower half of the column. Thus, a stable temperature stratification is prevalent here. When the Richardson number is non-zero, little difference is seen in the vertical turbulent temperature flux, although in the bulk of the domain the flux is slightly lower in magnitude for the cases with $Ri_\tau > 0$, indicative of turbulence supression by the surface heating.
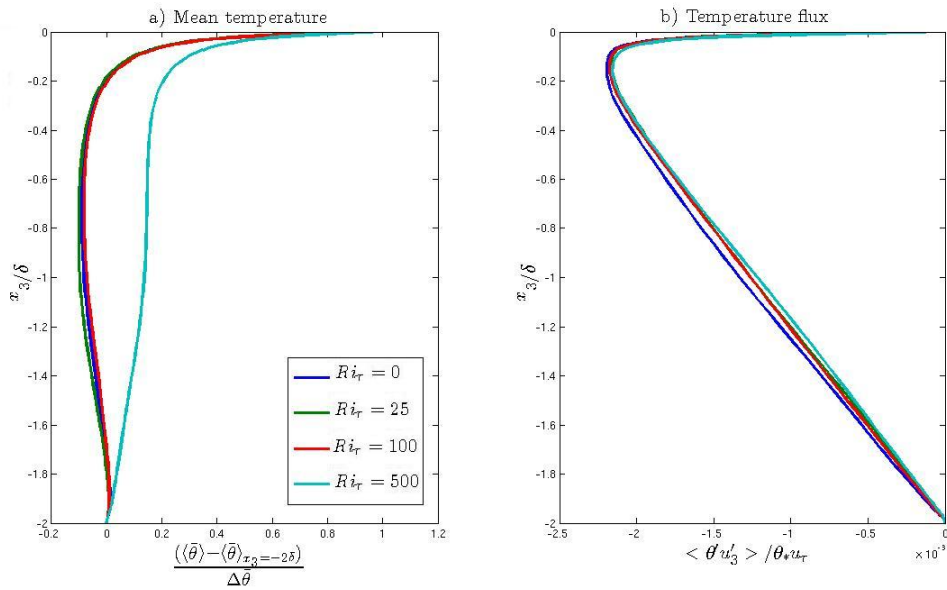
Figure 8.2: Temperature profiles: Flows with LC and surface heating. a) Mean temperature and b) vertical turbulent heat flux throughout full water column depth. Note that $\Delta\bar{\theta} = \langle\bar{\theta}\rangle_{x_3=0} - \langle\bar{\theta}\rangle_{x_3=-2\delta}$.

126

Additionally, we can consider the temperature gradients throughout the water column. The zoomed-in region of Figure 8.3 highlights the deepening of the surface temperature boundary layer as the strength of surface heating increases; in the LC-only case, the flow reaches a fully homogenous temperature profile at shallower depths than with heating applied, as would be expected. In the lower region, we can see the temperature gradient is significantly larger with $Ri_\tau = 500$, as would be expected given the stably stratified gradients visible in the above velocity and temperature profiles.
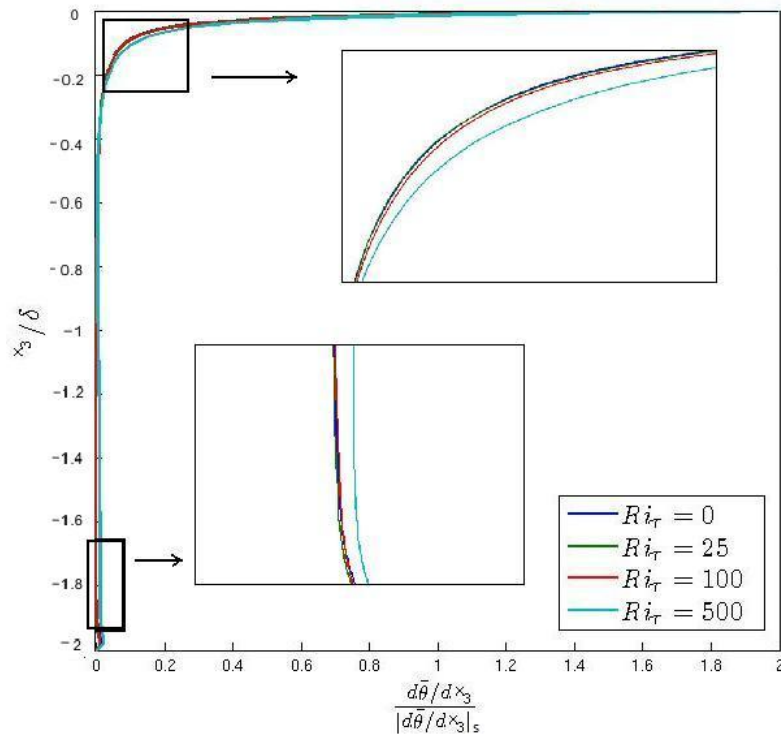
Figure 8.3: Temperature gradients: Flows with LC and surface heating

We may consider velocity fluctuations across vertical planes of the domain in order to see more clearly the impact of an increasing Richardson number on the large scale turbulent structures acting as a secondary component to the mean flow. Again, we average instantaneous velocity fluctuations over the streamwise direction and time and plot these averaged fluctuations in the vertical

127

and cross-stream directions. As previously, the flow with zero surface heat flux demonstrates the presence of full-depth regions of negative and positive vertical velocity fluctuations representing the downwelling and upwelling limbs of the resolved Langmuir cell (Figure 8.4b). The crosswind velocity fluctuations are characterized by negative and positive zones representing the surface and bottom convergences of the LC (Figure 8.4c). In the cases with $Ri_\tau = 100$ (Figure 8.5), little difference is seen to the case without surface heating, but as the Richardson number increases to $Ri_\tau = 500$ (Figure 8.6) we can clearly see from the vertical plane colormap the intensity of the cellular structures is diminished in the lower half of the water column, but remains relatively strong near the surface. The turbulence has been significantly inhibited near the lower wall. This supports the implication made through previous analysis of the mean velocity profiles in the upper and lower boundary layers that the application of stable stratification by surface heating is able to limit the depth to which full-depth LC are able to penetrate and generate strong mixing.
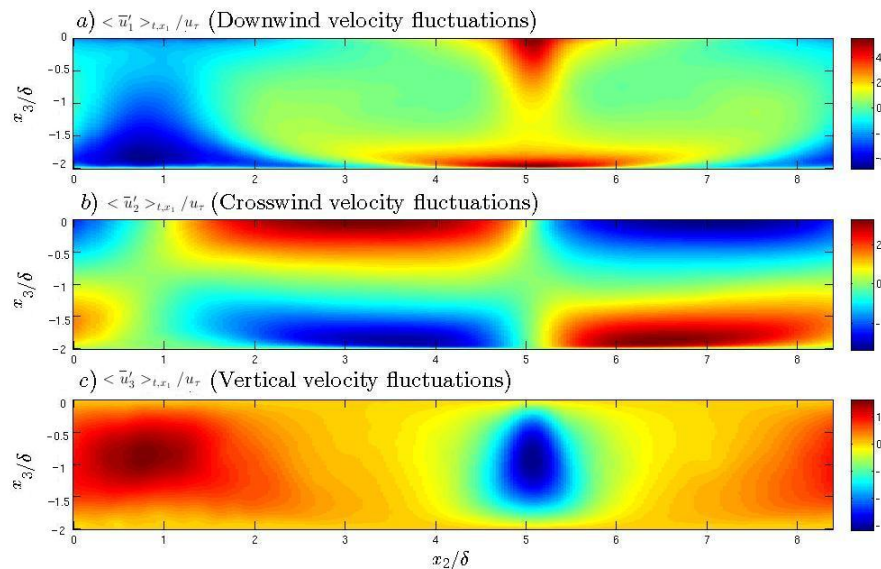
Figure 8.4: Vertical plane colormaps of velocity fluctuations: Flow with LC and no surface heating $(Ri_\tau = 0)$. Fluctuations are partially averaged in time and the downstream (x_1) direction.

128
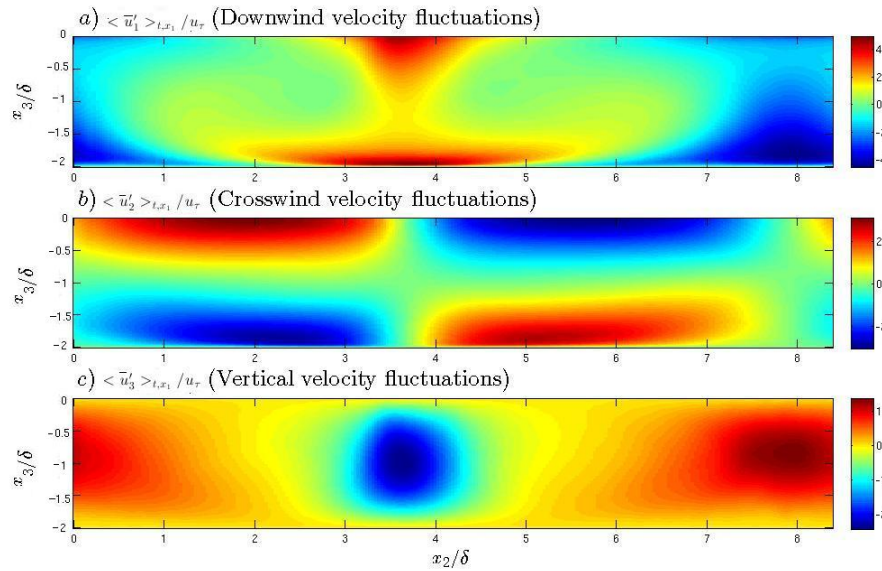
Figure 8.5: Vertical plane colormaps of velocity fluctuations: Flow with LC and surface heating ($Ri_\tau = 100$). Fluctuations are partially averaged in time and the downstream (x_1) direction
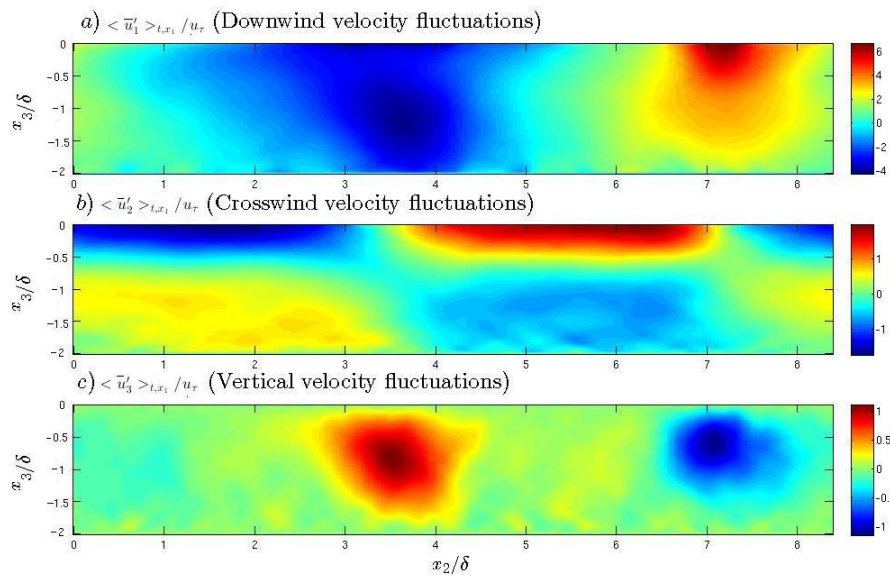
Figure 8.6: Vertical plane colormaps of velocity fluctuations: Flow with LC and surface heating ($Ri_\tau = 500$). Fluctuations are partially averaged in time and the downstream (x_1) direction

Returning to profiles of the RMS of velocity fluctuations (Figure 8.7), in the horizontal directions (streamwise and cross-stream), the influence of the surface heat flux at a Richardson number

129

of 500 is substantial. The streamwise RMS velocity increases with the Richardson number, consistent with the increase of mean shear caused by the surface heating. In the lower wall region at $Ri_\tau = 500$, the stable stratification is seen to suppress the crosswind RMS consistent with the weakening of the bottom divergence zone of the LC seen in Figure 8.6b relative to the $Ri_\tau = 0$ case in Figure 8.4b. However, in the case with $Ri_\tau = 500$, at the surface the characteristic patterns of persistent Langmuir cell structures are still present. Most noticably the increase in the crosswind RMS relative to the middle of the water column corresponding to the presence of strong surface convergence and divergence zones of the LC is still present, albeit at a lower magnitude.
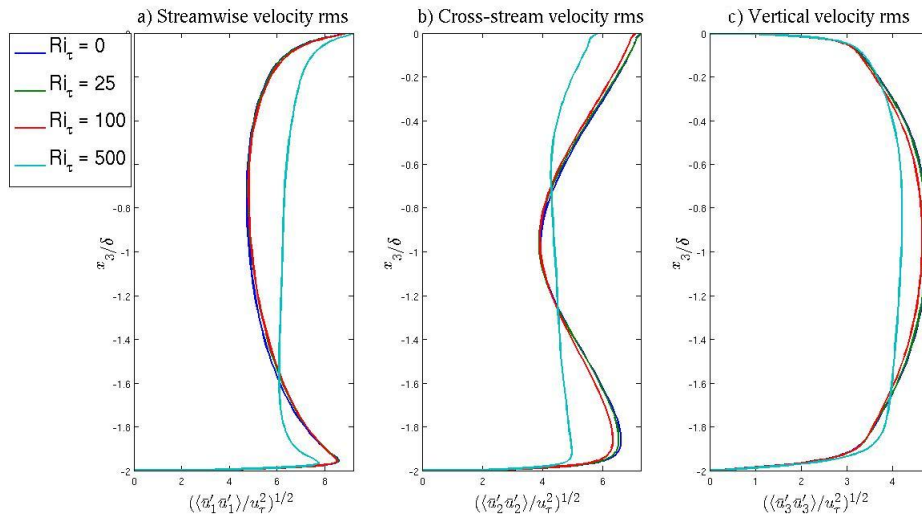
Figure 8.7: RMS of velocity fluctuations: Flow with LC and surface heating

Similarly in the profiles in Figure 8.7, at a Richardson number of 500 it is possible to see a substantial decrease in the vertical velocity RMS. Again, as the surface heat flux inhibits the strength and coherence of the Langmuir cells, the regions of strong up- and down-welling in the middle of the water column become weaker.
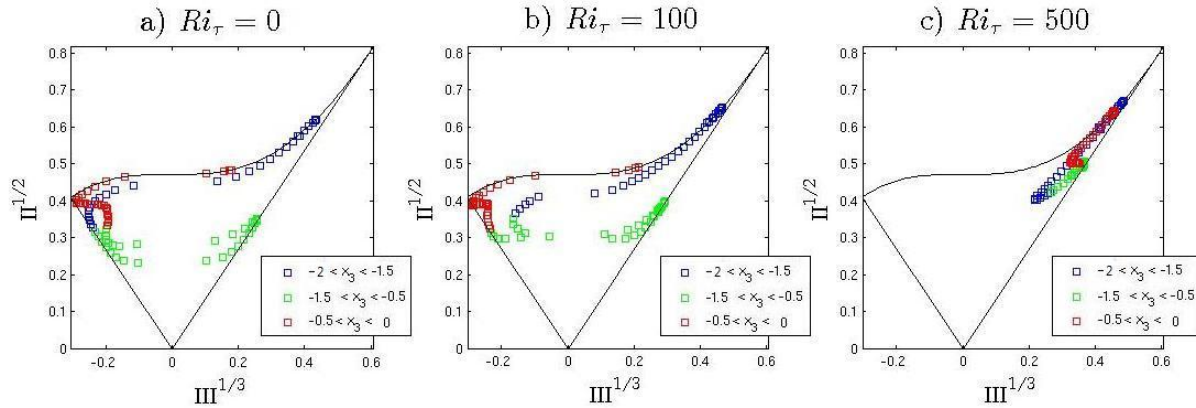
Figure 8.8: Lumley invariants: Flow with LC and surface heating
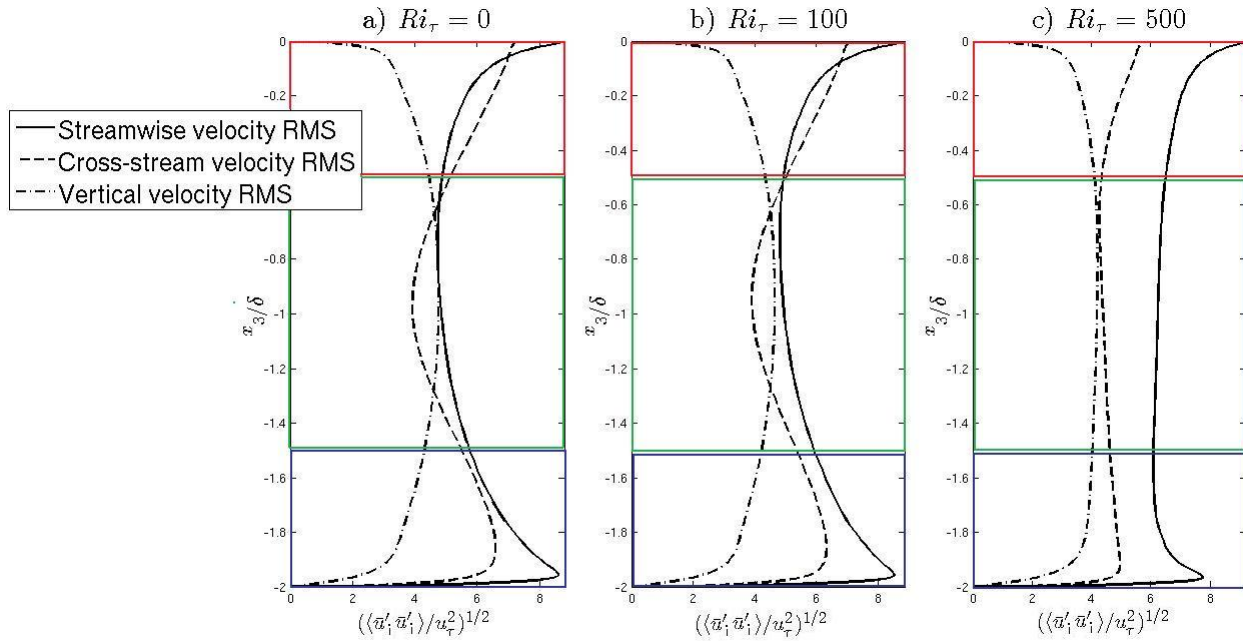
Figure 8.9: RMS of velocity fluctuations in regions identified by Lumley invariants: Flow with LC and surface heating

We may return to a consideration of Lumley invariants as discussed in Chapter 7, now for our cases with a surface heat flux applied. Recall in the case without a surface heat flux the regions of cross-stream velocity convergence and divergence associated with the Langmuir supercell and the shear generated by no-slip at the lower wall and the wind stress at the surface lead to a two-

131

component structure in the near-surface and near-wall regions of the water column in which both $<\bar{u}'_1\bar{u}'_1>$ and $<\bar{u}'_2\bar{u}'_2>$ are significantly larger than $<\bar{u}'_3\bar{u}'_3>$ (Figure 8.8a). In the case with surface heating applied in Figure 8.8c, it can be seen that at a Richardson number of 500, throughout the whole depth of the water column the turbulence retains a one-component structure as $<\bar{u}'_1\bar{u}'_1>$ dominates throughout, typical of a purely shear-dominated flow. This suggests the cells leading to the two-component structure in the case with LC without surface heating have been diminished. This can clearly be seen in the RMS profiles in Figure 8.9.

Additionally we can consider the total turbulent kinetic energy throughout the full depth of the water column. In the cases with $Ri_\tau = 0$ and $Ri_\tau = 100$, shown in Figure 8.10, we can observe higher levels of turbulent kinetic energy in the upper and lower halves of the water column relative to the middle of the water column. This corresponds to the strong surface and bottom convergence and divergence zones of the resolved LC (visible in Figures 8.4b and 8.5b) and the high values of crosswind RMS in the near-surface and near-bottom regions (Figures 8.9a,b) relative to the middle of the water column for the $Ri_\tau = 0, 100$ cases. When the strong surface heating is applied, this structure remains in the upper half of the water column in terms of the TKE in Figure 8.10, but we can observe homogeneity in the lower half where the LC is suppressed.

132
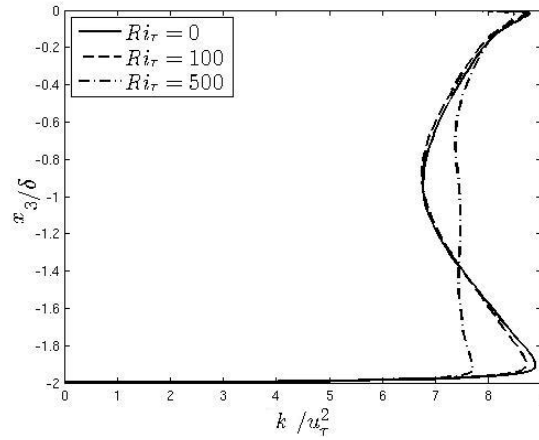
Figure 8.10: Turbulent kinetic energy $k = < \bar{u}_i' \bar{u}_i'/2 >$: Flow with LC and surface heating
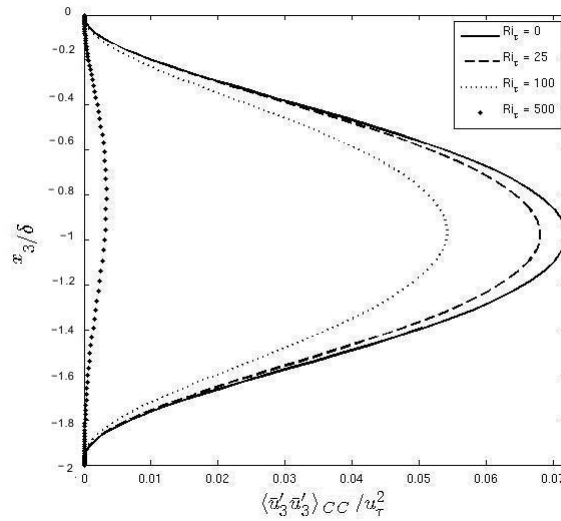
Figure 8.11: Instantaneous vertical velocity variance for varying values of Ri_τ: Flow with LC and surface heating

Figure 8.11 demonstrates the respective contributions of full-depth Langmuir cells to the vertical velocity RMS previously analyzed for increasing values of the Richardson number. Notice that here we have applied "CC" notation as we are monitoring the contribution of full-depth coherent Langmuir cell structures using the decomposition presented in Chapter 5. From here we can see the dramatic effect of the surface heating flux on the strength of the vertical velocity fluctuations

133

present in the cellular structures. Notice that as Ri_τ increases, corresponding to an increase in the surface heating, the vertical velocity fluctuations associated with the large Langmuir cells are diminished significantly. By $Ri_\tau = 500$, the strength (i.e. the contribution) of the Langmuir cell is significantly diminished.

Next we can consider the budgets of turbulent kinetic energy in both the surface and bottom halves of the water column for the respective cases with no surface heat flux and hence LC only and the cases with LC and surface heating with $Ri_\tau = 100$, and with $Ri_\tau = 500$. In Figure 8.12, in the near-surface region of the water column it is possible to see that only limited changes occur as surface heating is applied: relative to the flows with $Ri_\tau = 0, 100$, the flow with $Ri_\tau = 500$ is characterized by higher production by mean shear which is compensated for by buoyancy and turbulent transport sinks. In Figure 8.13, near the bottom of the water column, again differences are limited, but we can observe that turbulent transport becomes less significant, while SGS dissipation becomes more important.
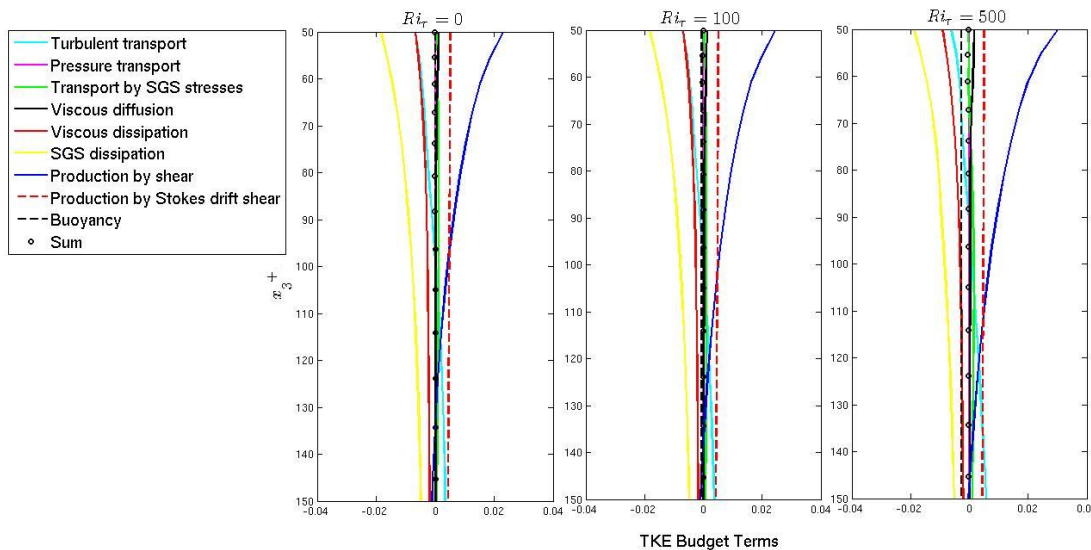
Figure 8.12: Budgets of turbulent kinetic energy in near-surface region: Flow with LC and surface heating. Ranges shown are $50 \leq x_3^+ \leq 150$ from the surface. Budget terms are scaled by u_τ^2.

134
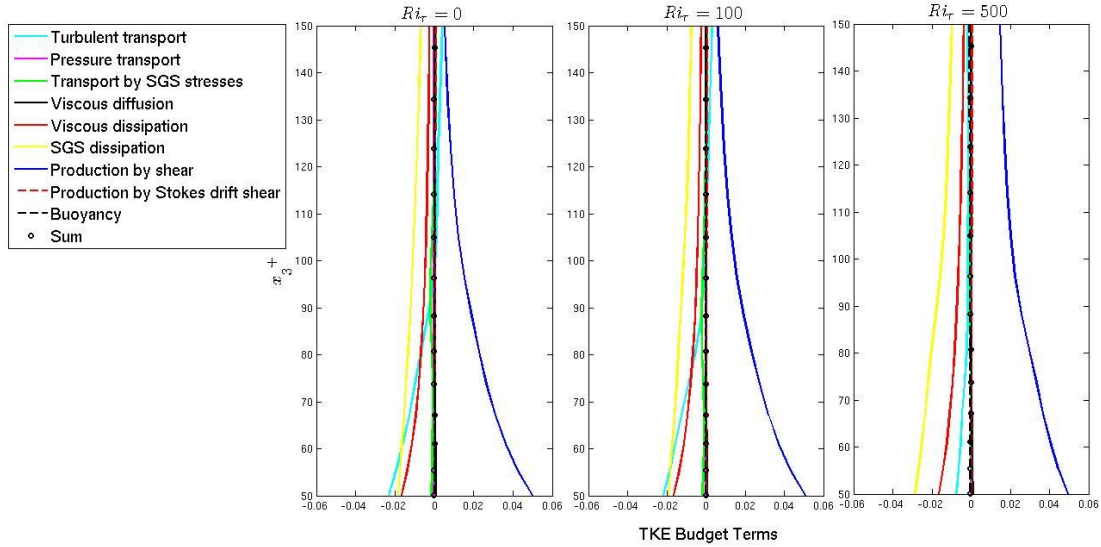
Figure 8.13: Budgets of turbulent kinetic energy in near-bottom region: Flow with LC and surface heating. Ranges shown are $50 \leq x_3^+ \leq 150$ from the bottom. Budget terms are scaled by u_τ^2.

Earlier results presented in this chapter have demonstrated inhibition of cellular structures caused by the application of surface heating which affects a substantial portion of the water column, as opposed to just the surface and lower wall regions. Figure 8.14 demonstrates the budgets of turbulent kinetic energy for the region in the bulk of the water column ($-1.8 < x_3/\delta < -0.2$, corresponding to approximately $100 < x_3^+ < 690$ from the lower wall). Here, the most significant differences between the flows with and without the application of a surface heating flux can be observed. For clarity, Figure 8.15 highlights only the terms of Figure 8.14 that show significant differences with and without the heating flux, namely the turbulent transport and production by mean shear, and also emphasises the sum of terms which lies at approximately zero and the contributions from buoyancy (from heating) and Stokes-drift shear (from LC).

135
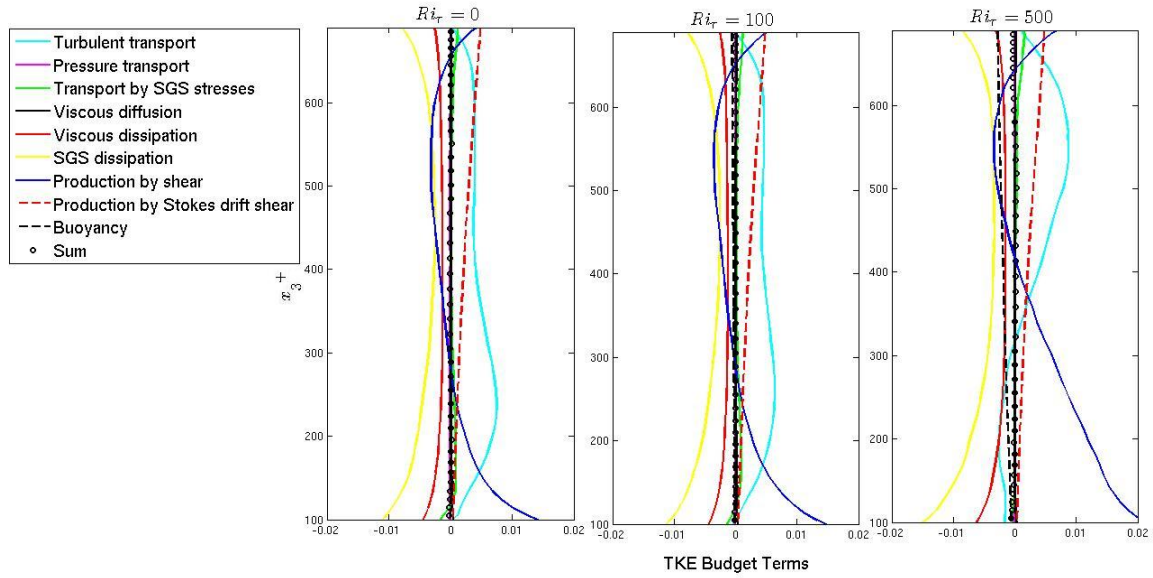
Figure 8.14: Budgets of turbulent kinetic energy in bulk of water column: Flow with LC and surface heating. Note figure excludes high gradient surface and lower wall regions. Budget terms are scaled by u_τ^2.
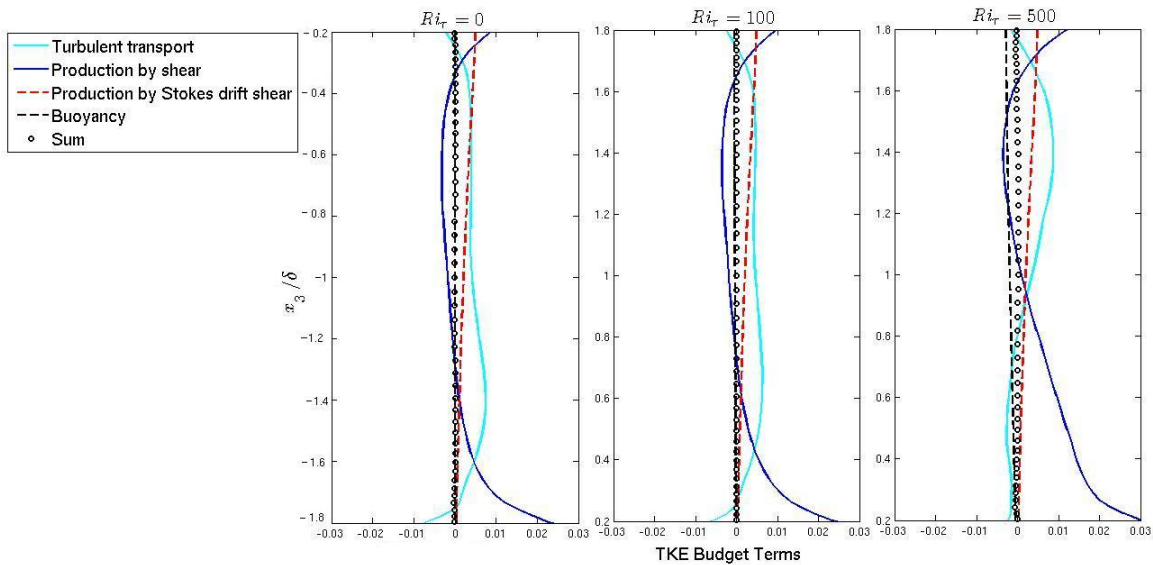
Figure 8.15: Adaptation of budgets of turbulent kinetic energy (LC-driven case with heating) in bulk of water column. Figure demonstrates contributions of turbulent transport, production by mean shear, buoyancy and Stokes-drift shear

136

The most noteworthy observation to be made from Figure 8.15 is the difference in distribution of turbulent transport. In the center and left hand side panels showing the $Ri_\tau = 0$ and $Ri_\tau = 100$ cases, we may observe that the turbulent transport remains a substantial source throughout the bulk of the water column, indicative of the presence of the large turbulent structure leading to vertical mixing and homogenization of flow properties. Turbulent transport is the largest source of TKE in the bulk of the water column except when production by mean shear becomes significant close to the solid lower wall (due to the no-slip condition) and the surface (due to the wind stress). When the surface heating flux is applied with $Ri_\tau = 500$, we can see a shift in the positive contribution of turbulent transport to the upper half of the water column, with very little turbulent transport in the lower region. This, paired with the significant increase in the production of turbulent kinetic energy by mean shear in this lower half of the domain, is yet further evidence that the application of the surface heat flux appears to be inhibiting the depth of LC.

To summarize, the application of surface heating leads to depth-inhibition of pre-existing, full-depth Langmuir cell structures. The interesting thing to note here is the location of this turbulence suppression. At the surface we do see some weakening of the turbulent mixing induced by the Langmuir cells reflected, for example, through the thickening of the surface boundary layers and hence increase in distance from the upper surface of the start of the homogeneous (strongly mixed) region. However, overall the bulk of the upper half of the water column still demonstrates homogenization of flow properties suggesting the strong vertical mixing induced by the Langmuir structure is still present. In the lower half of the water column when the surface heating at $Ri_\tau = 500$ is applied, we can see a weakening of mixing and the presence of a stably stratified temperature profile. The slight weakening of the strength of LC at the surface due to the surface heating leads to down-

137

welling limbs of the LC which are insufficiently strong to generate mixing in the near-wall region and thus allow a stratified pycnocline region to develop in the lower half of the water column.

From Figure 8.15 for the flow with $Ri_\tau = 500$, we could observe that the main source of turbulent kinetic energy transitioned from turbulent transport (near the surface) to production by shear (near the bottom) at approximately the mid-depth of the water column, suggesting that at the current ratio of Langmuir forcing to surface heating, the stratification-affected lower region accounts for approximately 50% of the flow domain. In potential future testing, a wider range of cases could be considered to attempt to identify a clear relationship between the ratio of Langmuir forcing to turbulent Richardson number and the depth of turbulence inhibition.

Chapter 9:

Discussion and Conclusions

In this dissertation the impact of several combinations of environmental forcing mechanisms on large (full-depth) turbulent structures in a flow representative of a shallow coastal ocean have been considered. This includes both downwind and crosswind tidal forces, surface wind stresses, Langmuir forcing caused by the interaction of wind and surface gravity waves, and a range of intensities of both stabilizing and de-stabilizing surface heat fluxes. The findings of the LES tests in the present dissertation have contributed towards the bridging of existing gaps in knowledge on how wind, wave, tidal and surface buoyancy forcing mechanisms act both in isolation and in conjunction with others in determining the turbulence structure throughout the water column. This gain in knowledge has broad impacts as turbulent vertical mixing can have major effects on coastal processes including ecosystem functioning, surface gas exchange, sediment resuspension and contaminant dispersion.

The emphasis of the present work was on the behavior of *large* structures, namely those which feature turbulent motions which are persistent in time, secondary to the mean flow and can entrain fluid on scales of the order of the flow domain. Three preliminary problem setups were defined in which such structures can be observed. A constant pressure gradient-driven flow with a no-slip lower wall and a shear-free upper surface demonstrates the development of coherent roll cell structures, elongated downstream and similar to those found in a plane Couette flow in [21] and [13], as well as in flow driven solely by a surface wind stress. The application of the well-known

139

Craik-Leibovich forcing mechanism, representative of the interaction of the Stokes-drift velocity (induced by surface gravity waves) and the wind-driven shear current, to a wind-driven flow (in the absence of a tidal pressure gradient) also leads to large structures similar to Couette cells, this time significantly stronger and more coherent, in the form of Langmuir cells. Langmuir cells also exist in the form of counter-rotating, elongated cell pairs. The cells have been observed in both the upper ocean mixed layer and, more recently in [8], a fully-mixed shallow coastal shelf region. The previously described fundamental problems and the behavior of their respective large (full-depth) turbulent structures under the influence of external forces provided the basis for the tests in this dissertation.

Initially in Chapter 5 it was observed that the application of a surface cooling flux to a flow featuring a constant downstream tidal force or pressure gradient is able to generate convection "supercells", spanning the full depth of the domain and generating strong vertical mixing. These cellular structures show very similar behavior to the full-depth Langmuir supercells observed in [8] and simulated in LES studies in [30], despite the difference in forcing mechanism. Similar observations were made for a flow driven by a surface wind with surface cooling but in the absence of the wave (Craik-Leibovich vortex) forcing that generates the Langmuir cells; existing weak, Couette-like cells merge and strengthen to form one convective supercell.

Based on the findings of the previously described flows without Langmuir cells, the second aim of the present dissertation was to determine whether surface cooling fluxes in the ocean environment are able to augment or alter pre-existing large turbulent structures such as Langmuir cells. Rayleigh numbers representative of the surface buoyancy to shear were considered ranging from $Ra_\tau = 0$ (no surface cooling flux), $Ra_\tau = 211$ (a moderate surface cooling flux, typical of observations in the field) and $Ra_\tau = 5000$ (a strong surface cooling flux). It was found that when a strong

140

surface cooling flux characterized by $Ra_\tau = 5000$ is applied to a case with pre-existing Langmuir circulation, although the supercell remains consistent in terms of cross-stream width and structure, analysis of turbulence statistics suggests the surface cooling can significantly increase the strength and coherence of the cell. However, at realistic values of a surface cooling flux that may commonly be observed in the field, this augmentation of these cells is not significant enough to allow convection to take over from Langmuir forcing as the dominant mechanism in cell generation, and Langmuir forcing remains the main source of turbulent kinetic energy involved in cell generation and maintenance. Comparison of the the present LES of turbulence in shallow water to existing LES studies of the upper ocean mixed layer and field measurements in shallow water ([26], [8]) supported this observation. Contributions of Langmuir forcing (through Stokes drift shear) and convective buoyancy respectively to turbulent kinetic energy were then analysed and suggested that for convective forcing to become the dominant source of energy over Langmuir forcing, a turbulent heat flux at the surface approximately five times greater than the moderate flux typically observed ($200W/m^2$) would be required.

In Chapter 7 a crosswind tidal force was taken into account in our LES studies. It was observed that a crosswind tidal force or pressure gradient leading to a crosswind-to-downwind mid-depth velocity ratio of approximately 1.5 led to the breakdown of full-depth Langmuir cells into several weaker structures, still full-depth but significantly reduced in cross-stream width. The resulting structures were seen to induce less vertical mixing than the Langmuir supercells present in the absence of the crosswind tidal forcing. When the crosswind tidal force produces a smaller crosswind mid-depth velocity component than the one present at mid-depth in the downwind direction, Langmuir cells merge into one wider but less coherent cell. When a surface cooling flux contributes to

141

this problem setup along with crosswind tidal forcing, cellular structures are able to gain strength from the convective forcing leading to enhanced vertical mixing.

Furthermore, Chapter 8 demonstrated that the imposition of a surface heat flux is able to inhibit the depth to which Langmuir supercells and the corresponding vertical mixing they induce are able to homogenize flow properties. In a surface heating case featuring a Richardson number of 500, a pre-existing Langmuir supercell is only able to maintain strength and cause significant vertical mixing in the upper half of the water column. Below this, in the lower half of the water column where the intensity of surface mixing mechanisms imposed by wind stress and Langmuir forcing are diminished, a stably stratified temperature profile is visible suggesting the formation of a heating-induced pycnocline separated from the heat source (i.e. the surface) by a mixed region generated by Langmuir forcing.

Due to the time and cost involved in collecting field measurements and the complexities of real world environmental flows making laboratory experiments challenging, it is hoped the ob-servations made through LES may contribute to both the future interpretation of field data and to models of both the ocean and the global climate which require accurate parameterization of the behavior of turbulence structures which can induce strong vertical mixing under a variety of environmental forcing conditions. There remains significant scope for further research. Other combinations of parameters including the turbulent Langmuir number and the wavelength of the surface waves (generating the Langmuir cells) should be assessed for their impact on the afore-mentioned transition point from Langmuir-driven to convection-driven turbulence; perhaps with a lower intensity of Langmuir forcing the surface cooling flux required for this transition may fall within a realistic range. Additionally, a formal parameter for the relationship between the strength of surface-induced turbulence and the surface heating flux could be identified to allow ease of as-

sessment of the depth to which cellular structures may be able to penetrate without being inhibited by a temperature gradient. In due course, future field data may be able to provide validation for these parameters.

References

[1] Akan, C., 2012. Surface Mass Transfer in Large Eddy Simulation (LES) of Langmuir Turbulence. PhD thesis, University of South Florida, Tampa.

[2] Akan, C., Tejada-Martinez, A.E., Grosch, C.E., Martinat, G., 2013 Scalar transport in large-eddy simulation of Langmuir turbulence in shallow water. Cont. Shelf Res. 55, 1-16

[3] Armenio, V., Sarkar, S., 2002. An investigation of stably stratified turbulent channel flow using large-eddy simulation. J. Fluid Mech. 459, 1-42

[4] Bammou, L., Omari, E.K., Blancher, S., Le Guer, Y., Benhamou, B. et al., 2012. A numerical study of the longitudinal thermoconvective rolls in a mixed convection flow in a horizontal channel with a free surface.

[5] Craik, A.D.D., Leibovich, S., 1976. A rational model for Langmuir circulations. J. Fluid Mech. 73:401-26

[6] Franzini, J.B., Finnemore, J.E., Daugherty, R.L., 1997. Fluid mechanics with engineering applications. McGraw-Hill.

[7] O.B. Fringer, S.W. Armfield, and R. L. Street. A nonstaggered curvilinear grid pressure correction method applied to interfacial waves. In 2nd International Conference on Heat Transfer, Fluid Mechanics, and Thermodynamics (HEFAT), page FO1, Victoria Falls, Zambia, 2003.

[8] Gargett, A., Wells, J., Tejada-Martínez, A.E., Grosch, C.E., 2004. Langmuir supercells: a dominant mechanism for sediment resuspension and transport in shallow shelf seas. Science. 306, 1925-1928

[9] Germano, M., Piomelli, U., Moin, P., Cabot, W. H., 1991. A Dynamic Subgrid-Scale Eddy Viscosity Model. Phys. Fluids. 3(7), 1760-1765

[10] Kolmogorov, A.N. 1941 Dissipation of Energy in a Locally Isotropic Turbulence (Dokl. Akad. Nauk SSSR 32: 141) Proc. R. Soc. London A 434, 15-18, 1991 (English translation).

[11] Kukulka, T., Plueddemann, A.J., Trowbridge, J.H., Sullivan, P.P., 2011. The influence of cross-wind tidal currents on Langmuir circulation in a shallow ocean. J. Geophys Res., 116:1-15.

144

[12] Langmuir, I., 1938. Surface motion of water induced by wind. Science, 87:119-123

[13] Lee, M. J., Kim, J., 1991. The structure of turbulence in a simulated plane Couette flow. Proc. 8th Symp. Shear Flows, Munich, Germany, paper 5-3.

[14] Leighton, R.I., Smith, G.B., Handler, R.A., 2003. Direct numerical simulations of free convection beneath an air-water interface at low Rayleigh numbers. Phys. Fluids. 15(10), 3181-3193

[15] Li, M., Sanford, L., Chao, S., 2004. Effects of time dependence in unstratified tidal boundary layers: results from large eddy simulations. Est. Coast. Shelf Sci. 62, 193-204

[16] Lilly, D.K., 1992. A proposed modification of the Germano subgrid-scale closure. Phys. Fluids. 3, 2746-2757

[17] Martinat, G., Xu, Y., Grosch, C.E., Tejada-Martinez, A.E., 2011. LES of turbulent surface shear stress and pressure-gradient-driven flow on shallow continental shelves. Ocean Dynamics 61:1369-1390.

[18] McWilliams, J.C., Sullivan, P.P., Moeng, C.H., 1997. Langmuir turbulence in the ocean. J. Fluid Mech., 334:1âĂŞ30

[19] Morinishi, Y., Vasilyev, O. V., 2001. A recommended modification to the dynamic two-parameter mixed subgrid scale model for large eddy simulation of turbulent flows. Phys. Fluids 13, 3400-3410

[20] Nagaosa, R., Saito, T., 1997. Turbulence structure and scalar transfer in stably stratified free-surface flows. AIChE J. 43, 2393

[21] Papavassiliou, D.V., Hanratty, T.J., 1997. Interpretation of large-scale structures observed in a turbulent plane Couette flow. Int. J Heat Fluid Flow. 18, 55-69.

[22] Peters, F. and Marrase, C., 2000. Effects of turbulence on plankton: an overview of experimental evidence and some theoretical considerations. Marine Ecology Progress Series 205:291-306.

[23] Petrovskii, S.V. and Malchow, H., 2004. Mathematical Models: Mathematical models of marine ecosystems. Encyclopedia of Life Support Systems, EOLSS Publishers, Oxford UK.

[24] Pope, S. B., 2000. Turbulent Flows. Cambridge University Press

[25] Sanford, L.P., 1997. Turbulent mixing in experimental ecosystem studies. Marine Ecology Progress Series 161:265-293.

[26] Scully, M.E., 2014. Langmuir Circulation and Turbulence in Chesapeake Bay. Proceedings of the 17th Physics of Estuaries and Coastal Seas (PECS) conference, Porto de Galinhas, Pernambuco, Brazil, 19-24 October 2014

[27] Skyllingstad, E.D., Denbo, W., 1995. An ocean large-eddy simulation of Langmuir circulations and convection in the surface mixed layer. J. Geophys Res. 100:8501-8522.

[28] Smagorinsky, J., 1963. General circulation experiments with the primitive equations. I. The basic experiment. Mon. Weather Rev. 91, 99-164

[29] Taylor, J.R., Sarkar, S., Armenio, V., 2005. Large eddy simulation of stably stratified open channel flow. Phys. Fluids. 17(11)

[30] Tejada-Martínez, A.E., Grosch, C.E., 2007. Langmuir turbulence in shallow water. Part 2. Large-eddy simulation. J. Fluid Mech. 576, 63-108

[31] Tejada-Martínez, A.E., Grosch, C.E., Gargett, A.E., Polton, J.A., Smith, J.A., MacKinnon, J.A., 2009. A hybrid spectral/finite-difference large-eddy simulator of turbulent processes in the upper ocean. Ocean Model. 30, 115-142

[32] Tejada-Martínez, A.E., Grosch, C.E., Sinha, N., Akan, C., Martinat, G., 2012. Disruption of the bottom log layer in large-eddy simulations of full-depth Langmuir circulation. J. Fluid Mech. 699, 79- 93

[33] Thorpe, S., 2004. Langmuir Circulation. Annu. Rev. Fluid Mech. 36, 55-79

[34] Walker, R., Tejada-Martinez, A.E., Martinat, G., Grosch, C.E., 2014. Larger-eddy simulation of open channel flow with surface cooling. Int J Heat Fluid Flow. 50, 209-224

[35] Eoearth.org,. 'Encyclopedia Of Earth'. N.p., 2015. Web. 8 Apr. 2015.
http://www.eoearth.org/article/Coastalzone

[36] Chea, Terence. 'Strange Things Along Pacific Coast Waters'. msnbc.com. N.p., 2005. Web. 8 Apr. 2015.
http://www.nbcnews.com/id/8796487/.UUDTh9ZJM7k

[37] Whoi.edu,. 'CBLAST Main Page'. N.p., 2015. Web. 8 Apr. 2015.
www.whoi.edu/science/AOPE/dept/CBLASTmain.html

[38] Skio.uga.edu. 'Executive Summary'. N.p., 1998. Web. 8 Apr. 2015.
http://www.skio.uga.edu/research/coop/downloads/execsumm.pdf

[39] Physics.utoronto.ca,. N.p., 2015. Web. 8 Apr. 2015.
http://www.physics.utoronto.ca/ nonlin/thermal.html

[40] John F. Gibson, School of Physics at Georgia Tech. 'John F. Gibson: Research, In Plain Words'.
Cns.gatech.edu. N.p., 2015. Web. 8 Apr. 2015.
http://www.cns.gatech.edu/ gibson/PCF-movies/plainwords.html

[41] Commons.wikimedia.org,. 'File:Convrolls.PNG - Wikimedia Commons'. N.p., 2007. Web. 8
Apr. 2015.
http://commons.wikimedia.org/wiki/File:Convrolls.PNG

[42] Www2.ucar.edu,. N.p., 2015. Web. 8 Apr. 2015.
https://www2.ucar.edu/sites/default/files/news/2011/CESMfinal.jpg

[43] Nap.edu,. 'Oil Spill Dispersants: Efficacy And Effects'. N.p., 2015. Web. 8 Apr. 2015.
http://www.nap.edu/openbook.php?isbn=030909562X

Appendix A: Grid Stretching

In refining the grid we require less distance between grid points near the surface and near the bottom wall, where we have particularly high velocity and vertical temperature gradients. In order to resolve these gradients, we need to 'stretch' our grid in these regions. Define the regular fixed gap between mesh points as ξ. To apply a smaller mesh near the boundary, consider applying a hyperbolic mapping function $z_i = f(\xi_i)$ which maps regularly spaced points ξ_i, to new stretched points z_i on the same domain (in the vertical direction only; the horizontal directions remain evenly spaced). This can be achieved using the function

$$z_i = f(\xi_i, b, tanh^{-1}(b)) = (1/b)tanh(\xi_i tanh^{-1}(b)) \tag{A.1}$$

where z_i are the new refined grid points, ξ_i are the original evenly spaced grid points and b is a constant which can be adjusted according to the required clustering of the grid points (see Tejada-Martinez et al (2007) [30] for further detail on this mapping function).

Appendix B: Balances of Momentum and Temperature

We can assess the accuracy of our numerical solution by comparing actual (from the LES) and theoretical values of the respective terms of Reynolds-averaged balances of temperature and momentum. These balances should be satisfied when the simulations have reached a statistically steady state (such that these averages are no longer changing in time).

Any resolved variable may be decomposed as

$$\bar{\phi} = \langle\bar{\phi}\rangle + \bar{\phi}' \tag{B.1}$$

where $\langle\cdot\rangle$ denotes averaging in time and over the horizontal directions x_1 and x_2 and $\bar{\phi}'$ is the resolved fluctuation, denoted by the prime. Applying this Reynolds decomposition generates the Reynolds-averaged momentum and temperature equations, where we can include the additional terms for our body force and source term:

$$0 = -\frac{d}{dx_3}<\bar{u}_1'\bar{u}_3'> + \frac{1}{Re_\tau}\frac{d^2<\bar{u}_1>}{dx_3^2} + \frac{d<\tau_{13}^{SGS}>}{dx_3} + f \tag{B.2}$$

and

$$0 = \frac{1}{PrRe_\tau}\frac{d^2<\bar{\theta}>}{dx_3^2} - \frac{d<\bar{u}_3'\bar{\theta}'>}{dx_3} + \frac{d<q_3^{SGS}>}{dx_3} + s \tag{B.3}$$

149

These Reynolds averaged momentum and temperature equations can be integrated over the x_3 direction to give the balance equations for momentum and temperature respectively

$$x_3 - 1 = 2 < \bar{u}_1' \bar{u}_3' > - \frac{2}{Re_\tau} \frac{d < \bar{u}_1 >}{dx_3} - 2 < \tau_{13}^{SGS} > \qquad \text{(B.4)}$$

$$x_3 + 1 = 2Re_\tau Pr < \bar{\theta} \bar{u}_3' > - 2\frac{d < \theta >}{dx_3} - 2Re_\tau Pr < q_j^{SGS} > . \qquad \text{(B.5)}$$

In the momentum balance equation, the right hand side terms respectively represent the Reynolds stress, the viscous stress and the subgrid-scale stress. In the temperature balance equation, we have the resolved turbulent vertical temperature flux, the molecular vertical temperature flux, and the SGS vertical temperature flux. Note that in simplifying these equations by eliminating the constant terms, the remaining stresses and fluxes acquire constant coefficients. Following the integration, the sum of the three stresses in the momentum balance and the sum of the three fluxes in the temperature balance will be a line with a constant slope. As mentioned, the comparison of the theoretical balances given above to those found in the computational results gives an indication of the level of accuracy provided by the LES.

150

Appendix C: SGS Models

The dynamic Smagorinsky model is a model used to represent the unresolved sub-grid scale terms described in Chapter 3. This model is widely used in LES, and further details of the application of this model to a comparable LES to that in the present study can be found in [31].

A basic Smagorinsky model defines

$$\tau_{ij}^{SGS} = 2\nu_t \bar{S}_{ij} = \nu_t \left(\frac{\partial \bar{u}_i}{\partial x_j} + \frac{\partial \bar{u}_j}{\partial x_i} \right)$$
$$\nu_t = (C_s \bar{\Delta})^2 |\bar{S}|$$

(C.1)

where

$$|\bar{S}| = (2\bar{S}_{ij}\bar{S}_{ij})^{1/2}$$
$$\bar{S}_{ij} = (\bar{u}_{i,j} + \bar{u}_{j,i})/2$$

(C.2)

and $\bar{S}_{ij}$ is the filtered strain-rate tensor. Note that τ_{ij}^{SGS} as given above is the deviatoric part of the τ_{ij}^{SGS} tensor defined in Chapter 3, the isotropic element can be combined into the pressure resulting in a modified version of the pressure.

151

Similarly for the temperature equation, recall the SGS turbulent heat flux $q_j = -\overline{\theta u_j} + \bar{\theta}\bar{u}_j$. This may be modeled as

$$q_j^{SGS} = D_T \frac{\partial \bar{\theta}}{\partial x_j}$$

$$D_T = (C_t\bar{\Delta})^2|\bar{S}|$$

(C.3)

where this D_T is the turbulent eddy diffusivity and C_t is the dimensionless Smagorinsky coefficient for the temperature equation. $(C_s\bar{\Delta})^2$ and $(C_t\bar{\Delta})^2$ are calculated dynamically; details can be found in [28] and [16].

In flows with Langmuir cells and $Ra_\tau = 5000$ the full-depth cells lead to vanishing or negative vertical velocity gradients throughout a large portion of the water column. For these cases, the dynamic Smagorinsky model was augmented with a scale-similarity term as

$$\tau_{ij}^{SGS} = 2(C_s\bar{\triangle})^2|\bar{S}|\bar{S}_{ij} + C_L(\bar{u}_i\bar{u}_j - \overline{u_iu_j})$$

$$= 2\nu_t\bar{S}_{ij} + C_L(\bar{u}_i\bar{u}_j - \overline{u_iu_j})$$

(C.4)

Coefficient C_L is calculated dynamically in addition to $(C_s\bar{\Delta})^2$. This model is outlined in more detail in [19].

152

Below is permission to use Figure 1.1.

On 3/30/2015 4:40 PM, Rachel Walker wrote:

> Good afternoon,
>
> I'd like to use the figure on the left in
>
> http://www.whoi.edu/science/AOPE/dept/CBLASTmain.html
>
> in my PhD dissertation. Do you know who the copyright holder is of this image, and where I can gain permission to use it?
>
> Thank you,
>
> Rachel

Sheila Hurst

to me

Hi Rachel,

You have permission to use the attached figure. Please just add the copyright below.

Thank you,
Sheila

-------- Forwarded Message --------
Subject:Re: CBLAST figure
    Date:Thu, 02 Apr 2015 13:23:34 -0400
    From:Jayne Doucette
       To:Sheila Hurst

It's attached Sheila, and she just needs to credit it somewhere like this:
©Woods Hole Oceanographic Institution

153
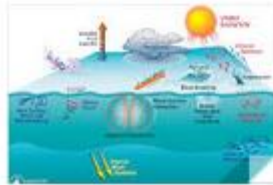
Below is permission to use Figure 1.2.

Rachel Walker ‹   ›   6:16 pm (2 days ago)

to

Good evening Dr Cvitanovic,

I'd like to include the figure located at

http://chaosbook.org/tutorials/color2.html

in my PhD thesis for the Department of Civil and Environmental Engineering at the University of South Florida. Are you the current copyright holder of the images on this site?

Thank you,

Rachel

Predrag Cvitanović   6:28 pm (2 days ago)

to John, me

almost all figures were generated by John F Gibson - contact him. You have my permission to use any material on ChaosBook.org, as long as you cite the source

best of luck with your thesis!

Predrag

home, work, road & voicemail:
check here for schedule and travel dates

John F. Gibson   6:36 pm (2 days ago)

to Predrag, me

Dear Ms. Walker:

You're welcome to use that figure and any other figure of mine in the chaosbook fluids tutorial. I would appreciate an attribution. Best regards, and best of luck with you thesis!

John Gibson

154

www.manaraa.com

Below is permission to use Figure 1.3.

Copyright Clearance Center

Confirmation Number: 11329008
Order Date: 03/30/2015

Customer Information

Customer: Rachel Walker
Account Number: 3000904059
Organization: Rachel Walker
Email: rachelwalker@mail.usf.edu
Phone: +1 (813)6441603
Payment Method: Invoice

This is not an invoice

Order Details

The International journal of heat and fluid flow

Billing Status:	N/A

Order detail ID:	66599894
ISSN:	0142-727X
Publication Type:	Journal
Volume:	
Issue:	
Start page:	
Publisher:	ELSEVIER INC.
Author/Editor:	INSTITUTION OF MECHANICAL ENGINEERS (GREAT BRITAIN

Permission Status: ✅ Granted

Permission type: Republish or display content
Type of use: Thesis/Dissertation
Order License Id: 3599030251335

Requestor type	Academic institution
Format	Electronic
Portion	image/photo
Number of images/photos requested	1
Title or numeric reference of the portion(s)	Approximation of large structures by a secondary flow, Figure 8
Title of the article or chapter the portion is from	Interpretation of large-scale structures observed in a turbulent plane Couette flow
Editor of portion(s)	N/A
Author of portion(s)	Dimitrios V. Papavassiliou and Thomas J. Hanratty
Volume of serial or monograph	18
Issue, if republishing an article from a serial	No. 1
Page range of portion	60
Publication date of portion	February 1997
Rights for	Main product
Duration of use	Life of current edition
Creation of copies for the disabled	no
With minor editing privileges	no
For distribution to	Worldwide
In the following language(s)	Original language of publication
With incidental promotional use	no
Lifetime unit quantity of new product	Up to 499
Made available in the following markets	academic
The requesting	

person/organization	Rachel Walker
Order reference number	
Author/Editor	Rachel Walker
The standard identifier	LESthesis
Title	Large-eddy Simulation of the Inner Continental Shelf Under the Combined Effects of Surface Temperature Fluxes, Tidal Currents and Langmuir Circulation
Publisher	University of South Florida
Expected publication date	May 2015
Estimated size (pages)	200

Note: This item was invoiced separately through our **RightsLink** service. More info $ 0.00

Total order items: 1   **Order Total: $0.00**

About Us | Privacy Policy | Terms & Conditions | Pay an Invoice

Below is permission to use Figure 1.4.

1. Are UCAR/NCAR images in the public domain?

No. All University Corporation for Atmospheric Research and National Center for Atmospheric Research images remain the property of UCAR. Access to the images included in the UCAR Digital Image Library is restricted and protected by U.S. copyright laws.

2. How can I get permission to use photos for non-commercial purpose?
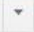
You have permission to use all images for non-commercial use. These are available at no cost for all non-commercial users. However, they may not be used to infer or imply UCAR/NCAR endorsement of any product or position or be used for religious or political purposes. Neither should they be used to distort the reality of the image they portray. If you have questions regarding use of any UCAR material please e-mail us.

3. Is there a cost for non-commercial use of the images?

No. Non-commercial research, educational, and private use of materials on this website is permitted at no cost. For these purposes, you may reproduce (print, photocopy, or download) materials from this website without prior permission, on the condition that you provide proper attribution of the source in all copies (see Copyright) and comply with the Terms of Use. Although we don't require you to contact us in advance for these purposes, we do appreciate hearing from teachers, students, and researchers who are using our resources in interesting ways. Please e-mail us

Below is permission to use Figure 1.5.

Rachel Walker   2:54 PM (4 minutes ago)
to smorris

Good afternoon Dr Morris,

I'm interested in using the first figure at the following location:

http://www.physics.utoronto.ca/~nonlin/thermal.html

in the introduction to my PhD thesis (for the department of Civil & Environmental Engineering at the University of South Florida).
Are you the copyright holder for these images? If so, is there an official way for me to gain permission to use this figure?

Kind regards,

Rachel Walker

Stephen Morris   2:56 PM (2 minutes ago)
to me

Hello

Yes, I own them.

Just go ahead and use them with a tiny credit back to me, thanks.

Below is permission to use Figure 1.6.
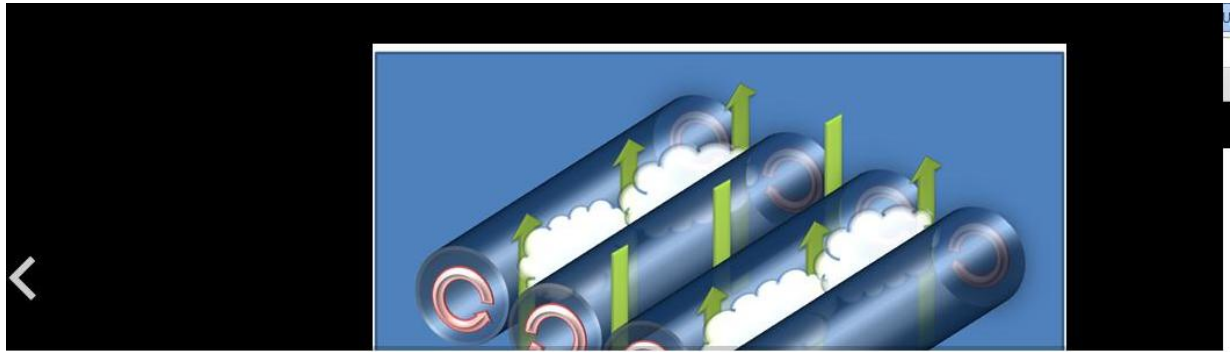
Simple schematic of the production of cloud streets by horizontal convective rolls.

Daniel Tyndall, Departmant of Meteorology, University of Utah. Original uploader was Dtyndall at en.wikipedia - Transferred from en.wikipedia (Original text : *User created schematic.*)

Schematic of horizontal convective rolls in the atmosphere in the production of cloud streets.

Public Domain [view terms]
File: Convrolls.PNG
Uploaded by Pierre cb
Created: April 6, 2007

Permission details

Released into the public domain (by the author). (Original text : public domain)

159

Below is permission to use Figure 1.7.

www.manaraa.com

Below is permission to use Figure 1.8.

161

Number of figures/tables/illustrations	1
Format	electronic
Are you the author of this Elsevier article?	No
Will you be translating?	No
Original figure numbers	Figure 1
Title of your thesis/dissertation	Large-eddy Simulation of the Inner Continental Shelf Under the Combined Effects of Surface Temperature Fluxes, Tidal Currents and Langmuir Circulation
Expected completion date	May 2015
Estimated size (number of pages)	200
Elsevier VAT number	GB 494 6272 12
Permissions price	0.00 USD
VAT/Local Sales Tax	0.00 USD / 0.00 GBP
Total	0.00 USD
Terms and Conditions	

INTRODUCTION

162

Below is permission to use Figure 3.1.

Rachel Walker <[   ]>   Apr 3 (1 day ago)
to Andres

Dr Tejada,

As the copyright holder of the figures contained within your PhD thesis "Dynamic Subgrid-scale Modeling for Large-Eddy Simulation of Turbulent Flows with a Stabilized Finite Element Method", please may I request your permission to use Figure 1.2 on page 11 in my dissertation titled "Large-eddy Simulation of the Inner Continental Shelf Under the Combined Effects of Surface Temperature Fluxes, Tidal Currents and Langmuir Circulation" to be published via the University of South Florida.

Thank you,

Rachel

Tejada-Martinez, Andres   Apr 3 (1 day ago)
to me

Rachel,

Yes, please use this figure.

Andres

163

Below is permission to include content from [34].

pages)

Elsevier VAT number	GB 494 6272 12
Permissions price	0.00 USD
VAT/Local Sales Tax	0.00 USD / 0.00 GBP
Total	0.00 USD

Terms and Conditions

INTRODUCTION

1. The publisher for this copyrighted material is Elsevier. By clicking "accept" in connection with completing this licensing transaction, you agree that the following terms and conditions apply to this transaction (along with the Billing and Payment terms and conditions established by Copyright Clearance Center, Inc. ("CCC"), at the time that you opened your Rightslink account and that are available at any time at http://myaccount.copyright.com).

GENERAL TERMS

2. Elsevier hereby grants you permission to reproduce the aforementioned material subject to the terms and conditions indicated.

3. Acknowledgement: If any part of the material to be used (for example, figures) has appeared in our publication with credit or acknowledgement to another source, permission must also be sought from that source. If such permission is not obtained then that material may not be included in your publication/copies. Suitable acknowledgement to the source must be made, either as a footnote or in a reference list at the end of your publication, as follows:

"Reprinted from Publication title, Vol /edition number, Author(s), Title of article / title of chapter, Pages No., Copyright (Year), with permission from Elsevier [OR APPLICABLE SOCIETY COPYRIGHT OWNER]." Also Lancet special credit - "Reprinted from The Lancet, Vol. number, Author(s), Title of article, Pages No., Copyright (Year), with permission from Elsevier."

4. Reproduction of this material is confined to the purpose and/or media for which permission is hereby given.

5. Altering/Modifying Material: Not Permitted. However figures and illustrations may be altered/adapted minimally to serve your work. Any other abbreviations, additions, deletions and/or any other alterations shall be made only with prior written authorization of Elsevier Ltd. (Please contact Elsevier at permissions@elsevier.com)

6. If the permission fee for the requested use of our material is waived in this instance, please be advised that your future requests for Elsevier materials may attract a fee.

7. Reservation of Rights: Publisher reserves all rights not specifically granted in the combination of (i) the license details provided by you and accepted in the course of this licensing transaction, (ii) these terms and conditions and (iii) CCC's Billing and Payment terms and conditions.

165